DISSERTATION

MODELING AND CONTROLLING NANOSCALE PATTERNS FORMED BY BOMBARDMENT WITH A BROAD ION BEAM

Submitted by

Matthew Paul Harrison

Department of Physics

In partial fulfillment of the requirements

For the Degree of Doctor of Philosophy

Colorado State University

Fort Collins, Colorado

Summer 2017

Doctoral Committee:

Advisor: R. Mark Bradley

Martin Gelfand
Patrick Shipman
Stuart Field

ABSTRACT

MODELING AND CONTROLLING NANOSCALE PATTERNS FORMED BY BOMBARDMENT WITH A BROAD ION BEAM

For over half a century it has been known that bombarding a solid surface with a broad ion beam can produce periodic nanoscale structures. Given the virtually limitless promise of nanotechnology, the potential of ion bombardment to produce nanopatterned surfaces over large areas in a simple and economical way has attracted substantial interest. In the decades since its discovery, there has been a wealth of experimental and theoretical work examining the phenomenon in detail, with the eventual goal of using ion beam sputtering (IBS) to produce useful nanostructures.

Despite the body of work, there are many open questions and unsurmounted challenges remaining. In this thesis, I present work that I have conducted in collaboration with my advisor, Mark Bradley, with whom I addressed some of these challenges. I show how we developed a formalism which connects information about single ion impacts to the evolution of a surface which sustains $> 10^{16}$ such impacts per square centimeter. We have also produced theoretical results for the case of a binary material being bombarded while rotated azimuthally, with some unexpected findings. I also discuss some very exciting theoretical predictions for the case in which an elemental target is bombarded while the polar angle of ion incidence periodically changes. In this case we find the temporal driving can induce a surface pattern which is nearly perfectly periodic in the long time limit. I also discuss our work on using templated surfaces in conjunction with IBS to produce high quality blazed gratings and multilayer blazed gratings. This work is the subject of a current collaboration with Carmen Menoni and her students.

ACKNOWLEDGEMENTS

It is impossible to accurately account for all of the people that have contributed to this thesis, to my career, and to my life (despite the equivalence of these three things for a graduate student), so I will err on the side of brevity. I would like to thank my parents firstly, for without their love and unconditional support this might never have been possible. I would like to thank my advisor, Mark Bradley, for making me a better scientist, and for instilling in my bones the need to label axes, minimize handwaving, define terms, and the idea that you have not really discovered something unless you can rigorously defend it. Lastly, I would like to thank the innumerable friends and colleagues that have helped me along my journey.

DEDICATION

I would like to dedicate this thesis to my loving parents

TABLE OF CONTENTS

LIST OF FIGURES

CHAPTER 1

OVERVIEW OF MATERIAL PRESENTED

Generating and controlling nanoscale patterns has been the subject of decades of work among countless researchers and across many disciplines. Applications as broad ranging as magnetic thin films,[1] linear and nonlinear optical components,[2,3,4,5,6,7,8] nanowire fabrication,[9] bioimaging devices,[10] and templates for growing carbon nanotubes[11] are evidence that this subject is anything but esoteric. One promising technique for developing such patterns is bombardment of a solid surface with a broad ion beam. It has long been known that under certain conditions such bombardment may spontaneously produce nanoscale patterns in the surface height. While the length scales of these patterns, which are typically on the order of tens to hundreds of nanometers, are accessible by direct lithographic methods such as electron beam lithography, ion bombardment has the tremendous advantage that it is a "bottom up" fabrication technique. If the experimental conditions can be arranged such that a desirable pattern forms on the surface, such a pattern may be easily formed on a surface whose area is enormous compared to the characteristic length scale of the pattern. This is in contrast to "top down" fabrication techniques, in which every surface feature must be individually etched. For a summary of the history of this field and its applications, see Chapter 2. While the potential upside of this method is significant, there has been substantial difficulty in precisely controlling the patterns are formed by ion bombardment. In this thesis I describe the research I have done with the goal of understanding and controlling these patterns.

In Chapter 3, we develop an improvement on an extant theoretical proposal. The aim of this work was to use atomistic simulations to produce a model of a macroscopic ion bombarded surface. Heuristically, if one had sufficient information about the average crater left by a single ion impact, one could extract from this a prediction for the overall surface evolution. The work done previously on this problem was the development of a mathematical formalism that takes the average crater resulting from a single ion impact and produces a continuum equation of motion for the entire surface.[12] This average crater may come either from atomistic simulations or from a microscopic theory. The latter case represents a means to test the formalism itself, as it should reproduce other theories based on the same assumptions. Despite the explicit claims of the authors in Ref. [12], their formalism did not reproduce the results of the Bradley-Harper (BH) theory. The BH theory is in turn based on the Sigmund model of ion sputtering.[13,14] Crucially, the analysis in Ref. [12] neglected the dependence of the average crater on the curvature of the surface. This neglect stems from an inconsistency of assumptions in their approximation of the average crater. To correct this, we developed our own formalism which accounts for the dependence of the crater on local surface curvature. Our formalism does reproduce the results of the BH theory.

In Chapter 4 we generate predictions for the evolution of a binary surface which is undergoing discrete, regular, azimuthal rotations. These results are surprising and unforeseen. Azimuthal rotation has been considered before, primarily in the context of suppressing the formation of surface patterns.[15,16,17,18,19] For applications such as secondary ion mass spectroscopy, it is desirable that the surface remain as flat as possible to optimize the depth resolution. However, for the case of a binary material or bombardment with concurrent deposition of a second atomic species, we show that unexpected and novel effects may occur as a result of azimuthal rotation. In Chapter 4, we develop a general formalism which takes an equation of motion valid for a single angle of

incidence and develops predictions for how the surface will evolve if it is discretely rotated by 180° azimuthally at a frequency ω. We apply this general result to a particular equation of motion which is relevant for ion bombardment with co-deposition of impurities. Among the surprising results is that the wavelength of the resulting pattern may be tuned by adjustment of the rotation frequency. Furthermore, the wavelength of the pattern may even jump discontinuously as a result of a continuous variation in rotation frequency.

In Chapter 5 we show numerical evidence that periodic variation of the polar angle of incidence can produce nanoscale patterns which are virtually free of defects. If confirmed experimentally, this would constitute a major breakthrough in the field, as the primary obstacle to the widespread use of ion bombardment as a nanofabrication tool is the high density of defects in the patterns that typically form. This discovery is also of interest to mathematicians, as the equation used to model the ion bombarded surface is widely studied because it exhibits spatiotemporal chaos. The fact that temporal driving can induce nearly perfect spatial periodicity is both exciting and invites further study. In this work we investigate the necessary and sufficient conditions for the formation of nearly perfect ripple structures. In particular, we examine influence of the rocking frequency and amplitude on the resulting morphology, and verify that undesirable additional terms likely to occur due to physical considerations do not constitute a substantial impediment to the suppression of chaos.

In Chapter 6 we study the time evolution of surfaces which have been pre-patterned, and are subjected bombardment with an obliquely incident ion beam. This goal of this work is to guide experimentalists working to produce blazed gratings (BGs). Such gratings are extremely valuable in the field of spectroscopy,[20] and there has been much work on developing new methods for improving the efficiency of their operation and production.[3,4,5,6,7,8] We propose a new method of fabrication in which a periodic surface modulation is first induced by more conventional means

such as optical lithography or electron beam lithography. This prepatterned, or "templated", surface is then bombarded by a broad ion beam with precisely selected characteristics to change the shape of the periodic modulation into a diffraction grating with well defined faces (i.e. a blazed grating).

The idea of using ion bombardment on templated surfaces with the aim of producing blazed gratings has been around for decades, but all previously proposed methods rely on a very specific initial pattern shape and primarily make use of shadowing effects.[3,4,5,6,7,8] The theoretical analysis of Refs. [7] and [8] is also extremely simplistic, neglecting a wide array of physical effects that are likely to be relevant. We seek to improve on their theoretical analysis to develop a new approach to blazed grating fabrication as well as an approach which may be useful in developing multilayer blazed gratings. This work is described in detail in Chapter 6.

In Chapter 7 we consider an extension of the method proposed in Chapter 6 to the case of multilayer blazed gratings (MBGs). For light in the soft X-ray regime, most materials lack sufficient reflectivity to function effectively. One way to partially circumvent this limitation is to deposit many layers of material, the composition of which alternates between two species, D and B. Constructive interference from reflections from the surface and subsurface interfaces allows an MBG to operate with efficiencies far in excess of what a BG could produce.

The BG profile of the surface of a MBG has been seen to degrade during the deposition of the multilayers without an ion assist.[21,22,23,24] Given that the method proposed in Chapter 6 spontaneously produces a good BG profile given a sinusoidal initial condition, it is natural to think that bombarding a MBG surface which has been smoothed by deposition with an ion beam might result in it returning to a good BG profile. In Chapter 7 we present numerical evidence that this is indeed the case, and show that for appropriately chosen conditions, an arbitrary number of layers may be deposited without significant degradation of the surface profile.

CHAPTER 2

BACKGROUND

2.1 Experimental History of Ion Beam Sputtering

The experimental record of nanoscale patterns produced by ion beam sputtering (IBS) is long, rich and, at times, confusing. In this section I provide an overview of some of the major experimental developments in this area.

The fact that bombardment of a solid surface with a broad beam of inert ions can spontaneously produce nanoscale patterns in the surface topography has now been known for over half a century. Early work by Cunningham et al.[25] showed in 1960 that Ar^+ ion bombardment of metals could produce disordered rough surfaces or ripple patterns. Two years later, some of the most important elements of this phenomenon were identified by Navez et al.[26] by studying ion bombardment of glass with a beam of ionized air. In particular, for intermediate angles of ion beam incidence, they observed ripple patterns, the wavevector of which was parallel to the projection of the incident ion beam onto the surface. In what follows I will call these patterns "parallel mode ripples", and refer to ripple patterns whose wavevector is perpendicular to the wavevector of parallel mode ripples as "perpendicular mode ripples". Figure 2.1 shows a simulation in which the surface develops parallel mode ripples, while Fig. 2.2 shows an experimental example. Figure 2.3 shows a simulation in which the surface develops perpendicular mode ripples.

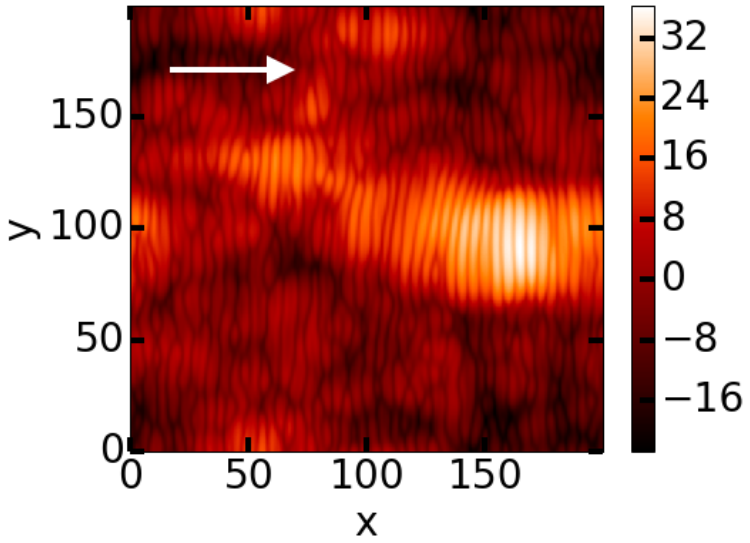

Fig. 2.1 An example of a simulation displaying parallel mode ripples. The arrow indicates the direction of the projected ion beam.

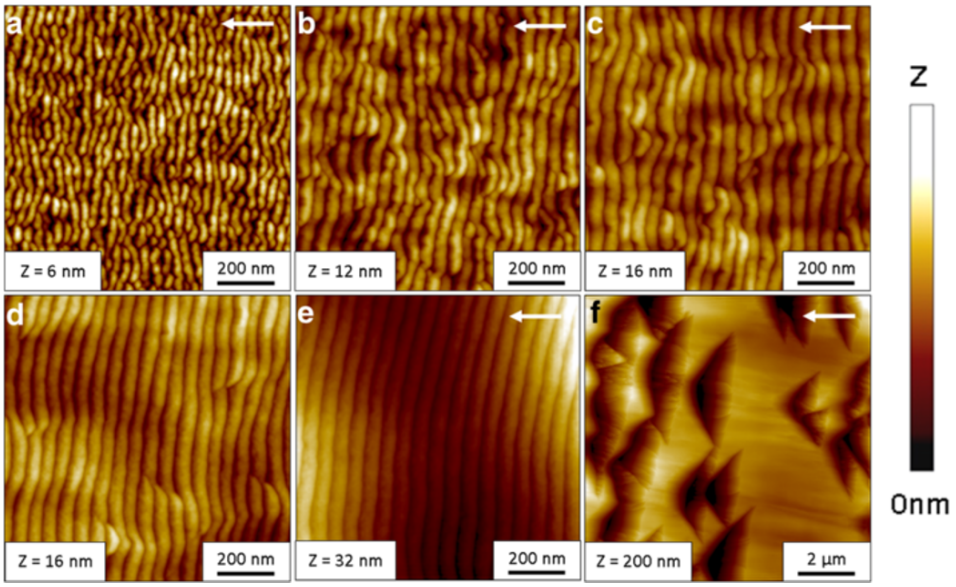

Fig. 2.2 Experimental results reported in Ref. [27]. Panels (a) - (e) display parallel mode ripples, while panel (f) shows a topography which cannot be classified as a kind of ripple pattern. These images represent AFM scans of Si surfaces subjected to 1.2 KeV Xe^{+} ion bombardment with an incidence angle of 75°. The fluence steadily increases from 1.12×10^{17} ions/cm^2 in (a) to 1.35×10^{19} ions/cm^2 in (f).

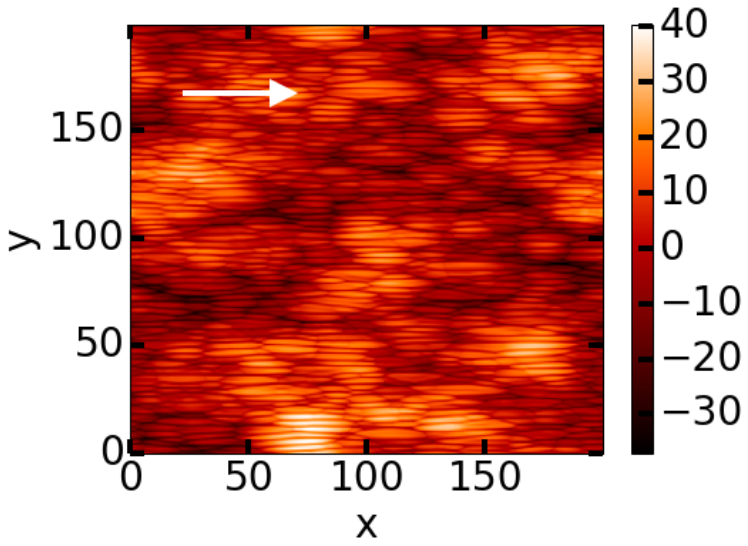

Fig. 2.3 An example of a simulation displaying perpendicular mode ripples. The arrow indicates the direction of the projected ion beam.

In order to clearly explain the plethora of experimental results on patterns formed by IBS, it is necessary to start with some of the most recent results and work backwards. This is because virtually all early IBS pattern formation experiments suffered from an uncontrolled factor: The unintentional deposition of impurities onto the sample. The critical influence of these impurities was first identified by Ozaydin et al.,[28] who performed *in situ* analysis of Mo islands grown on a Si substrate during 1 keV Ar^+ bombardment at normal incidence. When there was a large atomic flux of Mo incident on the surface, the experimenters observed disordered Mo dots spontaneously forming on the surface. When the atomic flux was set to zero, however, no patterns were formed. This strongly implied that the presence of Mo at the surface was a necessary condition for nanodot patterns to form.

There are many possible origins for inadvertent contamination fluxes. One common culprit is a highly divergent ion beam. If the ion beam spreads enough en route to the sample, stray ions strike the walls of the chamber, sputtering material from them. Typically the chambers are made from stainless steel, in which case a divergent beam would produce a deposition current of Fe atoms onto the surface. In Subsection 2.1.2 we will show experimental evidence that Fe deposition has a very strong effect on pattern formation. Due to this effect, it was once thought that the divergence of the ion beam had a strong influence on the surface morphology.[29] The device used to hold the sample can also introduce problems. Just as for the chamber walls, sputtering of the sample holder can produce a significant deposition flux, even if it is made of the same material as the sample.[30] Finally, even the grids used to accelerate the ions themselves can be struck by ions, and consequently sputter material onto the surface. However, experiments with controlled Fe deposition suggest that the atomic flux expected from this mechanism is below the threshold needed to influence the surface

topography in many cases.[31,32] The influence of impurities has been explored extensively since the breakthrough work of Ozaydin et al.[31,33,34,35]

2.1.1 Experiments on Elemental Targets

Given the influence of impurity deposition on the dynamics of ion induced pattern formation, it is difficult to draw rigorous conclusions from experiments which did not take careful precautions to avoid impurities. I will first focus on experiments in which care was taken to avoid impurity deposition, and discuss experiments in which impurities were intentionally incorporated in Subsection 2.1.2. Additionally, I will initially focus primarily on noble gas ion bombardment of Si targets for simplicity.

Careful experiments on noble gas IBS on Si have revealed the existence of a critical angle of incidence, θ_c. For incidence angles below θ_c, no significant patterns are observed. Experiments performed by Madi et al.[36,37] suggest that for 250 eV Ar^+ bombardment of Si $\theta_c \simeq 48^\circ$, and other experiments suggest similar values for θ_c.[38,39,40] The existence of a significant critical angle is at odds not just with previous experiments (in which impurites played a strong role) but also BH theory.[13] As explored later in this chapter, the BH theory predicts that ripple patterns should form spontaneously for all nonzero angles of incidence. The mass redistribution theory proposed by Carter and Vishnyakov[41] predicts a critical angle of $\theta_c = 45^\circ$.

Another phenomenon observed in low energy (<20 KeV) IBS of Si substrates is the transition from parallel mode ripples to perpendicular mode ripples as the angle of incidence is increased. Experiments by Madi et al.[36,37,42] suggest that the critical angle for this transition is approximately $\theta = 80^\circ$. However, in those works, experiments were performed for incidence angles below 75° and at 85°, but not angles in between, so this value is not terribly precise. The transition between the

two ripple modes at higher incidence angles is predicted by BH theory[13] and cannot be accounted for by the Carter-Vishnyakov (CV) effect.[41]

Broadly speaking, a typical ion bombardment experiment progresses through three distinct regimes.[43] We shall refer to these regimes as the linear, coarsening, and saturation regimes. The duration of each regime in real time is inversely proportional to the ion flux, but depends upon the incidence angle, ion energy, temperature, and other parameters in a less straightforward way. The points of transition between these regimes are not precise, but these three regimes form a useful framework for discussing IBS experiments.

During the linear regime, the surface roughness grows exponentially in time. The rate of growth of structures on the surface depends strongly on their periodicity. This is in very good agreement with the predictions of linear theories discussed later in this work, and has been investigated in detail by *in situ* grazing incidence small angle X-ray scattering (GISAXS).[44,45,46,47] In the linear regime, patterns typically have relatively simple sinusoidal profiles and tend to exhibit up-down symmetry. Futhermore, the characteristic length scale does not change appreciably in this regime. The duration of the linear regime is expected to depend on the ion flux, the strength of the nonlinearities present, and the linear growth rate. Experiments have shown that for IBS on Si just above the critical angle θ_c, the linear regime is longer than for experiments with an incidence angle well above θ_c.[36,48] Since the linear growth rate is expected to pass through zero at θ_c, it is reasonable to conclude that the increased linear regime duration near θ_c is due to a decreased linear growth rate. While there is substantial variation, a reasonable fluence below which one might expect to still be in the linear regime for 1 keV Ar^+ bombardment of Si would be on the order of 10^{16} ions/cm^2. Semiconductor surfaces at room temperature are typically amorphized during the linear regime as well.

As the surface width continues to grow, the sample eventually enters the coarsening regime. In this regime, nonlinearities start to have a large influence on the surface topography. The exponential amplitude growth observed in the linear regime slows, and the amplitude growth is seen to follow a power law scaling.[36,37,49,50] Additionally, the lateral length scale is seen to increase over time during the coarsening regime. Like the amplitude, the characteristic lateral length scale also typically grows in a power law fashion during this regime.[36,37,49,50] Figure 2.4 shows the results of a simulation in which coarsening was observed. Figure 2.5 shows a subset of the Fourier transform of the surface shown in Fig. 2.4.

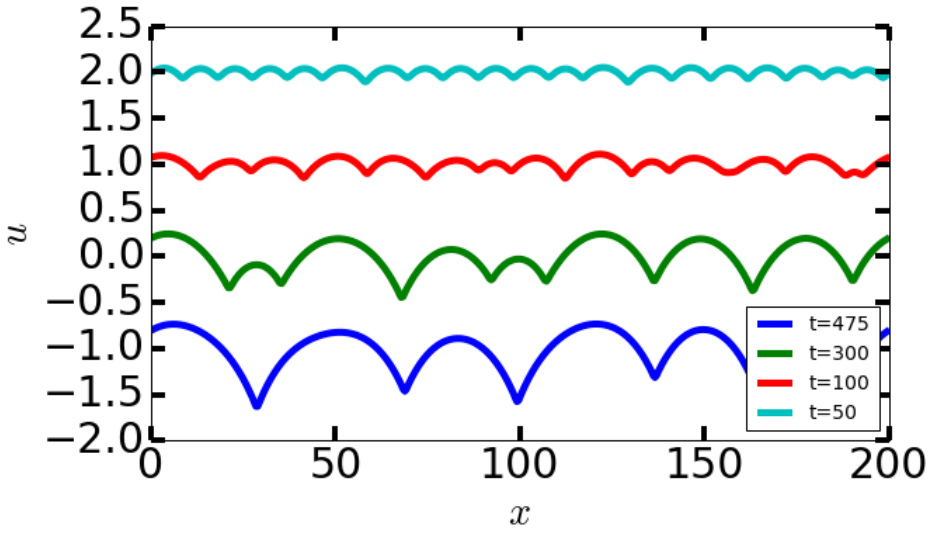

Fig. 2.4 A typical simulation in which coarsening is observed. Note that the characteristic horizontal and vertical length scales grow as the simulation proceeds. The horizontal and vertical scales are dimensionless.

The evolution of the shape of the patterns formed by IBS during the coarsening regime depends strongly on the angle of incidence. For angles less than approximately 75°, the nearly sinusoidal ripples grown during the linear regime typically coarsen into humps.[49,50,51,52] These humps resemble parabolic arcs connected by small regions of large positive curvature. In addition to the

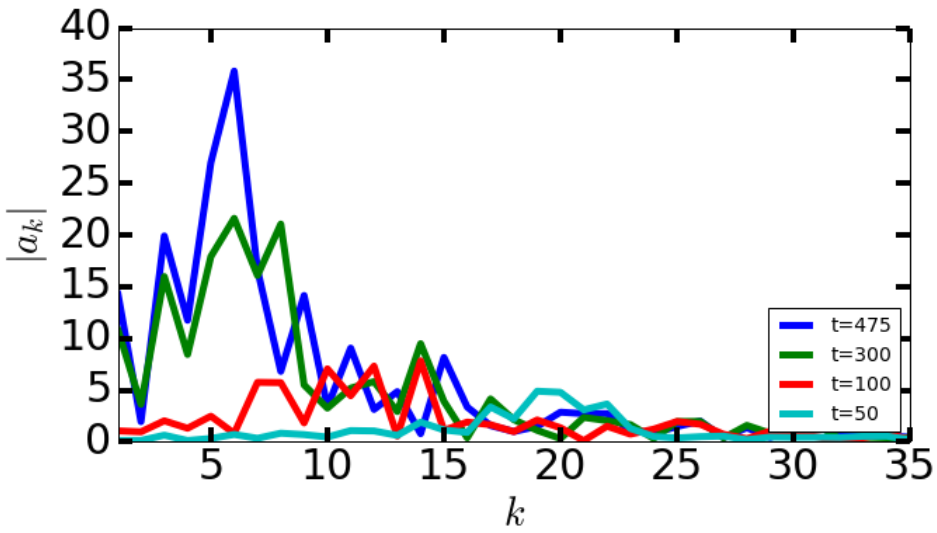

Fig. 2.5 A plot of the Fourier amplitudes of the surfaces shown in Fig. 2.4. As the simulation proceeds, the maximum in the Fourier spectrum grows and moves towards the origin.

power law scaling, the influence of nonlinearities is evident from the lack of up-down symmetry in the patterns that develop in this regime.

For higher angles of incidence, an ion bombarded surface has been observed to coarsen into terraced structures.[53,54,55,56,57,58,59,60,61,62,63,51,52,27,64] These surfaces typically have two selected slopes. A variety of explanations have been proposed for the existence of terraced topographies, including ion reflection and redeposition,[53] shadowing,[51,52] or the formation of undercompressive shocks.[65,66] Examples of simulated surfaces exhibiting terrace formation are shown in Figs. 2.6 and 2.7, and experimental examples are shown in Figs. 2.8 and 2.9.

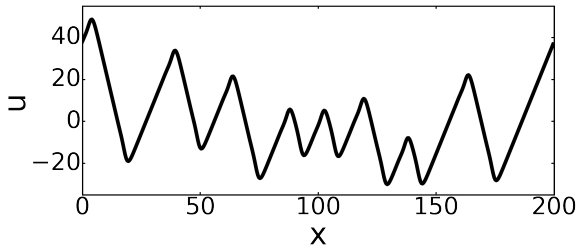

Fig. 2.6 A typical 1D terraced surface cross section in the saturation regime.

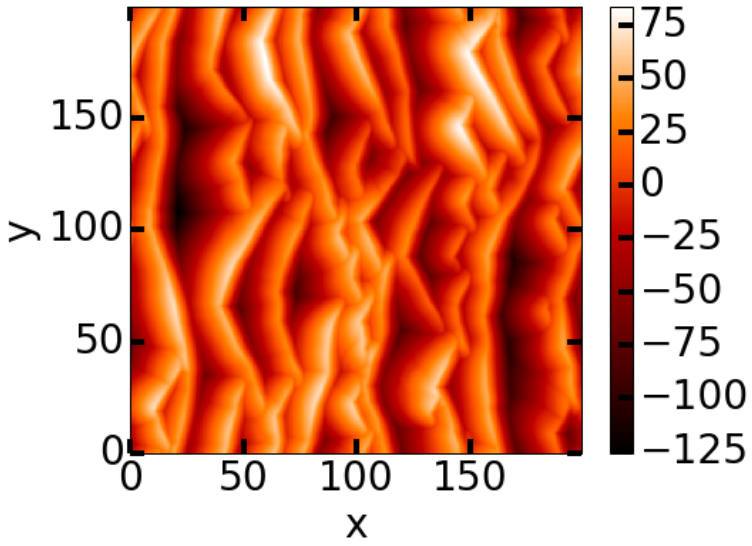

Fig. 2.7 A typical 2D terraced surface in the saturation regime.

Eventually the surface amplitude and characteristic length scale saturate and do not grow any further. The saturation regime is by far the least explored of the three regimes discussed here because it can take a very long time for an experiment to exit the coarsening regime and the dynamics during ripple growth are generally considered to be more interesting. Nevertheless, it is important to note that the vertical and horizontal length scales do not grow without limit. The existence of a saturation regime following a coarsening regime is referred to as the phenomenon of "interrupted coarsening".[67,43,68,69]

2.1.2 IBS with Multiple Atomic Species

In this section we expand the discussion of patterns formed by IBS to the case in which there is more than one non-noble-gas atomic species present at the surface. Such a situation can result from deposition of a second atomic species onto an elemental sample during ion bombardment or ion bombardment of a binary material with a noble gas ion beam. While the effects of noble gas ion implantation can affect the morphology of the bombarded surface, the influence of ion implantation

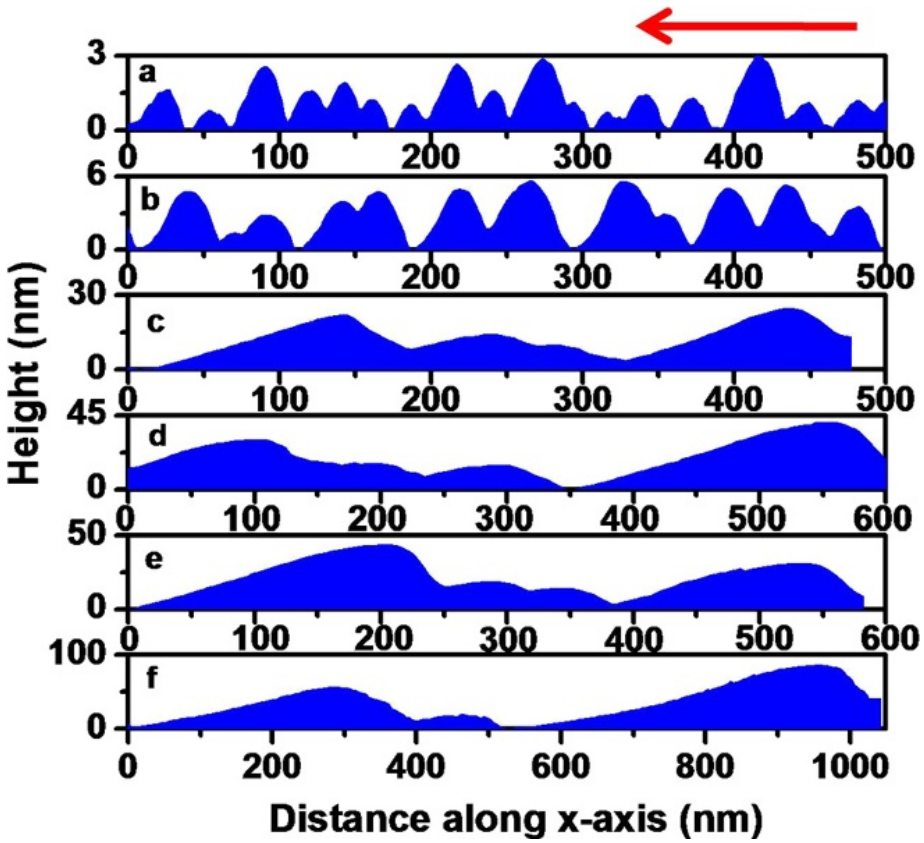

Fig. 2.8 Experimental cross sections demonstrating coarsening and terrace formation. These results were taken from Ref. [52]. The height profiles were extracted from AFM scans of a Si surface subjected to 500 eV Ar^+ ion bombardment with an incidence angle of 72.5°. The fluence increases from top to bottom, ranging from 1×10^{17} to 20×10^{17} ions/cm^2.

is expected to be much weaker than the influence of the presence of multiple chemically reactive elements at the surface layer.[70] The presence of multiple atomic species at the surface simultaneously increases the difficulty of accurately modeling the surface morphology and greatly expands the range of patterns which emerge from IBS. In Section 2.7 I will discuss various theoretical models which have been proposed to deal with this complicated situation. In this section I will provide an overview of some of the experimentally observed patterns which may form for the case in which there are multiple non-volatile atomic species present on an ion bombarded surface.

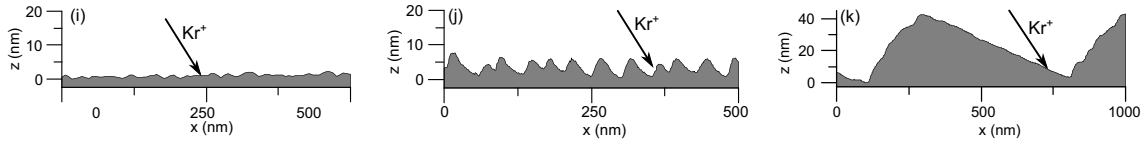

Fig. 2.9 Experimental cross sections demonstrating coarsening and terrace formation. These results were taken from Ref. [64]. The height profiles were extracted from AFM scans of a Si surface subjected to 2 KeV Kr^+ ion bombardment with an incidence angle of 75°. The fluence increases from left to right, ranging from 1×10^{16} to 3×10^{18} ions/cm^2.

One of the most striking results from some such experiments is the formation of somewhat regular arrays of nanodots.[71,72] The first experimental evidence for arrays of nanodots resulting from IBS on a binary material was provided by Facsko *et al.*[73] in 1999. In that work, a normally incident beam of 420 eV Ar^+ ions bombarded a GaSb surface. The surface was observed to develop a disordered hexagonal array of nanodots whose diameter was approximately 30 nm. An SEM image of these dots and their autocorrelation function is shown in Fig. 2.10. A short time after this, Frost *et al.*[74] obtained similar results for 500 eV Ar^+ bombardment of InP. Rather than using a normally incident ion beam, Frost *et al.* employed an obliquely incident beam at 40° off normal, and concurrently rotated the sample azimuthally. These experiments demonstrated that IBS could be a useful and economical way to produce ordered arrays of nanodots on semiconductor surfaces. In Chapter 4 we investigate the effects of azimuthal rotation during IBS of a binary target in the linear regime.

Other experiments ostensibly demonstrated the formation of arrays of nanodots on pure Si surfaces with 1.2 keV normal incidence Ar^+ sputtering.[75] However, this work proved difficult to reproduce, with some researchers finding arrays of dots under similar conditions,[76,77] and others finding only flat surfaces.[44,78] As discussed previously, the inconsistencies in experimental results are almost certainly due to the inadvertent deposition of a second atomic species. There is no

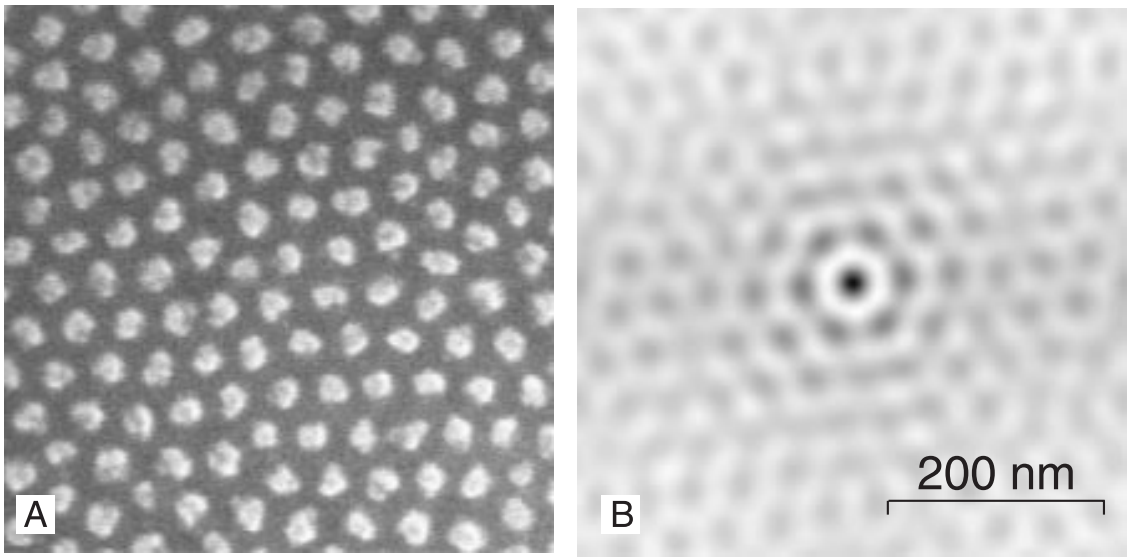

Fig. 2.10 An SEM image of the disordered hexagonal dot pattern produced in Ref. [73]. The left panel shows the real space image, while the right panel shows the autocorrelation function of the surface. These experiments were performed with 420 eV Ar^+ ion bombardment of a GaSb surface at normal incidence.

concrete experimental evidence that Si surfaces form nanodot arrays when only one non-noble-gas species is present at the surface.

One of the best demonstrations of the variety of morphologies possible with multiple atomic species present on the surface, as well as the sensitivity of those morphologies to experimental conditions, is the review published by Ziberi *et al.* in 2009.[79] Although the authors of that work believed they were studying noble gas ion bombardment of Si and Ge targets, their results suggest that unintentional impurity deposition was an extremely important factor. In Ref. [79], the authors observe parallel and perpendicular mode ripples with a high degree of order, as well as nanodots that form into hexagonal and square arrays. As we will see below, these results can likely be explained by the formation of iron silicides or similar compounds due to unintentional Fe deposition from sputtering the chamber walls and/or sample holder.

More recently, as the importance of impurity deposition during IBS has become clearer, there have emerged several papers which systematically investigate the effect of such deposition. In the case of inadvertent deposition, it is believed that the impurity flux originates from ions sputtering Fe atoms off of the chamber walls or sample holder. Because of this, many of the systematic studies in the literature have focused on the deposition of Fe and similar metals during IBS.

Macko *et al.*[80] chose to investigate the effects of deposition in a clever fashion that was first introduced by Hofsass and Zhang.[81] They began by verifying that for angles of incidence less than approximately 45°, 2 keV Kr^+ bombardment of Si does not produce any patterns, provided that the vacuum of the chamber is high and the ion beam only strikes the sample. The experimenters subsequently introduced a known source of impurities, namely a stainless steel plate mounted at one end of the sample. Ions striking this plate will sputter Fe atoms onto the surface. In a single run, the experimenters could investigate a range of deposition fluxes and angles, since points on the surface close to the plate would receive a much greater deposition flux than would points far from the plate. See Fig. 2.11 for an illustration of their experimental setup.

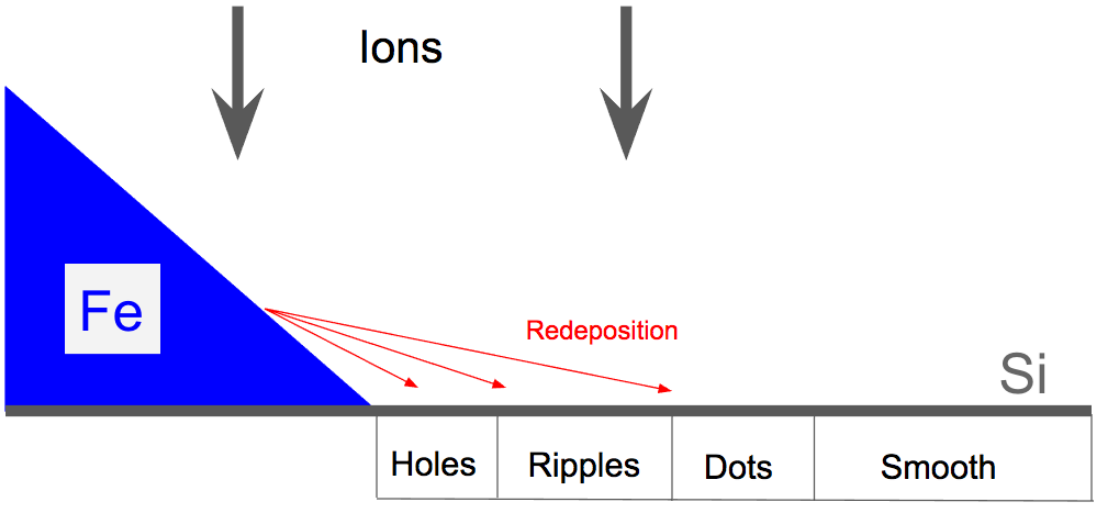

Fig. 2.11 An illustration of the experimental setup used in Refs. [31], [80], and [81] . The relative distances to the various topographies are not to scale.

The results Macko *et al.* obtained after introducing the stainless steel plate are striking. Close to the plate, the surface developed into an array of nanoholes, a topography which had previously been observed during ion bombardment using an alternating cold cathode source.[34] Further from the plate, they observed clear ripple patterns. At greater distances from the plate, they observed weakly ordered arrays of nanodots. At the greatest distances, where the Fe deposition was expected to be negligible, only surface smoothing was observed.

These results constitute strong evidence that a great number of patterns that have been observed in IBS experiments could be generated simply by adjusting the impurity deposition flux and/or incidence angle. Along with the results of Ozaydin *et al.*[28] and other systematic studies of deposition to be discussed below, Macko *et al.* helped to bring clarity to the apparently contradictory experimental IBS results obtained previously.

Another excellent systematic study of the effect of impurity flux and incidence angle was provided the following year by Zhang *et al.*[31] In that work, the authors examined normal incidence 5 keV Xe^+ ion bombardment of Si. Like Macko *et al.*, they mounted a stainless steel plate to one end of the sample, and additionally allowed the angle of this plate to vary with respect to the surface normal of the Si sample. The qualitative results of this study agreed with Macko *et al.*, and additionally the experimenters were able to identify a threshold deposition fluence for pattern formation on the order of 10^{15} ions per cm^2.

While the work in Refs. [30] and [31] helped to clarify the role of Fe impurities in IBS pattern formation, both experiments suffered from the same fundamental limitation: the deposition flux was due to sputtering from the fixed stainless steel plate, and thus the deposition flux was always dependent on the bombardment flux. In 2011, Macko *et al.*[33] circumvented this limitation by evaporating Fe directly onto the surface, allowing the authors to investigate the effects of ion and

impurity fluence independently. In addition to confirming the qualitative dependence on deposition fluence found previously, the authors of Ref. [83] demonstrated through *ex situ* transmission electron microscopy (TEM) images that iron compounds were building up on the side of the nanostructures facing the deposition source, as had been suggested previously. Furthermore, they verified that these results apply over the range of temperatures 140° C $<$T$<$ 440° C.

At this point, it was clear to researchers in the IBS field that Fe co-deposition was an important factor in determining surface morphologies, and that many of the ostensibly contradictory results obtained previously could be explained by inadvertent deposition of impurities. However, the question "why does Fe deposition affect the surface morphology so much?" had yet to be conclusively answered. The experimental setups described so far have left open the possibility that shadowing played a crucial role, since Refs. [80] and [81] had some deposited atoms impacting the surface at grazing angles of incidence, and even Ref. [83] had a deposition angle of -75°, which is large enough to admit the possibility of shadowing for some of their observations. Other proposed mechanisms included phase separation of materials at the surface or preferential sputtering due to silicide formation. We will discuss theories of phase separation and preferential sputtering in this context in Section 2.7.

The importance of silicide formation was established conclusively by Hofsass *et al.*[82] and Engler *et al.*[83] In the case of the former, an experimental setup similar to previous work[81,80,33,31] was employed using a variety of metals. When this plate was composed of Fe, Ni, or Cu (metals which spontaneously form silicides), the patterns were qualitatively similar to those observed previously. However, when the plate was composed of W, Pt, or Ag (metals which do not form silicides), only surface smoothing was observed. Similarly, Engler *et al.*[83] used ion sputtering to deposit Pd, Ir, Ag, and Pb onto an ion bombarded Si surface. Although Pd and Ir have similar masses to Ag and Pb

respectively, only the former pair form silicides. The experimenters determined that the tendency of the deposited species to form a silicide was a necessary but not sufficient condition for pattern formation to occur.

Finally, it is worth noting that many of the conclusions reached in this section only apply provided the temperature is not too high. While Ref. [31] did not observe a strong temperature dependence over the range considered, if the thermal mobility of atoms on the surface exceeds their ion-induced mobility a strong temperature dependence will emerge.[84] Furthermore, experiments done at very high temperatures have displayed many morphologies not observed at lower temperatures, and appear to be strongly influenced by the underlying crystal structure. In Ref. [85], for example, bombardment and deposition at T= 660° C produced sponge, segmented wall, and pillar structures with very high aspect ratios. More recent work by Ou *et al.*[86] has shown that low energy IBS of GaAs at elevated temperatures ($T = 410°$ C) can produce extremely regular patterns. At lower temperatures, the ion beam produces an amorphous surface layer. By contrast, patterns obtained at elevated temperatures frequently reflect the underlying crystal structure.

2.2 Selected Uses for Patterns Made by IBS

It is impossible to say what the true breadth of application that patterns formed by IBS may someday be. The potential of IBS to create nanoscale order in an economical way over large areas is unmatched. In what follows, I give a description of a number of ways in which IBS is already being used, as well as potential future applications. While not all of the work cited in this section is directly applicable in industrial settings, my intention is to provide a subset of the ways in which IBS is used to further other materials science research.

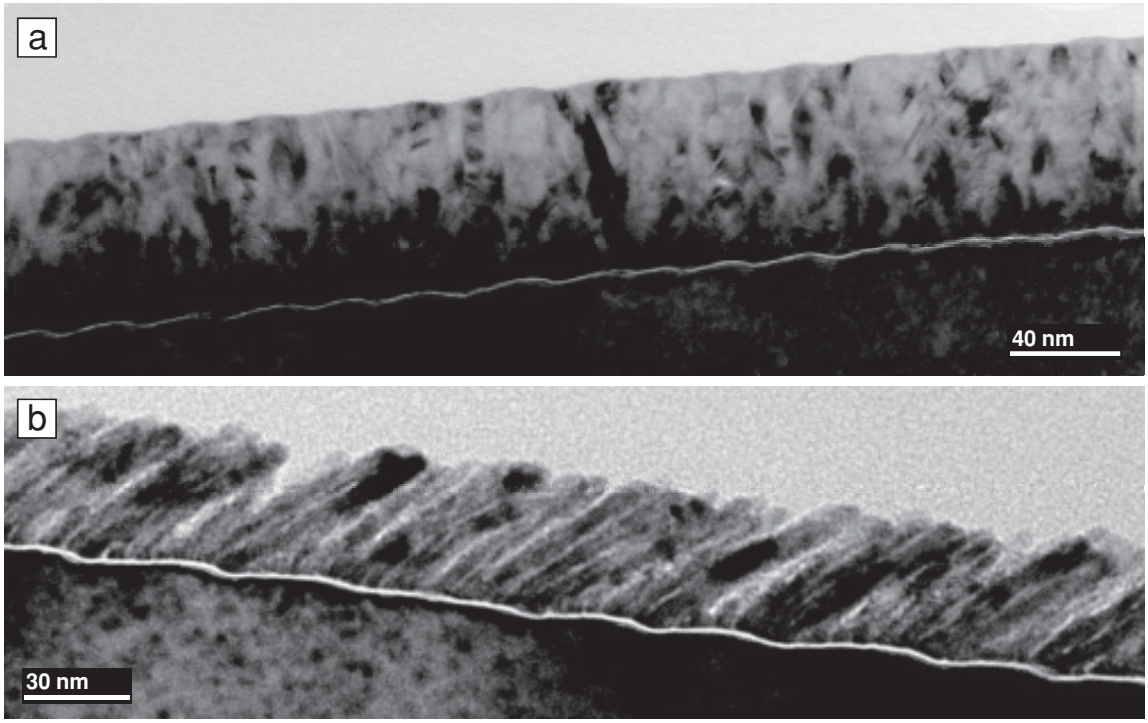

Fig. 2.12 TEM images of Al nanowires grown on a prepatterned substrate made by ion bombardment. The deposition beam was impinging on the sample at grazing incidence (from the right) and normal incidence in panels (a) and (b), respectively. Taken from Ref. [9].

One of the most common uses for Si surfaces with rippled topographies is as a template for developing patterns in other materials. Directional deposition on rippled surfaces has been used to create Al nanowires (see Fig. 2.12),[9] Co thin films which exhibited anisotropic island coalescence consistent with the anisotropy of the underlying ripples,[87] and Fe/Cr multilayer films.[1] The lattermost is an example of using IBS patterns as templates for magnetic thin films. The periodic structure makes the thin film's magnetic properties anisotropic.[88,89,90] Other groups have focused on making Si nanowires on insulators using IBS.[91] Ripple patterns are also a good template for growing carbon nanotubes.[11]

Some experiments have used Ag vapor deposition on rippled Si targets produced by IBS to fabricate an array of Ag nanoparticles which exhibit anisotropic plasmon absorption (see Fig. 2.13).[92,93]

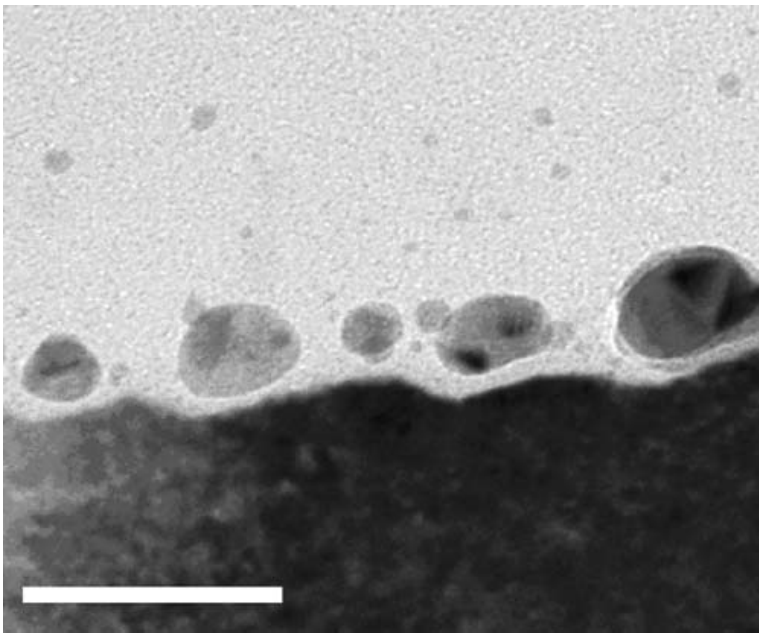

Fig. 2.13 TEM images of Ag nanoparticles on a rippled surface. Note that the nanoparticles tend to accumulate near the local minima in the surface height. The scale bar is 50 nm. Taken from Ref. [92].

In this case, because the Ag nanoparticles tend to bead up in the ripple valleys, they have a relatively consistent spacing in the direction parallel to the ripple wavevector. Because there is a well defined characteristic length in this direction, it is possible to observe resonance phenomena for incident light with the correct polarization to excite plasmons in the parallel direction. The reflectivity of a rippled Si surface with Ag beads has been seen to depend on the incident light polarization and angle of incidence in a way that is consistent with the expected behavior of a surface with anisotropic plasmon absorption. For a very similar reason, Ag vapor deposition on rippled Si surfaces has also been shown to exhibit enhanced Raman scattering.[94] Other Ag nanoparticle arrays are useful for investigating nonlinear optical properties.[2]

Some IBS experiments produces arrays of nanodots which resemble cones.[95,96,97,98] Arrays of these so-called "sputter cones" have found utility as anti-reflection coatings.[98,99,97] Rippled Si and TiO_2 surfaces have been used for biological applications since they are good at adsorbing

proteins.[100] Other researchers have demonstrated that ripple patterns in Si produced by IBS may be transferred onto organic compounds.[101] Other biological applications include fabricating nanofluidic channels,[102] making ultra-thin membranes,[103] and generating luminescent quantum dots for imaging cancer cells.[10]

IBS has been employed to produce blazed gratings for optical applications (see Fig. 2.14).[3,4,5,6,7,8] Later in this thesis I will explore recent theoretical work we have done towards the aim of using IBS to produce high efficiency multilayer blazed gratings. Our proposed fabrication procedure is currently being implemented by Professor Carmen Menoni and her collaborators.

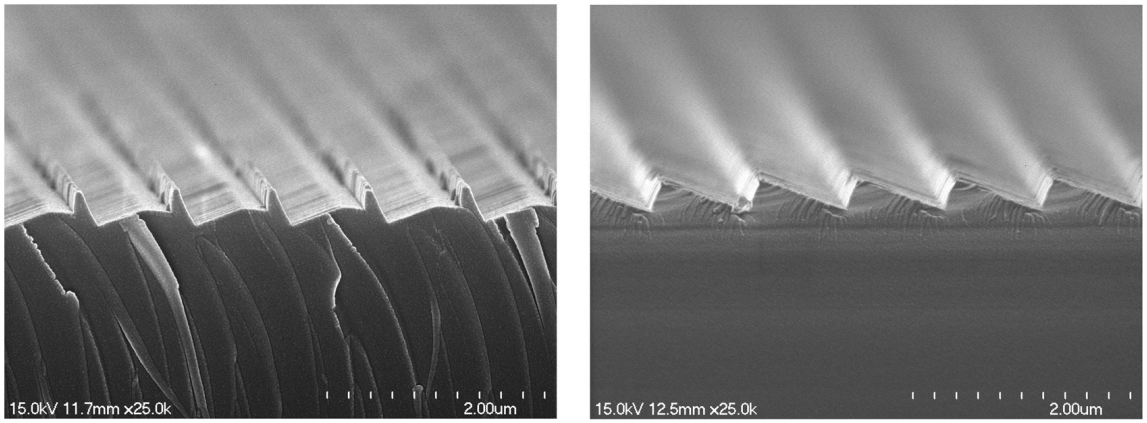

(a) (b)

Fig. 2.14 SEM images of a blazed grating made using ion bombardment. Panel (a) is after 240 seconds of bombardment, panel (b) is after 350 seconds. Taken from Ref. [8].

The complete scope of the applications of the nanopatterns produced by IBS has yet to be fully explored. As theory and experiment continue to improve, our ability to control the patterns is similarly expanded. It is my hope that the small subset of applications cited here is compelling enough reason to motivate the work contained in this thesis.

2.3 Theoretical Overview

Motivated by the multitude of experiments demonstrating the great promise of using IBS to produce highly ordered self organized nanoscale structures, there has been a great deal of theoretical work done in this field. In very broad terms we may organize theoretical approaches into three categories.

On the very finest level of analysis are molecular dynamics (MD) simulations. These simulations treat the solid surface being bombarded as a collection of atoms or molecules which interact via a particular potential. The specific form of this potential varies depending on the material being bombarded, ion energy, etc., but is generally the result of a detailed quantum mechanical calculation or *ab initio* methods.[104] In MD simulations, a specific collection of atoms or molecules (this collection is referred to as the 'target') is simulated in such a way that it has the desired macroscopic quantities (i.e. overall strain, crystallographic orientation, etc.). This target is then subjected to one or more ion impacts with assumed interaction potentials between the target constituents and the incident ion.

While MD simulations represent a description of ion bombardment on very small time and length scales, the computational power required for their implementation is substantial. Consequently, MD simulations are limited in their scope to targets which are small compared to the length scale of a typical pattern and time scales which are short compared to the running time of a typical experiment. In Chapter 3 we will see how some of the results of MD simulations can be extended to larger time and length scales.

A slightly coarser method of simulating an ion bombarded surface is known generically as the Monte Carlo (MC) method. In this approach, the complicated atom-atom and ion-atom interactions

considered in MD simulations are replaced with a discrete number of 'reactions', such as the production or translation of a crystal defect. Rather than computing pairwise interactions for a large number of particles, MC methods statistically sample these reactions to model the overall evolution of the sample. This approach has the advantage of a substantial improvement in computation time, but requires a significant amount of information (or assumed information) about the motion of defects in the surface. A very successful implementation of MC methods is *Transport of Ions in Matter*,[105] which is based on the Binary Collision Approximation.[106]

At the largest length scales and longest timescales are the continuum theories. These theories suppress the discrete nature of the target and impacting ions and instead describe the surface above a point (x,y) at time t as a continuous height field $h(x,y,t)$. The dynamics of the surface are governed by its spatial derivatives according to a local equation of motion (EOM) of the form

$$h_t = -v_0 + v_0' h_x + S_x h_{xx} + S_y h_{yy} + \ldots \tag{2.1}$$

where the subscripts on h denote partial derivatives. The coefficients v_0, v_0', etc. and the particular spatial derivatives considered are determined by a microscopic analysis of various physical effects. In the following section, we will give a detailed account of some of the continuum theories that have been proposed.

Continuum theories have several advantages over the MD and MC approaches to IBS surface science, not least of which is that they are frequently amenable to mathematical analysis. While most simulation techniques are capable of predicting the evolution of a surface given a particular initial condition and parameter set, some continuum theories may be solved generally. A general solution is valuable because it may be used to predict the surface morphology for any initial condition.

Furthermore, even when the EOM is sufficiently intractable that numerical integration is required, the continuum approach gives predictions for the surface over a large domain. This is essential for describing and controlling self organizing patterns, since our description of the surface must be at least of the same length scale as the pattern if it purports to describe the pattern in detail.

Despite these advantages, there are limitations to the continuum approach. For one, there is undoubtedly an error made in treating the surface as continuous, since the discrete nature of the atoms and impacting ions is a physical reality. Continuum approaches have been extended to incorporate nonlocal effects such as redeposition of the sputtered material and shadowing. In most cases, however, this is done at the expense of analytical tractability. There is also some amount of error resulting from retaining only a finite number of terms in the EOM. The retained terms are typically derived using an assumption that the surface height is slowly varying or that the theory applies only at early times. However, for patterns formed by IBS, these conditions do not always hold. Finally, as we will explore in the following section, the derivation of the EOM used for a particular theory is frequently based on an assumed microscopic model, and thus the continuum theory is likely only as good as the model upon which it is based. We will see in Chapter 3 how it is possible to generate a continuum model based on the results of MD simulations, which represents a promising way to circumvent this limitation.

2.4 Theories of Bombardment of Elemental Materials

2.4.1 Sigmund Model

Any discussion of IBS theory must begin with the work of Peter Sigmund.[14] In his seminal paper in 1973, he introduced a model for ions striking a solid surface and sputtering material

away. For ions with energy less than approximately 20 KeV, the Sigmund model predicts that the energy of an impacting ion is on average distributed among the atoms surrounding the impact point in an ellipsoidal fashion. Crucially, this ellipsoid is centered a distance below the solid surface comparable to the width of the ellipsoid.

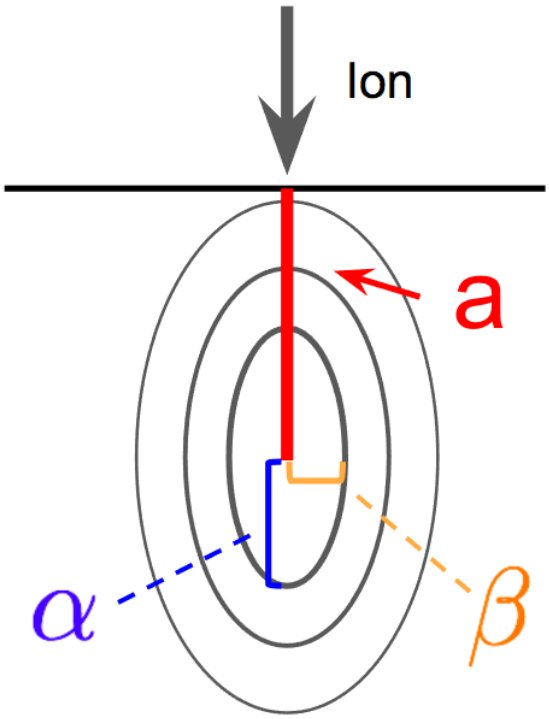

Fig. 2.15 An illustration of an ellipsoid described in the Sigmund model. The longitudinal and transverse length scales α and β, respectively, are labelled.

The exact theoretical prediction for the energy distribution of a single ion impact is in general quite complicated. As an ion penetrates the solid surface, its interaction with any given atom in the surface is determined by the scattering cross section of that atom. This process is inherently probabilistic. On average one expects that the ion will penetrate a finite nonzero distance before it is likely to significantly interact with any atoms in the solid. A typical ion-atom interaction leaves the affected atom with significant kinetic energy. This energetic atom is expected to move a short distance through the solid, losing energy due to atom-atom scattering events. A typical impacting

ion will collide with many atoms, which will in turn impact many more atoms. This process is known as a 'collision cascade'. This collision cascade constitutes the physical underpinnings for much of ion bombardment theory.

In the Sigmund model of sputtering, the collision cascade is assumed to adopt an ellipsoidal profile. For the special case in which an ion strikes a solid surface at normal incidence, the average energy distribution may be written as

$$E_D(x,y,z) = \frac{\varepsilon}{(2\pi)^{\frac{3}{2}}\alpha\beta^2} \exp\left[-\frac{(z+a)^2}{2\alpha^2} - \frac{x^2+y^2}{2\beta^2}\right], \tag{2.2}$$

where ε is the ion energy, a, α, and β are material constants with dimensions of length, and the $(x,y,z) = (0,0,0)$ is the point at which the ion begins to penetrate the surface. In order to make predictions for the sputtering of the target, Sigmund introduced the reasonable assumption that the rate at which material is sputtered at a point on the surface is proportional to the amount of power deposited at that point. Based on the exact shape of the ellipsoidal energy distribution he could then develop a prediction for the sputter yield as a function of incidence angle.

It is worth noting that despite the great success of the Sigmund model, it does not apply to all experimental situations. For high incident ion energies the dominant mode of interaction with the solid becomes electronic, rather than nuclear, stopping. In this energy regime, the so-called 'thermal spike' model is more appropriate.[107,108,109,110,111] For materials which maintain a high degree of crystallinity during IBS, such as metals, the crystallographic orientation can have a significant impact on the sputter yield due to effects such as ion channeling.[112] For high angles of incidence, effects such as ion reflection limit the accuracy of the Sigmund description.[113] Finally, the parameters describing the precise dimensions of the ellipsoids are difficult to access experimentally,

somewhat limiting the model's predictive capacity. For a quantitative investigation into the accuracy of the Sigmund model, see Ref. [l14]. Despite its limitations, since its introduction nearly half a century ago the Sigmund model has been a very successful and widely cited description of IBS.

2.5 Linear Continuum Theories

2.5.1 Bradley-Harper Theory

While the Sigmund model established an atomic-scale model by which ions sputter material from a solid surface, the formation of nontrivial patterns by IBS remained an unsolved mystery for another two decades. In 1988 the unveiling of the Bradley-Harper (BH) theory[13] marked a substantial breakthrough and the start of continuum theories being used to describe self organized patterns made by IBS. This foundational work continues to be cited by nearly every researcher in the field. The truly revolutionary aspect of the BH theory was that it was able to explain how a nominally flat surface could spontaneously evolve into a rippled structure with a characteristic length scale. It was also able to explain the rotation of these ripples at a finite angle of incidence as well as their propagation along the surface. In the years since the BH theory was introduced it has been extended in a variety of ways.[115,116,117,118,119,120,121,122,123,124]

The essence of the instability described by the BH theory relies on three properties of the Sigmund model: The energy is deposited in an ellipsoidal fashion about a point in the solid, these ellipsoids are not centered on the surface itself, and the rate of material sputtering is proportional to the energy deposited at the surface. An illustrative simple case is the sputtering of a sinusoidal crest (see Fig. 2.16) or trough (see Fig. 2.17) due to normal incidence IBS. The centers of energy deposition due to off-center impacts are closer to the base of the trough than the pinnacle of the

crest. Consequently, the sputtering is greater at low points than high points, and the amplitude of a ripple pattern will grow in time.

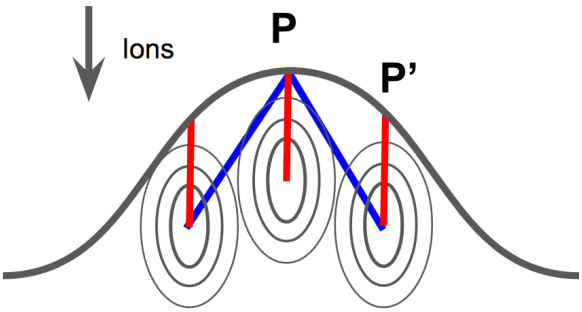

Fig. 2.16 An illustration of the BH mechanism at a local maximum of the surface. The center of the ellipsoid below the point P' is further from the point P than for the case shown in Fig. 2.17.

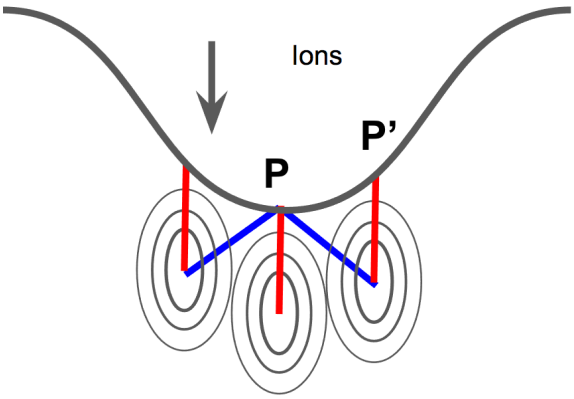

Fig. 2.17 An illustration of the BH mechanism at a local minimum of the surface. The center of the ellipsoid below the point P' is closer to the point P than for the case shown in Fig. 2.16.

In order to make quantitative predictions for the patterns which result from IBS, Bradley and Harper began with the Gaussian energy deposition given by Eq. (2.2) and applied it to a surface with a slowly varying height and with nonzero local curvature. We shall reproduce the results of their original analysis using the more recent approach developed by Bradley in 2011.[125] We are interested in the recession velocity of a surface point $\vec{r} \equiv x\hat{x} + y\hat{y} + h(x,y,t)\hat{z}$ due to nearby ion impacts. Let $-\hat{e}$ be the unit vector corresponding to the direction of the incident ion flux, and let $\vec{r}' \equiv x'\hat{x} + y'\hat{y} + h(x',y',t)\hat{z}$ be the location of a given ion impact. Denoting the ion energy as ε, we

may write the energy deposited at $\vec{r}$ due to an impact at $\vec{r}'$ as

$$E_D(x,y,z) = \frac{\varepsilon}{(2\pi)^{\frac{3}{2}}\alpha\beta^2}\exp\left[-\frac{\rho_\parallel^2}{2\alpha^2}-\frac{\rho_\perp^2}{2\beta^2}\right], \tag{2.3}$$

where

$$\vec{\rho} \equiv \vec{r}-\vec{r}'+a\hat{e}, \tag{2.4}$$

$$\rho_\parallel \equiv \vec{\rho}\cdot\hat{e}, \tag{2.5}$$

and

$$\rho_\perp \equiv \sqrt{\rho^2-\rho_\parallel^2}. \tag{2.6}$$

Having determined the energy per ion impact as a function of $\vec{r}$ and $\vec{r}'$, we may now write the power per unit volume at $\vec{r}$ and time t as a result of ions impacting an area element dA' centered on $\vec{r}'$. This power is denoted $P(\vec{r},\vec{r}',t)dA'$, and the ion beam flux is denoted by J. Defining

$$X \equiv x-x',$$

$$Y \equiv y-y',$$

and

$$H \equiv h(x,y,t)-h(x',y',t), \tag{2.7}$$

we have

$$\begin{aligned} P(\vec{r},\vec{r}',t) &= \frac{J\varepsilon}{(2\pi)^{\frac{3}{2}}\alpha\beta^2}\left[\cos\theta - h_{x'}(x',y',t)\sin\theta\right] \\ &\quad\times\exp\left[-\frac{(a+X\sin\theta+H\cos\theta)^2}{2\alpha^2}-\frac{(X\cos\theta-H\sin\theta)^2+Y^2}{2\beta^2}\right], \end{aligned} \tag{2.8}$$

where θ is the angle of incidence of the ion beam with respect to the global surface normal. Equation (2.8) is the average power deposited at a point $\vec{r}$ due to an impact at a point $\vec{r}'$ on a surface described by the function $h(x,y,t)$. The recession velocity at the point $\vec{r}$ is assumed to be proportional to the total power deposited at $\vec{r}$ due to all ions impacting the surface. To determine the total power deposited at $\vec{r}$, we must integrate the right hand side (RHS) of Eq. (2.8) over all possible impact points $(x',y',h(x',y',t))$. We may write

$$h_t = -\Lambda\sqrt{1+(\nabla h)^2}\int_{-\infty}^{\infty}dx'\int_{-\infty}^{\infty}dy' P(\vec{r},\vec{r}',t), \tag{2.9}$$

where Λ is the constant of proportionality between the power deposited and the erosion velocity. The term $\sqrt{1+(\nabla h)^2}$ appears because the surface recedes in the direction of the local surface normal, and we must project this recession onto the z axis. Inserting Eq. (2.8) into Eq. (2.9), we obtain

$$\begin{aligned} h_t = -\frac{\Lambda J\varepsilon}{(2\pi)^{\frac{3}{2}}\alpha\beta^2}\sqrt{1+(\nabla h)^2}\int_{-\infty}^{\infty}dx'\int_{-\infty}^{\infty}dy'\left[\cos\theta - h_{x'}(x',y',t)\sin\theta\right] \\ \times\exp\left[-\frac{(a+X\sin\theta+H\cos\theta)^2}{2\alpha^2}-\frac{(X\cos\theta-H\sin\theta)^2+Y^2}{2\beta^2}\right]. \end{aligned} \tag{2.10}$$

Equation (2.10) is the fully nonlinear equation of motion for a surface governed by the Sigmund model. While it is accurate to all orders in the surface height, Eq. (2.10) is not amenable to analysis. In order to generate a theory which could accurately generate predictions about the patterns formed by ion bombardment, Bradley and Harper assumed that the surface height varied slowly over the range of a typical ion impact. In particular, they performed a Taylor expansion of $h = h(x,y,t)$ up to second order in x and y, centered around the point $\vec{r}$.

While this method was successful in producing a theory which predicted the spontaneous formation of ripples, and the prevalence of perpendicular mode ripples above a critical angle of incidence, there is a more efficient and less restrictive way to perform this calculation. We continue to follow the method demonstrated Bradley in 2011[125] by assuming that $h(x,y,t)$ has the form

$$h(x,y,t) = A_0 \exp\left[\imath\vec{k}\cdot\vec{x} + \sigma(\vec{k})t\right], \tag{2.11}$$

where $\vec{k} \equiv k_x\hat{x} + k_y\hat{y}$ is the wave vector of a ripple pattern and $\sigma(\vec{k})$ is the growth rate of the amplitude of such a pattern. Instead of assuming that the surface may be approximated by a Taylor expansion in real space, we assume that A_0 is small. Put another way, it is assumed that each Fourier mode of the surface is sufficiently small that it does not affect the time evolution of any other mode. It is this assumption that permits us to consider a single mode at a time (i.e. Eq. (2.11) is not a sum over all possible modes).

The task at hand is now to determine the value of $\sigma(\vec{k})$ for all $\vec{k}$. We are most interested in the growth of long wavelength modes, since experiments suggest that the ripple patterns which typically form have a very long wavelength relative to their amplitude. Any experiment which begins with a nominally flat initial condition satisfies this restriction at early times. Consequently, we perform a Taylor expansion in powers of k_x, k_y, and A_0. Our assumption of no interaction between modes requires that we truncate this expansion at first order in A_0. We are free to carry out the expansion to arbitrary orders in k_x and k_y. However, we will primarily be interested in the long wavelength (small $|\vec{k}|$) terms.

The details of this expansion are somewhat lengthy, and will not be reproduced here. Schematically, the result of this analysis will be the coefficients a_{mn} in the expression

$$\sigma(\vec{k}) = \sum_{n=0}^{N} \sum_{m=0}^{N} a_{mn}(\imath k_x)^n(\imath k_y)^m, \tag{2.12}$$

where N is the desired expansion order. Equation (2.12) may also be written as a real space equation of motion as

$$h_t = \left[\sum_{n=1}^{N} \sum_{m=0}^{N} a_{mn}(\partial_x)^n(\partial_y)^m \right] h. \tag{2.13}$$

The values for a_{mn} derived by this method are equivalent to those found by the original BH derivation for $N \leq 2$. Additionally, this method allows one to determine arbitrary a_{mn} without computing a higher order Taylor expansion of h in space.

The curvature dependent instability resulting from this analysis of the Sigmund model is only half of the story. Carrying Eq. (2.12) out to second order, and noting that $a_{01} = 0$ by symmetry we obtain

$$\sigma(\vec{k}) = a_{10}\imath k_x - a_{20}k_x^2 - a_{02}k_y^2. \tag{2.14}$$

If either a_{20} or a_{02} are negative the theory becomes ill-posed. In this case the growth rate becomes a strictly increasing function of k_x or k_y. This implies that infinitesimally short ripples will have an infinite growth rate. This violates our assumption that the amplitude of the patterns is small, the assumption that the wavelength of the pattern is large, and the assumption that we may approximate the atoms of our solid surface by a continuous height field.

In order to formulate a well posed theory, Bradley and Harper considered the effects of surface self-diffusion.[126] Physically, this effect results from atoms diffusing on the surface. Surface self-

diffusion causes surfaces to smooth over time, and affects short wavelengths much more than long wavelengths. The effect on the EOM is to add a term proportional to $-(k_x^2+k_y^2)^2$ to the RHS of Eq. (2.14) (or equivalently a term $-\nabla^2\nabla^2 h$ to the RHS of Eq. (2.13)). In the years since the BH theory was introduced it has been suggested that a fourth order smoothing term of this form could originate from ion-induced viscous flow.[127]

Regardless of its physical origin, the addition of a fourth order term changes the predictions of the theory significantly. Rather than a strictly increasing function of k_x or k_y for the case of negative a_{20} or a_{02}, respectively, the growth rate is now a fourth order polynomial that goes to $-\infty$ as $|\vec{k}|$ goes to ∞. The value of (k_x, k_y) which maximizes this polynomial is referred to as the "selected wavevector", and we expect, at least at early times, that the surface will develop a ripple pattern with this wavevector.

In one paper, BH developed a convincing explanation for two of the biggest outstanding mysteries in the field of ion bombardment pattern formation: Why do ripples of a particular wavelength spontaneously form, and why do these ripples rotate by 90° at a finite angle of ion beam incidence? The former is explained by a balance between a curvature dependent instability due to the Sigmund model of energy deposition and surface self diffusion. The latter is explained by the fact that a_{02} becomes more negative than a_{20} at a finite angle of incidence, which implies a rotation of the selected wavevector by 90°.

Despite these great triumphs, there still existed many outstanding questions following the introduction of BH theory. Experiments suggest that for near normal ion bombardment there is not any ripple formation (except for experiments in which a second atomic species was present at the surface). The BH theory predicts that ripples should spontaneously form under such conditions. Furthermore, as a linear theory, the BH theory is inherently unable to deal with intermediate or long

time dynamics. Clearly, the amplitude of the ripple patterns which form do not continue to grow exponentially without limit. By what mechanism is the growth of these patterns limited? We shall see some proposed answers to these issues in the following sections.

2.5.2 Carter-Vishnyakov Theory

Another linear continuum theory of ripple formation was proposed by Carter and Vishnyakov in 1996.[41] In this model, a nominally flat surface develops a rippled topography with increasing amplitude due to direct momentum transfer from the incident ions to the atoms near the surface of the solid. For the general case of an ion striking a surface, there is some projection of the momentum of the ion onto the surface tangent plane. Through collisions with the atoms as the ion is slowed to a stop, the ion transfers its momentum to the surface layer. This momentum transfer results in a net mass flux "uphill" on average if the global angle of incidence is $> 45^\circ$. The surface atomic flux uphill is greater than the flux downhill for angles $> 45^\circ$ because the uphill faces are struck by more ions on average due to the experiment geometry, as shown in Fig. 2.18. The effective flux for uphill faces is greater than the effective flux for downhill faces by a sufficient amount to overcome the fact that ion impacts on the downhill faces transfer a greater fraction of their momentum to the surface current. When the ion beam is normally incident, the CV mechanism is purely stabilizing (see Fig. 2.19). For all angles of incidence the CV mechanism is stabilizing in the transverse direction.

The Carter-Vishnyakov (CV) model produces an EOM that is similar to that of BH [Eq. (2.13)], but the expressions for the coefficients a_{20} and a_{02} differ substantially. In particular they may be written

$$a_{02} = CV_y \cos^2(\theta) \tag{2.15}$$

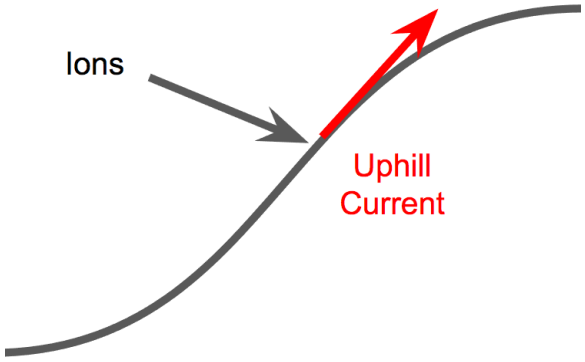

Fig. 2.18 An illustration of the CV mechanism when the incidence angle exceeds $\theta_c = 45°$.

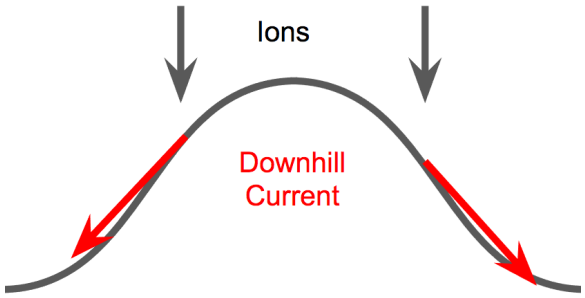

Fig. 2.19 An illustration of the CV mechanism when the ion beam is normally incident.

and

$$a_{20} = CV_x \cos(2\theta) \tag{2.16}$$

where CV_x and CV_y are positive constants that depend on the specific material, ion species, and ion energies involved. The CV model offers an explanation for the observed critical angle of incidence, below which the flat surface remains stable.[36,37,42] While the details of the instability will depend on the particular material being considered, if mass redistribution is the dominant destabilizing mechanism, the critical angle θ_c is expected to be universal. One criticism of the CV mechanism is that it cannot account for the formation of perpendicular-mode ripples, since $a_{02} > 0$ for all angles of incidence in the CV model.

In recent years there has been a great deal of discussion regarding the relative importance of sputtering (BH instability) and mass redistribution (CV instability) in describing pattern formation.[128,129,130,131,46,132,40,133,134,135,136,82,137,138] Some have gone as far as claiming sputtering is irrelevant,[132] while others have reached the opposite conclusion.[139] It seems certain that in all cases both mechanisms will be present, and that their relative importance is strongly dependent on the incident ion energy. In fact, below a certain energy threshold there can be no sputtering at all, so redistribution must dominate.[130,140] In the opposite limit, there is evidence that sputtering is far more important.[139]

2.6 Nonlinear Continuum Theories

While the linear BH and CV models provide descriptions of how a surface roughens from a nominally flat initial condition at early times, they both are incapable of describing the dynamics of the surface at later times. Since the EOMs produced by these models are linear, they predict a constant growth rate independent of ripple amplitude. This leads to ripple amplitudes which grow without limit, which is clearly unphysical. In reality, surfaces are typically observed to roughen exponentially at early times, followed by a period of coarsening and ripple amplitude saturation,[68,67,43] as discussed in Subsection 2.1.1. In what follows, we will describe some of the most successful attempts to incorporate nonlinear terms into models of IBS.

2.6.1 Kuramoto-Sivashinsky Equation

The most natural route to extending the linear BH model (subsection 2.5.1) is to carry out the expansion of the Sigmund model (subsection 2.4.1) to second order in ∇h, resulting in the well

known Kuramoto-Sivashinsky[141,142] (KS) equation,

$$h_t = -v_0 + v_0' h_x + S_x h_{xx} + S_y h_{yy} + B\nabla^4 h + \lambda_x h_x^2/2 + \lambda_y h_y^2/2. \tag{2.17}$$

Explicit expressions for the coefficients in Eq. (2.17) in terms of physical parameters in the Sigmund model were first determined by Cuerno and Barabasi.[115] This expansion may be obtained by first making the approximation that

$$h \simeq b_{10}X + b_{01}Y + \frac{b_{20}}{2}X^2 + b_{11}XY + \frac{b_{02}}{2}Y^2. \tag{2.18}$$

Next, one inserts Eq. (2.18) into Eq. (2.10). The resulting equation is then expanded to second order in b_{01} and b_{10}, and to first order in b_{20}, b_{11}, and b_{02}. The coefficients of this Taylor expansion correspond to the coefficients in Eq. (2.17). This Taylor expansion may be written

$$h_t \simeq v_0 + b_{10}v_0' + b_{20}S_x + b_{02}S_y + b_{10}^2\lambda_x + b_{01}^2\lambda_y, \tag{2.19}$$

and all odd powers of b_{01} and b_{11} do not contribute due to symmetry. By explicitly performing this expansion for the Sigmund model, Cuerno and Barabasi[115] obtained explicit expressions for the coeficients in Eq. (2.17). For notational convenience we consider the special case that $\alpha = \beta \equiv \sigma$, and define

$$\begin{aligned} s &\equiv \sin(\theta), \\ c &\equiv \cos(\theta), \\ a_\sigma &\equiv \frac{a}{\sigma}, \end{aligned}$$

and

$$F \equiv \frac{\varepsilon J \Lambda}{\sqrt{2\pi}} \exp\left[-\frac{a_\sigma^2}{2}\right]. \tag{2.20}$$

For the definitions of the physical quantities in Eqs. (2.20) see Subsections 2.4.1 and 2.5.1. For the special case being considered, the coefficients in Eq. (2.17) are given by

$$\begin{aligned}
v_0 &= \frac{Fc}{\sigma}, \\
v_0' &= \frac{Fs}{\sigma}\left(a_\sigma^2 c^2 - 1\right), \\
\lambda_x &= \frac{F}{\sigma} c \left[a_\sigma^2\left(3s^2 - c^2\right) - a_\sigma^4 s^2 c^2\right], \\
\lambda_y &= -\frac{Fc}{\sigma} a_\sigma^2 c^2, \\
S_x &= -\frac{F a_\sigma}{2}\left[2s^2 - c^2 - a_\sigma^2 s^2 c^2\right],
\end{aligned}$$

and

$$S_y = -\frac{F}{2} a_\sigma c^2$$

Since the work of Cuerno and Barabasi the KS equation has been extensively studied in the context of ion bombardment[116,117,119,120,121,122,123] The KS equation captures some of the essential features seen in ion bombardment experiments. It generates patterns that have a characteristic length scale, but which are not perfectly ordered. The amplitude of solutions to the KS equation saturates and averages to a constant in the long-time limit. There are many similarities between solutions to the KS equation and surfaces observed in ion bombardment experiments. These include apparently chaotic motion in space and time which nevertheless has a characteristic length, the scaling of the surface width as a function of time, and the absence of $u \to -u$ symmetry in the resulting patterns.

The KS equation will be prominently featured in Chapter 5. In that chapter we will see that the spatio-temporal chaos which is characteristic of solutions to the KS equation may be suppressed by periodically changing the value of the coefficient λ_x. In physical terms, this corresponds to rocking the sample periodically during ion bombardment.

2.6.2 Pearson-Bradley Theory

One common morphology observed in experiments is the so-called terraced state. Rather than a ripple pattern, at high fluences some surfaces develop into a state with two selected surface slopes. Furthermore, these surfaces seem to coarsen in time, increasing their amplitude and characteristic length according to a power law scaling for a finite time, after which they approach fixed values. Finally, they tend to propagate along the surface in a direction which is opposite that predicted by the BH theory.[53,54,56,57,143,58,59,60,62,63,52,27] For a discussion of experimental results demonstrating these phenomena, see Subsection 2.1.1.

Some have argued that carrying through the sputter yield to arbitrary angles of incidence is sufficient to explain the formation of terraced structures.[144,145,146,143] However this approach does not explain how the surface destabilizes in the first place.

Since these terraced topographies emerge for high fluence bombardment, it is unquestionable that the surface is in the regime where nonlinearities dominate the dynamics. There have been additional nonlinearities proposed to be relevant for IBS. The term $\partial_x^2 h_x^2$, for instance, produces surfaces which coarsen in time.[147,120] However this equation has been criticized due to the potential for the nonlinear terms to cancel out,[148] and the topographies which emerge from such a term are humps, not terraces. Therefore this term does not explain the phenomenon. This term has also been studied in the context of Aeolean sand dune formation.[149]

By carrying through the approximation of the sputter yield to third order in the surface slope h_x, Pearson and Bradley[65] obtained a modified version of the KS equation for IBS,

$$h_t = -v_0 + v_0' h_x - \kappa h_{xx} - B h_{xxxx} + \frac{c_1}{2} h_x^2 + \frac{c_2}{6} h_x^3, \tag{2.21}$$

where h is the height of the surface, v_0 is the erosion velocity of the unperturbed steady state, v_0', κ, B, c_2, and c_3 are constants, and the subscripts x and t on h denote partial derivatives. This equation is frequently referred to as the "3KS" equation. The solutions to this equation reproduce the essential features seen in experiments: The surface coarsens in time, with low amplitude, short wavelength ripple structures giving way to large amplitude, long wavelength sawtooth formations. This coarsening ceases at a finite time. The sawteeth have two clearly defined slopes which depend on the angle of incidence. At a finite time, the ripple propagation velocity may reverse direction as the cubic nonlinearity overtakes the linear term h_x. The terraced state emerges from a low amplitude noisy initial condition.

For the 1D case, Pearson and Bradley were able to show analytically that solutions to Eq. (2.21) develop undercompressive shocks. The predicted slopes and propagation velocities were in excellent agreement with numerical simulations. In Chapters 6 and 7, I will provide an extensive description of how the surface evolution predicted by this model of ion bombardment may be used to fabricate blazed gratings in a novel way.

2.7 Theories Regarding Systems With Multiple Atomic Species

As discussed previously, two of the most exciting areas of development in the IBS field are the closely related problems of bombarding a binary material and bombarding an elemental material with atomic co-deposition of a second species. The methods used to analyze these two situations are functionally nearly identical, and the two situations are very similar physically. In both cases it is important the the ions beam is composed of noble gas ions. A surface layer of altered composition also plays an important role when an elemental material is bombarded with a beam of non-volatile ions.

The phrase "surfactant sputtering" was coined by Hofsass[81] in 2008 to describe the co-deposition of material onto a bombarded elemental surface. Surfactant sputtering has received much theoretical interest. Kree et al.[150] explored the problem using Monte-Carlo simulations, while Bradley[151] analytically investigated the effect of compound formation on the morphology. Recent experiments[152] have shown that bombarding Ga with an Au ion beam can produce extremely well ordered ripple patterns. Other work suggests that surfactant sputtering can produce ripple instabilities which do not rely on a curvature dependent sputter yield[153] or that normal incidence IBS of a multicomponent surface may cause regular oscillations in the sputter yield.[154]

Virtually all of the theoretical work that has been done analyzing these multicomponent systems relies on the "two-field model". In this approach, the surface height (u) and chemical composition (ϕ) are two fields which describe the surface and their time evolution is in some way coupled. This coupling typically arises either from preferential sputtering (the chemical composition ϕ influences the local surface velocity u_t) or from amplification of the local deposition flux due to the local surface slope (regions of the surface with a local normal close to parallel to the deposition beam

will have more material deposited upon them than the average surface element, and will therefore be subject to a change in chemical composition ϕ and surface height u due to the increased effective deposition flux).

The first application of this particular two-field approach was provided by Shenoy et al.,[124] but was limited to a linear approximation. A significant improvement in this work was provided by Bradley and Shipman,[155, 156, 157] who were able to analyze the fully nonlinear equations of motion. Besides characterizing the qualitative behavior as a function of the free parameters, they were able show that for a critical range of a bifurcation parameter, the formation of ordered hexagonal arrays of nanodots could be predicted for normal incidence bombardment of a binary material, in agreement with experiment. In what follows I explore one theoretical explanation for the formation of nanoscale patterns in multi-component systems.

2.7.1 Preferential Sputtering

One proposed physical mechanism for ion-bombarded multi-component systems is the preferential sputtering of one material over another. It has long been known that different atomic species in a compound sputter at different rates under otherwise identical conditions. Suppose we have a binary compound of 50% material A and 50% material B, and that the sputter yield of A is strictly greater than the sputter yield of B. As the bombardment proceeds, atoms of material A are sputtered more often than those of material B. The result is an increase of the surface concentration of atoms of species B. The erosion rate of a point on the surface depends on the surface concentration in this case. A region which is rich in material A will recede more quickly than a region rich in material B. Because of this, we say that the surface height and composition are coupled to one another.[158, 155, 156, 159, 124]

To see how the coupling between the surface height and the composition may influence the surface morphology, I will follow a derivation provided by Bradley in 2012.[153] In this case, even if the instabilities due to mass redistribution, curvature dependent sputtering, and phase separation are absent, ripples may spontaneously form on the surface due entirely to preferential sputtering. This particular model is relevant to this thesis because it is considered as a special case in Chapter 4.

The situation we wish to consider is the following: A solid surface of material B is bombarded obliquely by a broad beam of noble gas ions at an angle θ. Concurrently, a beam depositing atomic species A is incident on the surface with angle θ_d. The fluxes of these two beams are such that, on average, the surface recedes. Define the quantities

$$\phi \equiv c - c_0 \tag{2.22}$$

and

$$u \equiv h - h_0 + v_0 t, \tag{2.23}$$

where c_0 is the steady state concentration of material A, c is the local concentration of material A, h is the surface height, h_0 is the average height of the surface at $t = 0$, and v_0 is the steady state erosion velocity when $c = c_0$. The steady state is defined to be the case in which $h_x = 0$ for all t. In what follows, we will work to first order in u and ϕ. Furthermore, for simplicity we will suppress the dependence of the sputter yield Y on the local surface curvature. Denoting the deposition flux J_d, we may write the flux of material B onto the surface at any point as

$$F_d = J_d(\cos\theta_d - u_x \sin\theta_d). \tag{2.24}$$

Furthermore, we may write the flux of atoms of materials A and B sputtered by the ion beam as

$$F_A = J(\hat{e}\cdot\hat{n})(c_0+\phi)Y_A(\theta_{local}) \tag{2.25}$$

and

$$F_B = J(\hat{e}\cdot\hat{n})(1-c_0-\phi)Y_B(\theta_{local}), \tag{2.26}$$

respectively, where J is the ion beam flux, $\hat{n}$ is the local surface normal, $\hat{e}$ is the unit vector antiparallel to the incident ion beam, and $Y_i(\theta_{local})$ is the sputter yield of species i evaluated at the local angle of incidence (i.e. $\cos\theta_{local} = \hat{e}\cdot\hat{n}$). Working to first order in u and ϕ, Eqs. (2.25) and (2.26) may be written as

$$F_A = c_0 f_A(\theta) + f_A(\theta)\phi + c_0 f_A'(\theta)u_x \tag{2.27}$$

and

$$F_B = (1-c_0) f_B(\theta) + f_B(\theta)\phi + (1-c_0) f_B'(\theta)u_x, \tag{2.28}$$

where

$$f_i(\theta) \equiv J\cos\theta Y_i(\theta). \tag{2.29}$$

Finally, we consider the effects of radiation enhanced viscous flow near the surface.[127] This effect gives rise to a current for i =A,B which is given by

$$\vec{J_i} = K c_i \nabla\nabla^2 h, \tag{2.30}$$

where $c_A = c_0$, $c_B = 1 - c_0$, and K is a constant which depends on material parameters of the solid surface and the attributes of the ion beam. Using mass conservation, we may combine all of these physical effects into a pair of coupled equations of motion, given by

$$u_t = -\Omega \left[F_A + F_B - F_d + \nabla \cdot (\vec{J}_A + \vec{J}_B) \right] \tag{2.31}$$

and

$$\phi_t = -\frac{\Omega}{\Delta} \left[F_A - F_d + \nabla \cdot J_A \right], \tag{2.32}$$

where Δ is a characteristic length on the order of the ion penetration depth and Ω is the atomic volume (taken to be the same for A and B for simplicity). Inserting Eqs. (2.24), (2.27), and (2.28) into Eqs. (2.31) and (2.32) results in a coupled pair of EOMs for the variables u and ϕ. The substitutions required to render these EOMs dimensionless are rather straightforward, but are somewhat lengthy and do not offer additional insight into the effect being considered. Interested readers are directed to Ref. [153] for the omitted steps. The dimensionless forms of Eqs. (2.31) and (2.32) after the substitutions described above are

$$\tilde{u}_{\tilde{t}} = \tilde{\phi} + \tilde{v}\tilde{u}_{\tilde{x}} - \tilde{D}\tilde{\nabla}^2\tilde{\nabla}^2\tilde{u} \tag{2.33}$$

and

$$\tilde{\phi}_{\tilde{t}} = -\tilde{\phi} + \tilde{u}_{\tilde{x}} - \tilde{D}'\tilde{\nabla}^2\tilde{\nabla}^2\tilde{u}, \tag{2.34}$$

where $\tilde{D}$, $\tilde{D}'$, and $\tilde{v}$ are dimensionless constants. In what follows we will suppress the tildes. In order to find solutions to Eqs. (2.33) and (2.34), we look for sinusoidal oscillations in the surface

height and composition which have the same periodicity. The composition and height fluctuations may have different amplitudes and phases, however. Our ansatz takes the form

$$(u,\phi)^T = (u_*,\phi_*)^T \exp(\imath\vec{k}\cdot\vec{x}+\sigma t), \tag{2.35}$$

where u_* and ϕ_* are complex constants, $\vec{k}$ is the wavevector of the sinusoidal perturbation, the superscript T denotes the matrix transpose, and $\sigma = \sigma(\vec{k})$ is the linear growth rate. Inserting this ansatz into Eqs. (2.33) and (2.34) results in a quadratic equation for σ. The roots of this quadratic, and thus the two possible growth rates for a mode with wavevector $\vec{k} = (k_x,k_y)^T$, are given by

$$2\sigma_\pm = -(1-v\imath k_x + Dk^4) \pm \sqrt{(1-v\imath k_x + Dk^4)^2 + 4(\imath k_x - D'k^4)}, \tag{2.36}$$

where $k \equiv |\vec{k}|$. Remarkably, for $v > -1$, the real part of σ_+ is greater than zero. This implies that for small values of k_x there exists a linear instability. Purely due to the coupling between the surface composition and the surface height, ripple patterns will spontaneously form on the solid surface. While this is of course not true for all materials, it is a strong indication that the coupling between the composition and the surface height can have a strong influence on the surface morphology. This particular model is explored in greater detail in Chapter 4.

2.8 Numerical Methods

In what follows I provide a description of the method of numerical integration used widely throughout this work. While this method itself does not represent an original contribution, I did implement the 1D method from scratch in Python. Furthermore, given the extensive use of this algorithm in this work, I would be remiss in omitting a general description.

The method used is a particular extension of the exponential time differencing (ETD) scheme first developed by Cox and Matthews,[160] which is applicable to an equation of the form

$$\frac{\partial u}{\partial t} = \hat{L}u + \hat{N}(u,t), \tag{2.37}$$

where $u = u(x,t)$ is the dependent variable, t is time, $\hat{L}$ is a linear differential operator, and $\hat{N}(u,t)$ is a nonlinear operator. Since $\hat{L}$ is a linear differential operator, its eigenfunctions are plane waves. In what follows we will use the matrix representation of $\hat{L}$ in Fourier space. The goal is to find a solution for some time interval $t_0 < t < t_1$ given an initial state $u(x,t_0)$. The first step is to act from the left on Eq. (2.37) with the integrating factor $e^{-\hat{L}t}$. This gives

$$e^{-\hat{L}t}u_t - e^{-\hat{L}t}\hat{L}u = e^{-\hat{L}t}\hat{N}(u,t). \tag{2.38}$$

Using the definition

$$v \equiv e^{-\hat{L}t}u, \tag{2.39}$$

Eq. (2.38) may be written as

$$v_t = e^{-\hat{L}t}\hat{N}(e^{\hat{L}t}v,t). \tag{2.40}$$

These transformations have the effect of transforming Eq. (2.37) from a form which has a stiff linear part to one which is purely nonlinear. Since the left hand side (LHS) of Eq. (2.40) may be integrated exactly, the only approximations which must be made in this method is the integral over the right hand side (RHS) of Eq. (2.40) over one timestep. We will follow the notation of Cox and Matthews, and denote the length of one timestep by h. The integral from t_n to $t_n + h$ of Eq. (2.40)

may be written as

$$u(x,t_n+h) = e^{\hat{L}h}u(x,t_n) + e^{\hat{L}h}\int_0^h e^{-\hat{L}\tau}\hat{N}(u(x,t_n+\tau),t_n+\tau)d\tau. \tag{2.41}$$

The matrices $e^{\pm\hat{L}h}$ need only be calculated once for a given simulation, and thereafter the propagation of the linear terms is simply matrix multiplication. This makes this approach exceedingly fast compared to other methods without sacrificing accuracy. In order to approximate the integral on the RHS of Eq. (2.41), Cox and Matthews made use of the standard Runge-Kutta method.

While analytically the method developed by Cox and Matthews is well behaved for a general $\hat{L}$, it suffers from a numerical instability for linear operators which have very small eigenvalues. This particular numerical instability is well known to the community, and was efficiently surmounted by Kassam and Trefethen.[161] To understand the nature of the problem they circumvented, consider the expression

$$g(z) = \frac{e^z - 1}{z} \tag{2.42}$$

for $z \ll 1$. In the explicit prescription provided by Cox and Matthews, there appear many terms of this form (or terms which are similar and exhibit the same issue) where z corresponds to an eigenvalue of $\hat{L}$. Analytically one may Taylor expand $g(z)$ in powers of z and see that this term gives a finite result for all finite z. Numerically, however, issues arise due to the limits of floating point precision. If z is smaller than a threshold value, e^z incorrectly evaluates to 1, and so $g(z)$ evaluates to 0, and massive inaccuracies or overflows can result. If all of the eigenvalues of $\hat{L}$ are small, this problem may be corrected by replacing e^z with a Taylor series, truncating at the desired level of precision. However, a general operator $\hat{L}$ may have eigenvalues which are not all small, and thus any truncated series will be inaccurate for some eigenvalues. In the particular application of

models of an ion bombarded surface, the eigenvalues correspond to growth rates of different Fourier modes. Thus we expect some will be very close to zero while others will be large in magnitude. The solution discovered by Kassam and Trefethen is to evaluate expressions of the form of $g(z)$ which appear in Cox and Matthews' expressions by means of contour integration. In particular, they use the expression

$$f(\hat{L}) = \frac{1}{2\pi i}\int_{\Gamma} f(t)(t\hat{I} - \hat{L})^{-1} dt, \tag{2.43}$$

where Γ is a contour in the complex plane that encloses the eigenvalues of $\hat{L}$. This integral is easily approximated discretely, and sidesteps the numerical cancellations. Equation (2.43) may be used throughout the exponential time differencing algorithm, including accurately calculating the elements of the matrix $e^{\hat{L}h}$ [in this case f in Eq. (2.43) is given by $f(x) = \exp(hx)$]. With this innovation, one can take the explicit formulae provided by Cox and Matthews, accurately calculate the relevant matrices therein, and produce an algorithm which is very fast and accurate for a general $\hat{L}$ and N.

In order to solve 1D problems of the form of Eq. (2.37), I implemented this scheme in Python. Quantitative comparison was made with an existing form of this method implemented in Matlab, with very good agreement. This method offers a tremendous speed advantage over other methods, such as using built in ODE solvers on the associated dynamical system. In order to solve 2D equations, I have made use of the Python code developed by Dan Pearson. I am grateful for his willingness to share his work with me, and this 2D implementation has proven to be very fast and accurate as well.

CHAPTER 3

CRATER FUNCTIONS

3.1 Introduction

In Chapter 2 we explored the linear continuum theories of BH and CV, which are based on simple models of sputtering and mass redistribution, respectively. It has been unclear just how good these models are and in what circumstances they can be reasonably applied. Moreover, the predictions of the BH and CV theories depend on a number of phenomenological parameters but give no means of computing their values.

Recently, there has been considerable interest in incorporating the results of molecular dynamics (MD) simulations into a continuum theory of ion-induced surface dynamics. The so-called crater function formalism (CFF) utilizes the average result of many ion impacts at a single point to generate a Green's function, which is then used to determine the response of a surface to bombardment with a broad ion beam.[12,132] This approach has the advantage that it takes into account both sputtering and ion-induced mass redistribution and does not rely on simple models of these phenomena. The formalism yields estimates of the constant coefficients that appear in the continuum equation of motion based on input from MD simulations. In the first application of this method to a specific physical problem, Norris *et al.* carried out MD simulations of the bombardment of a silicon surface with 100 and 250 eV Ar^+ ions and then used their CFF to obtain estimates of some of the coefficients in the equation of motion.[132]

The Green's function, which is usually referred to as the "crater function," depends on the complete shape of the surface surrounding the impact point.[12] However, because it is not possible to find the crater function for an arbitrarily shaped surface using MD, the shape dependence of the crater was simply neglected in Norris *et al.*'s study of the erosion of Si with an Ar^+ beam.[132] In particular, the crater function for a *flat* surface was used to estimate the coefficients in the equation of motion (EOM), even though the accuracy of such a procedure is questionable. The dependence of the crater on the shape of the surface has also been neglected in more recent applications of the CFF.[162, 163]

In this chapter, we extend the CFF so that it includes the dependence of the crater function on the curvature of the surface at the point of impact. We give explicit expressions for the coefficients in the equation of motion which reduce to the expressions given by Norris *et al.*[132] only if the curvature dependence of the crater function is neglected. We then demonstrate that our extended CFF yields the exact BH coefficients for the Sigmund model. In contrast, the BH coefficients are not recovered if the curvature dependence of the crater function is neglected. This uncontrolled approximation instead results in coefficients that are off by a factor of two for normal-incidence bombardment. Our results therefore strongly suggest that if reliable estimates of the coefficient values are to be obtained using the CFF, the curvature dependence of the crater function must be taken into account.

This chapter is organized as follows. We introduce the crater function and its arguments in Section 3.2. In Section 3.3, we use the crater function to determine the coefficients in the EOM for the special case in which the surface height does not vary in the direction transverse to the plane of the beam. In Section 3.4, we develop the geometric preliminaries required to extend our theory to fully three-dimensional surfaces. Section 3.5 generalizes the results of Section 3.3 to the case

in which the surface height varies in both the transverse and longitudinal directions. Section 3.6 contains an explicit demonstration that our extended CFF is in accord with the BH theory in the case of the Sigmund crater. In Section 3.7, we compare our theory to the CFF of Norris *et al.*[132] and demonstrate that for the Sigmund crater the latter produces coefficients that can differ significantly from their exact values. Additionally, we discuss the implications of our work, and place its results in context. Our findings are summarized in Section 3.8.

3.2 The Crater Function

Consider the bombardment of a solid elemental material with a broad ion beam. We will assume that the material is amorphous, or, if it is crystalline, that a layer at the surface of the solid is rendered amorphous by the ion bombardment. The sample surface will be taken to be nominally flat before the irradiation begins.

We define the $\hat{\boldsymbol{z}}$ direction to be the global vertical, normal to the macroscopic surface. $\hat{\boldsymbol{x}}$ is taken to be the direction of the projection of the incident ion beam onto the macroscopic surface, and $\hat{\boldsymbol{y}}$ is taken to be normal to the $x-z$ plane. The incident ion flux is $\boldsymbol{J} = J(\hat{\boldsymbol{x}}\sin\theta - \hat{\boldsymbol{z}}\cos\theta)$, where the angle of incidence θ is the angle between the global vertical and the incident beam, as shown in Fig. 1. An arbitrary point on the surface P is given by $\boldsymbol{r} = x\hat{\boldsymbol{x}} + y\hat{\boldsymbol{y}} + h(x,y)\hat{\boldsymbol{z}}$, where $h(x,y)$ is the height of the point above the $x-y$ plane. (For convenience, we will suppress the time dependence of h unless it is necessary to explicitly display it.)

Our goal is to evaluate $\partial h/\partial t$ at an arbitary point O on the solid surface at an arbitrary time $t > 0$. To that end, we will place the global origin at the position of O at time t, as shown in Fig. 1.

The global origin will be taken to be stationary, and it so will remain fixed as the surface point O moves either up or down.

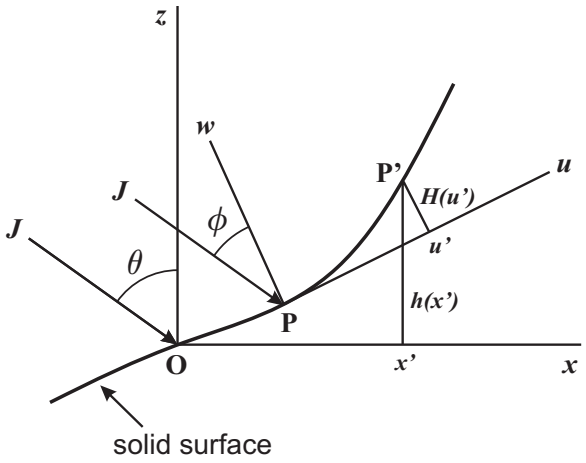

Fig. 3.1 The solid surface at time t. The points O, P and P' lie on the surface. The global frame of reference has its origin at O and has axes x, y and z, while the local frame of reference has its origin at P and has axes u, v and w. $\boldsymbol{J}$ is the incident ion flux. θ and ϕ are the global and local angles of incidence, respectively. The height of the point P' is $h(x')$ in the global frame but is $H(u')$ in the local frame. For simplicity, the figure has been drawn for the special case in which $h(x,y)$ is independent of y.

The collision cascade that an impinging ion produces in the solid has a characteristic lateral length scale that we will denote by l. We will assume that a smoothing mechanism ensures that the surface height varies only a little over this length scale; in practice, the smoothing mechanism could be thermally activated surface diffusion (as in the BH theory) or ion-induced viscous flow within a thin surface layer.[127] It is important to note that the equation of motion we will derive will *not* include the effects of the smoothing mechanism, since we will include only terms up to second order in the wave number k and the smoothing mechanism produces terms of order k^4.

Our first step in finding the surface velocity at O will be to determine the contribution to it coming from ions striking the surface an arbitrary surface point P. In fact, we may restrict our attention to points P that have a distance to O that is on the order of a few times l or less because ions

arriving at more remote points make a negligible contribution to the value of $\partial h/\partial t$ for $x = y = 0$. The height h is small for these points P. We will accordingly work to first order in h and its spatial derivatives throughout the remainder of the chapter.

In addition to the global coordinates x, y and z, it is convenient to introduce a set of local coordinates whose origin is the point P. Following Norris, Brenner and Aziz,[12] we define the vector $\hat{\boldsymbol{n}}$ to be the local surface normal at P and $\hat{\boldsymbol{t}}_u$ to be the local downbeam direction projected onto the surface. Explicitly,

$$\hat{\boldsymbol{n}} = \frac{\hat{\boldsymbol{z}} - \boldsymbol{\nabla} h}{\sqrt{1 + (\nabla h)^2}} \tag{3.1}$$

and

$$\hat{\boldsymbol{t}}_u = \frac{-\boldsymbol{J} + (\boldsymbol{J} \cdot \hat{\boldsymbol{n}})\hat{\boldsymbol{n}}}{|-\boldsymbol{J} + (\boldsymbol{J} \cdot \hat{\boldsymbol{n}})\hat{\boldsymbol{n}}|}. \tag{3.2}$$

$\hat{\boldsymbol{t}}_v$ is defined to be the cross product of $\hat{\boldsymbol{n}}$ and $\hat{\boldsymbol{t}}_u$. The unit vectors $\hat{\boldsymbol{n}}$, $\hat{\boldsymbol{t}}_u$ and $\hat{\boldsymbol{t}}_v$ form an orthonormal basis and $\hat{\boldsymbol{t}}_u$ and $\hat{\boldsymbol{t}}_v$ are tangent to the surface at P. The local angle of ion incidence, which will be denoted by ϕ, is given by $J\cos\phi = -\boldsymbol{J} \cdot \hat{\boldsymbol{n}}$. To first order in the spatial derivatives of the surface height,

$$\phi(x,y) = \theta - h_x(x,y), \tag{3.3}$$

where the subscript denotes a partial derivative with respect to x. Finally, we define u, v, and w to be the coordinates along the directions $\hat{\boldsymbol{t}}_u$, $\hat{\boldsymbol{t}}_v$ and $\hat{\boldsymbol{n}}$, respectively.

For surface points that have a distance to O that is on the order of l, we may approximate h by discarding terms of third order and higher terms from its Taylor series: We set $x_1 = x$, $x_2 = y$, and

$$h(x,y) = S_1 x + S_2 y + \frac{1}{2}K_{11}x^2 + K_{12}xy + \frac{1}{2}K_{22}y^2, \tag{3.4}$$

where

$$S_i \equiv \frac{\partial h}{\partial x_i}(0,0) \tag{3.5}$$

and

$$K_{ij} \equiv \frac{\partial^2 h}{\partial x_i \partial x_j}(0,0) \tag{3.6}$$

for $i, j = 1, 2$. While an arbitrary number of terms in the expansion (3.4) could in principle be retained, we will only keep terms up to quadratic order in x and y because the length scale of the height variation is assumed to be much larger than l. Note that the quantities S_i and K_{ij} are both of first order in h. This will be exploited later in our analysis.

We may also parameterize the surface in terms of the local coordinates u, v, and w. Close to P, the height of the solid surface above the $u-v$ plane is given by

$$H(u,v) = \frac{1}{2}E_{11}u^2 + E_{12}uv + \frac{1}{2}E_{22}v^2, \tag{3.7}$$

to second order in u and v. Here

$$E_{ij} \equiv \frac{\partial^2 H}{\partial u_i \partial u_j}(0,0), \tag{3.8}$$

where $u_1 \equiv u$, $u_2 \equiv v$ and $i, j = 1, 2$. Terms that are linear in u and v do not appear on the right-hand side of Eq. (3.8) because the u and v axes are tangent to the solid surface at the point P. The expansion (3.7) gives a good approximation to the value of H for O because the distance between O and P is of order l.

We now introduce the crater function

$$F = F(u, v, \phi, E_{11}, E_{12}, E_{22}), \tag{3.9}$$

which is defined to be minus the average change in the local surface height H above the point (u,v) in the $u-v$ plane as a result of a single ion impact at $u=v=0$, i.e., the point P. While two impacts may produce very different craters, by taking the statistical average of a great number of craters, we develop an expected response. The information required to construct F is assumed to be known *a priori* from another theory or from MD simulations.

The crater function $F(u,v,\phi,E_{11},E_{12},E_{22})$ is defined in the local coordinate system of the point of impact P. Its first two arguments are the lateral coordinates u and v in that coordinate system. The third argument of F is the local angle of incidence ϕ. Finally, we have included the dependence of the crater on the local curvatures E_{11}, E_{12} and E_{22}. This dependence was neglected by Norris *et al.*,[132] but, as we will discuss in Section 3.7, evidence from experiments[164] and MD simulations[165] suggests that it can have a significant effect.

Note that while the E_{ij}'s refer to second derivatives of H with respect to the local coordinates u and v at the point P, it is shown in Section IV that to first order they are equal to the corresponding second derivatives of h with respect to the global coordinates x and y at the point O, i.e.,

$$E_{ij} = K_{ij} \tag{3.10}$$

for $i,j=1,2$. We may therefore rewrite Eq. (3.9) as

$$F = F(u,v,\phi,K_{11},K_{12},K_{22}). \tag{3.11}$$

3.3 The Extended Crater Function Formalism in Two Dimensions

The goal of our analysis is to derive an EOM of the form

$$\begin{aligned}\frac{1}{J}\frac{\partial h}{\partial t} = \quad & C_0(\theta) + C_1(\theta)h_x + C_2(\theta)h_y \\ & + C_{11}(\theta)h_{xx} + C_{12}(\theta)h_{xy} + C_{22}(\theta)h_{yy},\end{aligned} \tag{3.12}$$

and to write the coefficients $C_0, C_1, \ldots, C_{22}$ in terms of the crater function F. The first step in our analysis will be to determine the contribution to the normal velocity of the surface at O due to impacts at the point P. Having found this, we will perform a flux weighted integral over all possible impact points P to determine the overall response.

To make the analysis as transparent as possible, we will begin by considering the special case in which the surface height h has no dependence on y. In this case, Eq. (3.12) reduces to

$$\frac{h_t}{J} = C_0(\theta) + C_1(\theta)h_x + C_{11}(\theta)h_{xx}, \tag{3.13}$$

where $h_t \equiv \partial h/\partial t$. This problem is equivalent to a two-dimensional (2D) problem in which h depends only on x and t and ions are incident in the $x-z$ plane with an angle of incidence θ. The effective crater function for this 2D problem is

$$g(u, \phi, E_{11}) \equiv \int_{-\infty}^{\infty} F(u, v, \phi, E_{11}, 0, 0)dy. \tag{3.14}$$

We will study the equivalent 2D problem for the remainder of this section.

Consider an impact at the point P whose position in the global coordinate system is $\boldsymbol{r} = x\hat{\boldsymbol{x}} + h(x)\hat{\boldsymbol{z}}$. The lateral position of the global origin O in the local reference frame of the impact

point is to first order

$$u = \hat{\boldsymbol{t}}_u(x) \cdot (\mathbf{0} - \boldsymbol{r}) = [\hat{\boldsymbol{x}} + h_x(x)\hat{\boldsymbol{z}}] \cdot [-x\hat{\boldsymbol{x}} - h(x)\hat{\boldsymbol{z}}] = -x. \tag{3.15}$$

Thus, to first order, we may replace the first argument of the crater function $g(u, \phi, E_{11})$ by $-x$. Similarly, the height of the origin O relative to the local frame of the impact point P is to first order

$$H(u) \equiv \hat{\boldsymbol{n}}(x) \cdot (\mathbf{0} - \boldsymbol{r}) = [-h_x(x)\hat{\boldsymbol{x}} + \hat{\boldsymbol{z}}] \cdot [-x\hat{\boldsymbol{x}} - h(x)\hat{\boldsymbol{z}}] = xh_x(x) - h(x). \tag{3.16}$$

Recall that the crater function gives the change in surface height in the direction of the local normal $\hat{\boldsymbol{n}}$, and so we must project the local normal velocity along the global vertical direction in order to find the velocity of the surface point O along the global vertical direction. However, because

$$\hat{\boldsymbol{n}}(x) \cdot \hat{\boldsymbol{z}} = 1 \tag{3.17}$$

to first order, this projection has no effect on the linearized EOM we will obtain.

This analysis permits us to write the time derivative of the surface height at O in terms of the crater function g and the ion flux J:

$$h_t(0,t) = -J \int g(-x, \phi, E_{11}) \cos\phi \, dx, \tag{3.18}$$

where the factor of $\cos\phi$ comes from projecting the ion flux onto the local normal at the point P. Finally, because only points P within a distance on the order of l from the origin give a significant contribution to the integral on the right-hand side of Eq. (3.18), we may replace E_{11} by $K \equiv K_{11}$ in the integral.

We are now in a position to begin analyzing the integrand in Eq. (3.18). To do so, we will linearize in the quantities $S \equiv S_1$ and K, which, as we noted earlier, are first order in h. This will yield expressions for the coefficients in the EOM (3.13). Making use of $\phi = \theta - h_x = \theta - S - Kx$, we see that

$$\begin{aligned} -J^{-1}h_t(0,t) = \quad & \int g(-x,\theta,0)\cos\theta dx \\ & + S\left[\frac{d}{dS}\int g(-x,\theta-S,0)\cos(\theta-S)dx\right]\Bigg|_{S=0} \\ & + K\left[\frac{d}{dK}\int g(-x,\theta-Kx,K)\cos(\theta-Kx)dx\right]\Bigg|_{K=0}. \end{aligned} \tag{3.19}$$

The first term on the right-hand side of Eq. (3.19) is particularly simple, and gives the steady-state erosion velocity. Notice that we may perform a change of variable $x \to -x$ without changing the overall sign of this term, i.e.,

$$\int g(-x,\theta,0)\cos\theta dx = \int g(x,\theta,0)\cos\theta dx. \tag{3.20}$$

Therefore, the steady-state erosion velocity for the undisturbed flat surface is

$$V_0(\theta) = J\cos\theta\int g(x,\theta,0)dx. \tag{3.21}$$

The second term on the right-hand side of Eq. (3.19) is somewhat more involved. Noticing that the only dependence of g upon S comes from the the local angle of incidence ϕ, it is clear that we may write the second term on the right-hand side of Eq. (3.19) as

$$S\left[\frac{d}{dS}\int g(-x,\theta-S,0)\cos(\theta-S)dx\right]\Bigg|_{S=0} = -S\frac{\partial}{\partial\theta}\int g(x,\theta,0)\cos\theta dx = -\frac{S}{J}\frac{\partial}{\partial\theta}V_0(\theta). \tag{3.22}$$

Finally, we turn to the dependence of h_t on K. The last term on the right-hand side of Eq. (3.19) becomes

$$\begin{aligned} & K\left[\frac{d}{dK}\int \quad g \quad (-x,\theta-Kx,K)\cos(\theta-Kx)dx\right]\Bigg|_{K=0} \\ = K\int dx\Big[& -x\sin\theta \quad g \quad (x,\theta,0)+x\cos\theta\frac{\partial g}{\partial\theta}(x,\theta,0)+\cos\theta\frac{\partial g}{\partial K}(x,\theta,K)\Big|_{K=0}\Big], \end{aligned} \tag{3.23}$$

where we have once again used the change of variable $x \to -x$.

Inserting Eqs. (3.21), (3.22) and (3.23) into Eq. (3.19), we arrive at an EOM of the form (3.13). Defining

$$M_K(\theta) = \int g(x,\theta,K)dx \tag{3.24}$$

and

$$M_x^{(n)}(\theta) = \int g(x,\theta,0)x^n dx, \tag{3.25}$$

we obtain

$$\begin{aligned} h_t(0,t) = \quad & -JM_x^{(0)}\cos\theta + J\frac{\partial}{\partial\theta}(M_x^{(0)}\cos\theta)h_x(0,t) \\ & -J\left[\frac{\partial}{\partial\theta}(M_x^{(1)}\cos\theta)+\cos\theta\frac{\partial}{\partial K}M_K\Big|_{K=0}\right]h_{xx}(0,t). \end{aligned} \tag{3.26}$$

Comparing this to Eq. (3.13), we see that

$$C_0(\theta) = -M_x^{(0)}\cos\theta, \tag{3.27}$$

$$C_1(\theta) = \frac{\partial}{\partial\theta}(M_x^{(0)}\cos\theta) = -\frac{\partial}{\partial\theta}C_0(\theta), \tag{3.28}$$

and

$$C_{11}(\theta) = -\frac{\partial}{\partial\theta}(M_x^{(1)}\cos\theta) - \cos\theta\frac{\partial}{\partial K_{11}}M_{K_{11}}\Big|_{K_{11}=0}. \tag{3.29}$$

The first term on the right-hand side of Eq. (3.29) stems from the fact that a nonzero surface curvature gives rise to a local angle of ion incidence that depends on the point of impact. The second is a direct result of the curvature dependence of the crater function itself.

3.4 Geometric Preliminaries In Three Dimensions

The extension of the analysis of the previous section to three dimensions (3D) is subtle and requires care. In this section, we delve into the relationship between the local and global coordinate systems before turning to the CFF in 3D. As discussed in Section II, the local coordinate system is defined using the local surface normal and the projection of the ion beam onto the local tangent plane.

To first order in h, the local unit vectors may be expressed in terms of their global counterparts as follows:

$$\hat{\boldsymbol{t}}_u = \hat{\boldsymbol{x}} - (h_y\cot\theta)\hat{\boldsymbol{y}} + h_x\hat{\boldsymbol{z}}, \tag{3.30}$$

$$\hat{\boldsymbol{t}}_v = (h_y\cot\theta)\hat{\boldsymbol{x}} + \hat{\boldsymbol{y}} + h_y\hat{\boldsymbol{z}}, \tag{3.31}$$

and

$$\hat{\boldsymbol{n}} = -h_x\hat{\boldsymbol{x}} - h_y\hat{\boldsymbol{y}} + \hat{\boldsymbol{z}}. \tag{3.32}$$

The partial derivatives of h are to be evaluated at the point (x,y) in the $x-y$ plane in these expressions. The coordinates of the point O in the local coordinate system (u, v and w) can now be found using Eqs. (3.30) - (3.32). The vector leading from P to O is $-\boldsymbol{r}$. Recalling that $\boldsymbol{r} = x\hat{\boldsymbol{x}} + y\hat{\boldsymbol{y}} + h(x,y)\hat{\boldsymbol{z}}$, we

obtain

$$u = -\boldsymbol{r}\cdot\hat{\boldsymbol{t}}_u = -x + yh_y\cot\theta, \tag{3.33}$$

$$v = -\boldsymbol{r}\cdot\hat{\boldsymbol{t}}_v = -y - xh_y\cot\theta, \tag{3.34}$$

and

$$w = -\boldsymbol{r}\cdot\hat{\boldsymbol{n}} = xh_x + yh_y - h \tag{3.35}$$

to first order. We may use Eq. (3.4) to eliminate h from Eqs. (3.33) - (3.35) because the surface height varies slowly between O and P. In particular, Eq. (3.35) yields

$$w = \frac{1}{2}K_{11}x^2 + K_{12}xy + \frac{1}{2}K_{22}y^2. \tag{3.36}$$

We are now prepared to demonstrate that Eq. (3.10) is valid. Inversion of Eqs. (3.33) and (3.34) gives

$$x = -u - vh_y\cot\theta \tag{3.37}$$

and

$$y = -v + uh_y\cot\theta. \tag{3.38}$$

Since $H = w$ and the K_{ij}'s are first order in h, Eq. (3.36) may now be written

$$\begin{aligned} H(u,v) = \quad & \frac{1}{2}K_{11}(u + vh_y\cot\theta)^2 + K_{12}(u + vh_y\cot\theta)(v - uh_y\cot\theta) \\ & + \frac{1}{2}K_{22}(v - uh_y\cot\theta)^2 \\ = \quad & \frac{1}{2}K_{11}u^2 + K_{12}uv + \frac{1}{2}K_{22}v^2. \end{aligned} \tag{3.39}$$

Taking the partial derivatives of H with respect to u_i and u_j, we arrive at the desired result, Eq. (3.10).

3.5 The Extended Crater Function Formalism in Three Dimensions

We will now utilize the results of Section 3.4 to obtain the coefficients of the EOM in three dimensions. To extend the formalism to the general case in which the surface height depends on y as well as x, we return to the crater function $F(u,v,\phi,E_{11},E_{12},E_{22})$, the generalization of $g(u,\phi,E_{11})$ to three dimensions. The EOM is

$$h_t = -J\int dx\int dy\cos\phi F(u,v,\phi,E_{11},E_{12},E_{22}). \tag{3.40}$$

Using Eqs. (3.3), (3.10), (3.33) and (3.34), we see that this may be written

$$h_t = -J\int dx\int dy\cos(\theta-h_x)F(-x+yh_y\cot\theta,-y-xh_y\cot\theta,\theta-h_x,K_{11},K_{12},K_{22}). \tag{3.41}$$

We now expand this to linear order in h and its derivatives, and let F_i denote the partial derivative of F with respect to its ith argument. This gives

$$\begin{aligned}-\frac{h_t}{J\cos\theta} = \int dx\int dy\Big\{ \quad & F(-x,-y,\theta,0,0,0)+F_1(-x,-y,\theta,0,0,0)(yh_y\cot\theta)\\ & +F_2(-x,-y,\theta,0,0,0)(-xh_y\cot\theta)\\ & -\sec\theta\frac{\partial}{\partial\theta}\left[\cos\theta F(-x,-y,\theta,0,0,0)h_x\right]\\ & +K_{11}F_4(-x,-y,\theta,0,0,0)+K_{12}F_5(-x,-y,\theta,0,0,0)\\ & +K_{22}F_6(-x,-y,\theta,0,0,0)\Big\}. \end{aligned}\tag{3.42}$$

To simplify this expression, we will examine it term by term and employ Eq. (3.4). The second term on the right-hand side of Eq. (3.42) is

$$I_2 \equiv \int dx \int dy F_1(-x,-y,\theta,0,0,0) y \cot\theta (S_2 + K_{12}x + K_{22}y). \tag{3.43}$$

I_2 is in fact zero. To see this, recall that we have assumed that the solid surface is amorphous. Independent of the details of the crater function $F(u,v,\phi,K_{11},K_{12},K_{22})$, therefore, symmetry demands that it be an even function of v if $K_{12} = 0$. Thus, the terms which are proportional to odd powers of y in the integrand of Eq. (3.43) integrate to zero. The remaining term in the integrand vanishes upon integration over x since

$$\int dx F_1(-x,-y,\theta,0,0,0) = F(-x,-y,\theta,0,0,0)|_{x=-\infty}^{x=\infty} = 0. \tag{3.44}$$

The third term on the right-hand side of Eq. (3.42) may be written

$$I_3 \equiv -\int dx \int dy F_2(-x,-y,\theta,0,0,0) x \cot\theta (S_2 + K_{12}x + K_{22}y). \tag{3.45}$$

Again using the symmetry of F, we see that $F_2(-x,-y,\theta,0,0,0)$ is an odd function of y, and thus the terms in the integrand that are proportional to even powers of y will integrate to zero. This leaves

$$\begin{aligned} I_3 &= -\cot\theta K_{22} \int dx \int dy F_2(-x,-y,\theta,0,0,0) xy \\ &= \cot\theta K_{22} \int dx \int dy F(x,y,\theta,0,0,0) x \\ &= \cot\theta K_{22} M_x^{(1)}, \end{aligned} \tag{3.46}$$

where we have integrated by parts and changed the dummy variables of integration from x to $-x$ and from y to $-y$.

The fourth term on the right-hand side of Eq. (3.42) is identical to the analogous term in the 2D case, except that h_x now contains the additional term $K_{12}y$. However, since $F(-x,-y,\theta,0,0,0)$ is an even function of y, this term makes no contribution.

Without additional assumptions or specific information about the crater function, the fifth and seventh terms on the right-hand side of Eq. (3.42) cannot be simplified further. However, we may eliminate the dependence of h_t on K_{12} using a symmetry argument. Notice that a surface described by $h(x,y) = K_{12}xy$ is invariant under the transformation $y \to -y$, $K_{12} \to -K_{12}$. We may thus write

$$F(x,y,\theta,0,K_{12},0) = F(x,-y,\theta,0,-K_{12},0). \tag{3.47}$$

It follows that I_6, the sixth term on the right-hand side of Eq. (3.42), is given by

$$\begin{aligned}\frac{I_6}{K_{12}} &= \left[\frac{\partial}{\partial K_{12}} \quad \int_{-\infty}^{\infty}dx\int_{-\infty}^{\infty}dyF(-x,-y,\theta,0,K_{12},0)\right]\Bigg|_{K_{12}=0} \\ &= \left\{\frac{\partial}{\partial K_{12}}\left[\quad \int_{-\infty}^{\infty}dx\int_{0}^{\infty}dyF(-x,-y,\theta,0,K_{12},0)\right.\right. \\ &\qquad \left.\left. +\int_{-\infty}^{\infty}dx\int_{0}^{\infty}dyF(-x,-y,\theta,0,-K_{12},0)\right]\right\}\Bigg|_{K_{12}=0}.\end{aligned} \tag{3.48}$$

The quantity in the square brackets in the later expression is an even function of K_{12}. As a consequence, I_6 vanishes and $C_{12} = 0$. We could have reached this conclusion *a priori* from Eq. (3.12): since the system is invariant under a reflection about the $x-z$ plane, h_t must also remain invariant under this transformation, which implies that $C_{12} = 0$.

We define

$$M_{K_{11}} = \int\int F(x,y,\theta,K_{11},0,0)dxdy, \tag{3.49}$$

$$M_{K_{22}} = \int\int F(x,y,\theta,0,0,K_{22})dxdy, \tag{3.50}$$

and

$$M_x^{(n)} = \int\int F(x,y,\theta,0,0,0)x^n dxdy. \tag{3.51}$$

Collecting terms, we arrive at a simpler form of Eq. (3.42),

$$\begin{aligned} -\frac{h_t(0,0,t)}{J\cos\theta} = \quad & M_x^{(0)} - S_1 \sec\theta \frac{\partial}{\partial\theta}(\cos\theta M_x^{(0)}) \\ & + K_{11}\left[\sec\theta\frac{\partial}{\partial\theta}\left(\cos\theta M_x^{(1)}\right) + \frac{\partial}{\partial K_{11}}M_{K_{11}}\Big|_{K_{11}=0}\right] \\ & + K_{22}\left[\cot\theta M_x^{(1)} + \frac{\partial}{\partial K_{22}}M_{K_{22}}\Big|_{K_{22}=0}\right]. \end{aligned} \tag{3.52}$$

Comparing this with Eq. (3.12), we conclude that Eqs. (3.27) - (3.29) remain valid, but the moments $M_{K_{11}}$ and $M_x^{(n)}$ are now given by Eqs. (3.49) and (3.51). We also have found that $C_2 = C_{12} = 0$ and that

$$C_{22}(\theta) = -\cos\theta\cot\theta M_x^{(1)} - \cos\theta\frac{\partial}{\partial K_{22}}M_{K_{22}}\Big|_{K_{22}=0}. \tag{3.53}$$

The first term on the right-hand side of Eq. (3.53) is present because if h_y is nonzero at the point of impact P, the local normal $\hat{\boldsymbol{n}}$ and the local downbeam direction $\hat{\boldsymbol{t}}_u$ have nonzero components along the y-direction. The second term results from the explicit dependence of the crater function on the curvature in the y-direction.

Despite the appearance of the factor of $\cot\theta$ in Eq. (3.53), $C_{22}(\theta)$ is well behaved in the limit $\theta \to 0$. To see this, note that for small θ,

$$M_x^{(1)}(\theta) \cong R_0 + R_1\theta, \tag{3.54}$$

where R_0 and R_1 are finite constants. Symmetry demands that $M_x^{(1)}(0) = 0$, and thus $R_0 = 0$. Therefore, in the limit of small θ, the lowest order term $M_x^{(1)}$ is proportional to θ. It follows that

$$\lim_{\theta\to 0}\left[\cos\theta\cot\theta M_x^{(1)}(\theta)\right] = R_1. \tag{3.55}$$

The value of the constant R_1 of course depends on the specifics of the crater being considered, but it is finite.

3.6 Application of the Formalism to the Sigmund Model

In this section, we demonstrate explicitly that our crater function formalism yields the exact BH coefficients for the Sigmund model. The crater function for the Sigmund model is given by Eq. (8) of Ref. [125]. For convenience, we will adopt the same notation that was used in that work. On average, an impact at the origin produces a crater whose negative depth at the point $\boldsymbol{r} = x\hat{\boldsymbol{x}} + y\hat{\boldsymbol{y}} + h(x,y)\hat{\boldsymbol{z}}$ is

$$F(x,y,\theta,K_{11},K_{12},K_{22}) = \frac{\varepsilon\Lambda}{(2\pi)^{3/2}\alpha\beta^2}\exp\left(-\frac{1}{2\alpha^2}[a - x\sin\theta + h(x,y)\cos\theta]^2 - \frac{1}{2\beta^2}[x\cos\theta + h(x,y)\sin\theta]^2 - \frac{1}{2\beta^2}y^2\right). \tag{3.56}$$

If the distance between the origin and $\boldsymbol{r}$ does not exceed a few times l, then we may set

$$h(x,y) = \frac{1}{2}K_{11}x^2 + K_{12}xy + \frac{1}{2}K_{22}y^2 \tag{3.57}$$

in Eq. (3.56). The dependence of the crater for the Sigmund model on the components K_{ij} of the curvature tensor becomes manifest once Eq. (3.57) has been inserted into Eq. (3.56).

For brevity, let

$$D \equiv \frac{a^2\varepsilon\Lambda}{(2\pi)^{3/2}\alpha\beta^2}. \tag{3.58}$$

We readily obtain

$$\begin{aligned} M_x^{(0)} &= D\int\int \exp\Big(-\frac{1}{2}a_\alpha^2(1-x\sin\theta)^2 - \frac{1}{2}a_\beta^2 x^2\cos^2\theta - \frac{1}{2}a_\beta^2 y^2\Big)dxdy \\ &= De^{-a_\alpha^2/2}\int\int \exp\Big(-\frac{B_1}{2}x^2 + Ax - \frac{a_\beta^2}{2}y^2\Big)dxdy \\ &= De^{-a_\alpha^2/2}\frac{2\pi}{a_\beta\sqrt{B_1}}\exp\left(\frac{A^2}{2B_1}\right) \end{aligned} \tag{3.59}$$

and

$$\begin{aligned} M_x^{(1)} &= aDe^{-a_\alpha^2/2}\int\int x\exp\left(-\frac{B_1}{2}x^2 + Ax - \frac{a_\beta^2}{2}y^2\right)dxdy \\ &= \frac{aA}{B_1}M_x^{(0)}. \end{aligned} \tag{3.60}$$

To find C_{11} and C_{22}, we need the partial derivatives of the curvature dependent moments $M_{K_{22}}$ and $M_{K_{22}}$ with respect to K_{11} and K_{22}, respectively. Since the K_{ij}'s do not depend on x and y, we may

exchange differentiation with respect to the K_{ij}'s with integration over x and y. This gives

$$\begin{aligned}\frac{\partial}{\partial K_{11}} \quad & M_{K_{11}}\Big|_{K_{11}=0} = \int\int \frac{\partial}{\partial K_{11}} F(x,y,\theta,K_{11},0,0)\Big|_{K_{11}=0} dxdy \\ & = -aDe^{-a_\alpha^2/2} \int\int \exp\left(-\frac{B_1}{2}x^2 + Ax - \frac{a_\beta^2}{2}y^2\right)\left(\frac{B_2}{2}x^2 + Cx^3\right) dxdy \\ & = -aM_x^{(0)}\left(\frac{A^2B_2}{2B_1^2} + \frac{A^3C}{B_1^3} + \frac{B_2}{2B_1} + \frac{3AC}{B_1^2}\right). \end{aligned} \tag{3.61}$$

Similarly,

$$\begin{aligned}\frac{\partial}{\partial K_{22}} \quad & M_{K_{22}}\Big|_{K_{22}=0} = \int\int \frac{\partial}{\partial K_{22}} F(x,y,\theta,0,0,K_{22})\Big|_{K_{22}=0} dxdy \\ & = -aDe^{-a_\alpha^2/2} \int\int \exp\Big(-\frac{B_1}{2}x^2 + Ax - \frac{a_\beta^2}{2}y^2\Big)\Big(\frac{B_2}{2}y^2 + Cxy^2\Big) dxdy \\ & = -M_x^{(0)}\frac{a}{a_\beta^2}\Big(\frac{B_2}{2} + \frac{AC}{B_1}\Big). \end{aligned} \tag{3.62}$$

We must also compute the derivative of $M_x^{(1)}\cos\theta$ with respect to θ. We obtain

$$\begin{aligned}\frac{\partial(M_x^{(1)}\cos\theta)}{\partial\theta} = \quad & \frac{\partial}{\partial\theta}\left(\frac{aA}{B_1}M_x^{(0)}\cos\theta\right) \\ = \quad & -aM_x^{(0)}\left[\frac{A\sin\theta}{B_1} - \cos\theta\left(\frac{B_2}{B_1} + \frac{6AC}{B_1^2} + \frac{A^2B_2}{B_1^2} + \frac{2A^3C}{B_1^3}\right)\right]. \end{aligned} \tag{3.63}$$

Finally, we will need the identity

$$\frac{1}{a_\beta^2}\Big(B_2 + \frac{2AC}{B_1}\Big) = \cot\theta\frac{A}{B_1}. \tag{3.64}$$

Inserting Eqs. (3.61) and (3.63) into Eq. (3.29) yields

$$C_{11}(\theta) = aM_x^{(0)}\left[\frac{A\sin\theta}{B_1} - \frac{\cos\theta}{2}\left(\frac{B_2}{B_1} + \frac{6AC}{B_1^2} + \frac{A^2B_2}{B_1^2} + \frac{2A^3C}{B_1^3}\right)\right]. \tag{3.65}$$

Similarly, inserting Eqs. (3.60) and (3.62) into Eq. (3.53) and applying the identity (3.64), we have

$$\begin{aligned} C_{22}(\theta) = \quad & -aM_x^{(0)}\left[-\frac{1}{a_\beta^2}\left(\frac{B_2}{2}+\frac{AC}{B_1}\right)+\cot\theta\,\frac{A}{B_1}\right]\cos\theta \\ = \quad & -M_x^{(0)}\,\frac{a}{a_\beta^2}\left(\frac{B_2}{2}+\frac{AC}{B_1}\right)\cos\theta. \end{aligned} \tag{3.66}$$

Note as well that explicit expressions for C_0 and C_1 can be obtained by inserting Eq. (3.60) into Eqs. (3.27) and (3.28). The resulting expressions for C_0 and C_1 and Eqs. (3.65) and (3.66) for C_{11} and C_{22} agree with the results obtained by BH for the Sigmund model.

3.7 Discussion

The key results of this chapter are given by Eqs. (3.29) and (3.53). These equations give a means of computing the coefficients C_{11} and C_{22} if the curvature dependent crater function is known. These coefficients play a key role in determining whether parallel-mode or perpendicular-mode ripples form or if the surface remains flat.

In their 2011 paper, Norris *et al.*[132] gave explicit expressions for C_{11} and C_{22}, namely

$$C_{11}(\theta) = -\frac{d}{d\theta}\left[M_x^{(1)}(\theta)\cos\theta\right], \tag{3.67}$$

and

$$C_{22}(\theta) = -M_x^{(1)}(\theta)\cos\theta\cot\theta. \tag{3.68}$$

Our results Eqs. (3.29) and (3.53) show that Eqs. (3.67) and (3.68) are a good approximation only if the curvature dependence of the crater function is negligible.

In the Sigmund model of ion sputtering, the form of the crater depends on the curvature of the surface at the point of impact, despite a statement to the contrary in Ref. [12]. This point has been discussed in detail by Nietiadi and Urbassek.[165] The second terms on the right-hand sides of Eqs. (3.29) and (3.53) therefore yield nonzero contributions to C_{11} and C_{22}. These contributions were computed explicitly in the preceding section.

For normal-incidence ion bombardment, the values of C_{11} and C_{22} obtained by neglecting the curvature dependence of the crater function [Eqs. (3.67) and (3.68)] differ by a factor of two from the exact values for the Sigmund model [Eqs. (3.65) and (3.66)]. In fact, Norris *et al.*'s result for C_{22} is equal to twice the exact value for all angles of incidence θ.

To get an idea of how much Eq. (3.67) differs from the exact result for the Sigmund model for nonzero values of θ, see Fig. 2. The values of a, α and β used in that figure are for 1 keV Ar^+ bombardment of silicon.[46] The ratio of C_{11} as given by Eq. (3.67) to the exact value is greater than two for a broad range of θ values. For $\theta = 45^\circ$, for example, the ratio exceeds 3.5. The angle where the switch from parallel- to perpendicular-mode ripples occurs is 50.8° but, if we use Eqs. (3.67) and (3.68), this angle is found to be 66.7°, fully 15.9° higher than the correct value.

Recently, Nietiadi and Urbassek carried out MD simulations of the bombardment of an amorphous silicon target with a normally-incident 500 eV Ar^+ beam.[165] They found that the craters for curved surfaces are substantially different than those for a flat surface. These observations and our results for the Sigmund model lead us to the conclusion that the errors incurred by neglecting the curvature dependence of the crater function are typically not small.

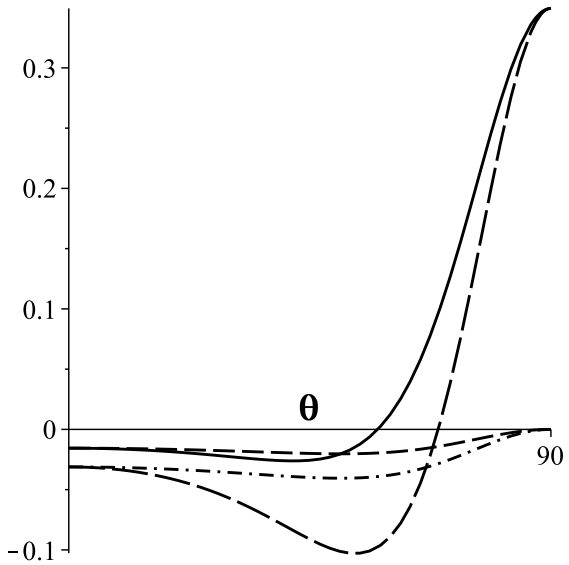

Fig. 3.2 The coefficients C_{11} and C_{22} as functions of θ for the Sigmund model. The exact results for C_{11} and C_{22} are shown with a solid and dashed curve, respectively. The results obtained for C_{11} and C_{22} if the curvature dependence of the crater function is neglected are shown with long dashes and with a dash-dotted curve, respectively. The values of a, α and β employed are for 1 keV Ar^+ bombardment of silicon. The coefficients are in units of $2\sqrt{2\pi}/(\Lambda\varepsilon a_\alpha^3 a_\beta)$ and θ is given in degrees.

The contribution to C_{ii} that comes from the curvature dependence of the crater function is $F_i \cos\theta$, where

$$F_i \equiv -\frac{\partial}{\partial K_{ii}} M_{K_{ii}}\Big|_{K_{ii}=0} \tag{3.69}$$

for $i = 1, 2$. If K_{ii} is initially zero and then becomes negative, the surface of the solid nears the core of the collision cascade and the amount of sputtered material increases for an arbitrary choice of target and ion beam. $M_{K_{ii}}$ is a decreasing function of K_{ii} for $i = 1$ and 2 as a result. We conclude that both F_1 and F_2 are positive, which means that the curvature dependence of the crater function yields a *smoothing* contribution to the dynamics that is neglected in Eqs. (3.67) and (3.68).

Equations (3.61) and (3.62) give the values of F_1 and F_2 for the Sigmund model. It is a simple matter to verify that F_1 and F_2 are indeed positive using these formulae, in accord with our general

observation. In addition, for the Sigmund model, F_1 is greater than F_2 for all $\theta > 0$. To see this, note that because the collision cascade is elongated along the direction of the incident ion, the lateral straggling length β exceeds the longitudinal straggling length α. Thus, $a_\alpha \equiv a/\alpha < a/\beta \equiv a_\beta$ and $B_1 \equiv a_\alpha^2 \sin^2\theta + a_\beta^2 \cos^2\theta < a_\beta^2$ for $\theta > 0$. The constants A, B_1, B_2 and C are all positive for $\theta > 0$ and $M_x^{(0)} > 0$ as well. Hence

$$F_1 = \frac{aM_x^{(0)}}{B_1}\left(\frac{B_2}{2} + \frac{3AC}{B_1} + \frac{A^2B_2}{2B_1} + \frac{A^3C}{B_1^2}\right) > \frac{aM_x^{(0)}}{a_\beta^2}\left(\frac{B_2}{2} + \frac{AC}{B_1}\right) = F_2. \tag{3.70}$$

For the Sigmund model, therefore, the smoothing effect that comes from the curvature dependence of the crater function is greater for parallel-mode ripples that it is for perpendicular-mode ripples, except of course for the degenerate case of normal-incidence bombardment.

Nietiadi and Urbassek noted that for normal-incidence ion bombardment, the common value of $M_{K_{11}}$ and $M_{K_{22}}$ is a decreasing function of $K_{11} = K_{22}$ for both the Sigmund model and for their simulations of sputtering of amorphous silicon.[165] From these observations, they correctly concluded that the curvature dependence of the crater function produces a smoothing effect. However, Nietiadi and Urbassek then went on to assert that this effect "counteracts the main effect of Bradley-Harper theory, since it leads to increased sputtering on crests and decreased sputtering in troughs." In fact, as we have seen, the curvature dependence of the crater function must be taken into account if the exact BH values of the coefficients C_{11} and C_{22} are to be reproduced by the CFF. The smoothing effect produced by the curvature dependence of the crater function is therefore included in the BH theory.

Perkinson *et al.*[164] have recently pointed out some apparent inconsistencies in the coefficients given by Norris *et al.*, Eqs. (3.67) and (3.68). Because Norris *et al.*'s expression for C_{11} is a

derivative with respect to θ of a function which vanishes at $\theta = 0$ and $\pi/2$, the integral of C_{11} is

$$\int_0^{\pi/2} C_{11}(\theta)d\theta = -M_x^{(1)}(\theta)\cos\theta\Big|_{\theta=0}^{\theta=\pi/2} = 0 \tag{3.71}$$

for their theory. Additionally, using Norris *et al.*'s expressions (3.67) and (3.68), we obtain

$$C_{11}(\theta) = \frac{d}{d\theta}\big(C_{22}\tan\theta\big). \tag{3.72}$$

Perkinson *et al.*'s experiments provide evidence that the actual values for C_{11} and C_{22} do not satisfy either Eq. (3.71) or (3.72). This again suggests that the errors incurred by neglecting the curvature dependence of the crater function are significant. When one includes the curvature dependence, however, Eqs. (3.29) and (3.53) result, and Eqs. (3.71) and (3.72) do not apply. Our CFF therefore does not suffer from the same difficulties as that of Norris *et al.*[132]

Perkinson *et al.*'s experimental results indicate that there is "a surfeit of stability relative to instability compared to the prediction of crater-function theory," i.e., the actual values of C_{11} and C_{22} are larger than the theoretical values obtained using Eqs. (3.67) and (3.68). It seems likely that this discrepancy was the result of omitting the smoothing effect of the curvature dependence of the crater function.

As Eq. (3.27) shows, the crater function for a flat surface is all that is needed to compute C_0. Our expression for C_0 agrees with that of Norris *et al.* as a consequence. Our extended CFF also yields an expression for C_1, Eq. (3.28). Norris *et al.* did not give an explicit formula that relates C_1 to a crater function moment.[132] This coefficient is needed if one wishes to find the velocity with which parallel-mode ripples propagate over the solid surface.

Norris, Brenner and Aziz introduced their CFF in 2009 but did not apply it to estimate the coefficients in the EOM for a particular target material or choice of ion beam.[12] Subsequently, Norris *et al.* carried out MD simulations of the bombardment of a flat silicon surface with 100 and 250 eV Ar^+ ions and then used Eqs. (3.67) and (3.68) to obtain estimates of C_{11} and C_{22}.[132]

The results of Norris *et al.* have some puzzling aspects. For angles of incidence θ below a critical value θ_c, the surface remains flat. For $\theta > \theta_c$, on the other hand, ripples develop as the bombardment proceeds. The experimental value of θ_c Norris *et al.* obtained for 250 eV ions (48°) is approximately 10° larger than the theoretical value they obtained. Moreover, for $\theta = 50°$, the measured ripple wavelength was roughly twice as large as the theoretical value. The difference between the measured and theoretical wavelength declined for larger values of θ, but remained appreciable up until θ had reached 65°. Finally, a switch from parallel-mode ripples to perpendicular-mode ripples was observed for incidence angles near grazing in the experiments of Norris *et al.* but no such transition was found by inputting their MD results into Eqs. (3.67) and (3.68).

Plausible explanations for these discrepancies between theory and experiment emerge if the curvature dependence of the crater function is taken into account. The smoothing effect of the curvature dependence of the crater function clearly increases the theoretical value of θ_c. Moreover, the wavelength of parallel-mode ripples is inversely proportional to $|C_{11}|^{1/2}$, and so when the contribution to C_{11} that comes from the curvature dependence of the crater function is included, the predicted wavelength increases. Finally, recall that for the Sigmund model the curvature dependence of the crater function has a greater smoothing effect on parallel-mode ripples than it does for perpendicular-mode ripples. It seems likely that this is also true for Ar^+ bombardment of silicon, since the Sigmund model provides a good description of the spatial distribution of the deposited energy.[166] It is therefore possible that if the curvature dependence of the crater function had been

taken into account by Norris *et al.* in their theoretical work, then they might have found a transition between parallel- and perpendicular-mode ripples as θ nears 90°.

If the correct formulae (3.29) and (3.53) are to be used in combination with MD simulations to obtain accurate estimates of C_{11} and C_{22}, it is not sufficient to find the crater function for a flat surface. Instead, to find C_{11}, craters on a curved surface of the form $h(x,y) = K_{11}x^2/2$ must be found for a range of small values of K_{11} so that the derivative $\partial M_{K_{11}}/\partial K_{11}$ can be computed for $K_{11} = 0$. Naturally, an analogous statement applies to determining C_{22}. In that case, craters on a surface that has the form $h(x,y) = K_{22}y^2/2$ are needed. This means that the computational resources necessary to find accurate values of the coefficients C_{11} and C_{22} are considerably greater than it was previously thought.

3.7.1 Binary Materials

In 1999, a series of fascinating experiments by Facsko *et al.* revealed that normal-incidence bombardment of the binary compound GaSb with an argon ion beam can produce a densely packed, highly regular hexagonal array of nanodots.[73] Bradley and Shipman (BS) subsequently introduced a theory that accounts for the formation of orderly hexagonal arrays of nanodots when the flat surface of a binary compound is subjected to normal-incidence ion bombardment.[155, 156, 157] In their theory, the coupling between the topography of the surface and a thin surface layer of altered composition is the key to the observed pattern formation. In addition, in the BS theory, the curvature dependence of the sputter yields is responsible for the instability that leads to the formation of the nanodots.

In an effort to test the BS theory, Norris and co-workers extended their CFF to binary materials.[163] They then performed MD simulations to find the craters produced by argon ion bombardment of GaSb and input the results into their CFF. The resulting estimated parameter values do not lead

to the formation of ordered arrays of nanodots in the BS model. These results have led Norris to suggest that the instability that leads to the formation of the nanodot arrays stems from phase segregation rather than the curvature dependence of the sputter yields, and to generalize the BS theory to include the former effect.[167]

Norris *et al.* neglected the curvature dependence of the crater function in extending their CFF to binary target materials.[163] Accordingly, it is possible that the errors in their estimated parameter values are quite large, and that improved estimates would in fact lead to the emergence of ordered arrays of nanodots from the BS model. Additional analytical work is needed in which the curvature dependence of the crater function is taken into account when the CFF is extended to binary materials. MD simulations that yield the crater function for curved GaSb surfaces would then permit significant improvements in the estimated parameter values, and would indicate whether curvature dependent erosion or phase segregation is responsible for the formation of the nanodots.

3.8 Conclusions

In principle, the crater function F depends on the entire shape of the surface in the vicinity of the point of impact. In this chapter, we extended the crater function formalism to include the dependence of F on the curvature of the surface at the point of impact. Explicit expressions for the constant coefficients in the continuum equation of motion were derived; these reduce to the results given by Norris *et al.*[132] *only* if the curvature dependence of the crater function is negligible. Our extended crater function formalism yields the exact coefficients for the Sigmund model of ion sputtering. In contrast, if the curvature dependence of the crater function is neglected, substantial errors in the estimated values of the coefficients typically ensue.

Our results show that accurately estimating the coefficients in the equation of motion using craters obtained from molecular dynamics simulations will require significantly more computational power than was previously thought. They also lead us to question the reliability of the coefficient estimates that have been obtained using the version of the crater function formalism in which the curvature dependence of the crater function is neglected.

CHAPTER 4

AZIMUTHAL ROTATION OF BINARY TARGETS

4.1 Introduction

It has recently become apparent that ion bombardment of binary materials is able to produce a much richer variety of patterns than bombardment of elemental materials can. Examples of patterns that can form include nearly defect-free surface ripples,[158] hexagonal and square arrays of nanodots,[73,77,155,156] and a hybrid "dots-on-ripples" topography in which dots that form a hexagonal array sit atop a ripple pattern.[159] The key to understanding the emergence of these novel patterns is the observation that the surface composition and topography are coupled.[158,155,156,159,124] This coupling also plays an important role in "surfactant sputtering," i.e., pattern formation on an initially elemental material that is subjected to ion bombardment and concurrent deposition of a second atomic species.[168,169,125,153,170]

The formation of surface ripples is problematic in a variety of applications, including secondary ion mass spectroscopy (SIMS), Auger electron spectroscopy (AES), and ion milling. SIMS is one of the most widely used techniques for dopant profiling of semiconductors, while AES is an important tool in the structural characterization of multilayers. In the simplest kind of SIMS or AES apparatus, the primary ions are obliquely incident on the stationary surface of the sample. Thus, as sputtering proceeds, ripples can be formed, and this leads to rapid degradation of the depth resolution.

Zalar first demonstrated that this problem can often be overcome by rotating the sample with a constant angular velocity about its surface normal as the depth profiling proceeds.[171] Zalar rotation has subsequently been used by many other groups, who found that in many cases, the surface actually becomes flatter as the solid is eroded.[16] Consequently, ion sputtering with concurrent sample rotation has also been used as a means of preparing ultra-smooth surfaces for optical applications.[19] Sample rotation does not always prevent surface roughening, however. In some instances, the sample roughens while it is simultaneously eroded and rotated, albeit at a slower rate than it does when it is stationary.[16,17]

Some understanding of the effects of sample rotation during ion bombardment of an elemental material has been achieved. In the early time linear regime,[172] the rate with which the surface roughens or smooths is independent of the angular velocity ω so long as ω is nonzero. The same is true of the characteristic length scale of the patterns that form. In the longer time nonlinear regime, if the surface is unstable, it is governed by the Kuramoto-Sivashinsky equation in the limit that ω is large.[173] The surface roughness asymptotes to a finite steady-state value in that event.

In recent years it has been discovered that mass redistribution plays an important role in nanoscale pattern formation on ion-bombarded Si and Ge targets, and it has been speculated that this may true of other elemental materials as well.[46,132,47] Mass redistribution was not taken into account in Refs. [172] and [173], but incorporating this phenomenon into the theory does not alter the predictions mentioned in the preceding paragraph.

Kinetic Monte Carlo simulations of the ion bombardment of elemental materials indicate that the surface roughness depends on ω in the nonlinear regime if the sample rotation is not rapid.[174] This has since been confirmed experimentally,[175] even though the effect of mass redistribution was not included these simulations. Very recently, kinetic Monte Carlo simulations which utilize crater func-

tions computed using molecular dynamics have been performed.[176] Mass redistribution was taken into account in these simulations, although the curvature dependence of the craters[165,177,178,179] was not. The results of these simulations suggest that the patterns formed in the nonlinear regime strongly depend on the angular velocity ω.

It is now known that sample rotation during oblique-incidence ion sputtering of *binary* materials can produce intriguing surface patterns that would not otherwise appear. In particular, hexagonal, square and rectangular arrays of nanodots have been observed in experiments.[74,180] If the rotation is sufficiently rapid, the equations of motion have the same form as for normal-incidence bombardment but the values of the coefficients are altered.[156] The Bradley-Shipman theory therefore predicts that hexagonal arrays of nanodots will form for a range of parameter values,[155,156] in accord with the experiments of Frost and co-workers.[74,180] It is not currently understood how square and rectangular arrays arise, however.

The object of the present chapter is to explore the effects of sample rotation with a finite angular velocity ω during ion sputtering of binary materials. We will also consider surfactant sputtering of a rotating sample. These are challenging problems which we will simplify by restricting our attention to times early enough that linear equations of motion apply. We will also concentrate on the case in which the sample is periodically rotated in discrete steps of 180°. As we shall see, this problem is quite rich but it can nonetheless be solved analytically. We find that the rate with which the surface roughens or smooths depends on the frequency of rotation ω, in contrast to the behavior of elemental materials in the linear regime. In addition, the characteristic length scale of the patterns that form changes as the value of ω is increased, and can even exhibit a jump discontinuity. Our numerical work shows that this unexpected behavior carries over to the case in which the sample is rotated continuously rather than discretely.

The chapter is organized as follows. In Section 4.2, we introduce the equations of motion that describe the coupled dynamics of the surface composition and morphology for a stationary sample and show how they can be solved. The general solution of the equations of motion for a sample rotating periodically in discrete steps of 180° is obtained in Section 4.3. We apply these results to a simplified model of surfactant sputtering in Section 4.4 to illustrate the types of behavior that can occur as a result of sample rotation during concurrent ion bombardment and impurity deposition. In Section 4.5, we study the case of continuous sample rotation with a constant angular velocity and show that the interesting features of our solution for discrete rotation are also found in this case. We discuss our results further in Section 4.6. We place our results in a mathematical context in Section 4.7. Finally, we summarize this chapter in Section 4.8.

4.2 Stationary Samples

The theory developed in this chapter is applicable to two types of experiments which are physically different yet which yield similar equations of motion. In particular, it applies to

I. a binary material that is bombarded with a broad ion beam with the angle of incidence θ, and to

II. an initially elemental material being bombarded by a broad ion beam with incidence angle θ while undergoing concurrent deposition of a second atomic species at an angle θ_d with respect to the vertical.

J will denote the ion flux in both Problems I and II. In Problem II, we require the atomic beam to have the same azimuth as the ion beam, and the atomic flux will be denoted by J_d.

In order to make the analysis of rotating samples as clear as possible, we will first review how to evaluate the linear stability of a solid surface for the non-rotating case. We define the x direction to be the projection of the ion beam onto the plane of the surface, the z direction to be normal to that plane, and the y direction to be orthogonal to both the x and z directions so as to follow the right-hand convention. We define

$$u(\boldsymbol{x},t) = h(\boldsymbol{x},t) + V_0 t, \tag{4.1}$$

where $h(\boldsymbol{x},t)$ is the height of the surface above a point $\boldsymbol{x} = (x,y)$ in the $x-y$ plane at time t and V_0 is the steady-state erosion velocity of a flat surface. In the case of Problem I, we will call the elements that make up the binary material A and B and take A to be the species with the lower of the two sputter yields. For Problem II, on the other hand, the atoms that make up the elemental material will be species B and the atomic species that is concurrently deposited will be species A. In both cases, we let $\phi(\boldsymbol{x},t)$ denote the deviation of the surface concentration of A atoms from its steady-state value above the point $\boldsymbol{x}$ at time t. It will be assumed that the sample is amorphous or that a surface layer of the sample is amorphorized by the ion bombardment. We will also assume that the solid surface is close to being flat and that the deviations of the surface composition from its uniform steady-state value are small. These last two assumptions allow us to use linearized equations of motion.

The linearized equations of motion for Problem I take the form

$$\begin{aligned} u_t &= a_{10}u_x + a_{20}u_{xx} + a_{02}u_{yy} + \ldots \\ &\quad + b_{00}\phi + b_{10}\phi_x + b_{20}\phi_{xx} + b_{02}\phi_{yy} + \ldots \end{aligned} \tag{4.2}$$

$$\begin{aligned} \phi_t &= c_{10}u_x + c_{20}u_{xx} + c_{02}u_{yy} + \ldots \\ &\quad + d_{00}\phi + d_{10}\phi_x + d_{20}\phi_{xx} + d_{02}\phi_{yy} + \ldots, \end{aligned} \tag{4.3}$$

where the subscripts on u and ϕ denote partial derivatives.[158, 155, 156, 159, 157] The a_{ij}'s, b_{ij}'s, c_{ij}'s, and d_{ij}'s are real constant coefficients which in general depend on the sample material, the sample temperature, and the characteristics of the ion beam. Explicit expressions which relate these coefficients to the underlying physical parameters may be found in Refs. [158, 155, 156, 159, 157].

The terms proportional to u_x in Eqs. (4.2) and (4.3) describe the dependence of the sputter yields on the angle of incidence, while those proportional to ϕ stem from the dependence of the yields on the surface composition. Both curvature-dependent sputtering[13] and mass redistribution[132, 41] contribute to the terms proportional to u_{xx} and u_{yy}. Mass redistribution also gives rise to the terms proportional to ϕ_x. Finally, the terms proportional to ϕ_{xx} and ϕ_{yy} are the result of surface diffusion.

Notice that some terms cannot appear in Eqs. (4.2) and (4.3) due to the symmetries of the system. In particular, the transformed surface height u cannot appear undifferentiated due to translational invariance in the z direction, and all terms must be invariant under the transformation $y \to -y$ due to the reflectional symmetry of the system about the $x-z$ plane.

Equations (4.2) and (4.3) are also the equations of motion for Problem II.[125, 153, 170, 157] In this case, however, the coefficients in the equations of motion also depend on the atomic species that

is being deposited and on the values of J_d and θ_d. The dynamics of the surface morphology and composition are in general coupled in both Problems I and II.

We may simplify Eqs. (4.2) and (4.3) by considering the equation of motion for a single Fourier mode with wavevector $\boldsymbol{k}$. We set

$$\begin{pmatrix} u(\boldsymbol{x},t) \\ \phi(\boldsymbol{x},t) \end{pmatrix} = \begin{pmatrix} \tilde{u}(t) \\ \tilde{\phi}(t) \end{pmatrix} \exp(i\boldsymbol{k}\cdot\boldsymbol{x}) \equiv \tilde{\boldsymbol{X}}(t)\exp(i\boldsymbol{k}\cdot\boldsymbol{x}), \tag{4.4}$$

which gives rise to the matrix equation

$$\frac{d}{dt}\tilde{\boldsymbol{X}}(t) = \hat{A}\tilde{\boldsymbol{X}}(t). \tag{4.5}$$

The 2×2 matrix $\hat{A} = \hat{A}(\boldsymbol{k})$ is given by

$$\hat{A} \equiv \begin{pmatrix} a & b \\ c & d \end{pmatrix}, \tag{4.6}$$

where

$$a \equiv a_{10} ik_x - a_{20}k_x^2 - a_{02}k_y^2 + \ldots \tag{4.7}$$

$$b \equiv b_{00} + b_{10} ik_x - b_{20}k_x^2 - b_{02}k_y^2 + \ldots \tag{4.8}$$

$$c \equiv c_{10} ik_x - c_{20}k_x^2 - c_{20}k_y^2 + \ldots \tag{4.9}$$

$$d \equiv d_{00} + d_{10} ik_x - d_{20}k_x^2 - d_{02}k_y^2 + \ldots \tag{4.10}$$

. (4.11)

The solution to Eq. (4.5) is

$$\tilde{\boldsymbol{X}}(t) = \exp(\hat{A}t)\boldsymbol{e}, \tag{4.12}$$

where $\boldsymbol{e} = \boldsymbol{e}(\boldsymbol{k})$ is a constant vector that is determined by the initial conditions. Clearly, if $\hat{A}(\boldsymbol{k})$ has an eigenvalue whose real part is positive, the surface is unstable with respect to perturbations of wavevector $\boldsymbol{k}$. If it does not, the surface is either neutrally stable or stable with respect to such a perturbation. It is sufficient to determine the stability of perturbations with height and composition that vary sinusoidally in space because an arbitrary surface disturbance can be written as a linear combination of this type of mode.

As a concrete example of the use of our formalism, we will later consider a particular version of Problem II in some detail. In this version of Problem II, a number of simplifying assumptions are made.[153] In particular, it is assumed that curvature dependent sputtering and mass redistribution can be neglected. The sample temperature is also taken to be low enough that thermally activated surface diffusion is negligible, but radiation-induced viscous flow near the surface of the solid[127] is taken into account. Finally, it is assumed that no chemical reactions between the target atoms and the impurities take place.

The rescaled equations of motion for this problem are

$$u_t = \phi + v u_x - \tilde{D}\nabla^4 u \tag{4.13}$$

$$\phi_t = -\phi + u_x - \tilde{D}'\nabla^4 u. \tag{4.14}$$

As shown in Ref. [153], the terms proportional to ϕ on the right-hand side of Eqs. (4.13) and (4.14) arise because the sputtered fluxes of the two atomic species depend on the surface composition. The terms proportional to u_x, on the other hand, stem from the angular dependence of the sputter yields and the atomic flux being deposited on the surface. Finally, radiation-induced viscous flow is the origin of the terms proportional to $\nabla^4 u$.

The general expression for the parameter v (which is given in Ref. [153]) is quite complex. However, if the ion beam is normally incident on the solid surface, then v is just $Y_A/(Y_B - Y_A)$, where Y_A is the sputter yield of species A for normal-incidence bombardment and Y_B is defined analogously.

The solid surface is stable for $v < -1$.[153] For $v > -1$, on the other hand, the surface is unstable and ripples develop. The instability criterion $v > -1$ reduces to the requirement that Y_B be greater than Y_A for normal-incidence ion bombardment and oblique-incidence deposition of the atomic species A. Physically, the instability is a result of the coupling between the surface composition and topography. This coupling arises because the flux of A atoms onto the surface depends on the surface slope and because the erosion rate depends on the surface composition.

Equations (4.13) and (4.14) are a special case of Eqs. (4.2) and (4.3). In this case, the matrix $\hat{A}$ is given by

$$\hat{A} = \begin{pmatrix} ivk_x - \tilde{D}k^4 & 1 \\ ik_x - \tilde{D}'k^4 & -1 \end{pmatrix} \equiv \hat{A}_0. \tag{4.15}$$

This is the matrix $\hat{A}$ for the example that we will analyze in detail later.

4.3 Samples Rotating in Discrete Steps

Consider the surface of a binary material which is being bombarded with an ion beam while undergoing periodic discrete rotations of 180° about the z-axis. We will choose a frame of reference that rotates with the sample. In that frame, the incidence angle of the ion beam switches back and forth between the values θ and $-\theta$ for a total time T. After each rapid switch, the angle of incidence remains fixed for a dwell time Δt before it switches once more. Our goal is to analyze the linear stability of the surface for all possible values of Δt. As mentioned previously, our analysis is

equally applicable to the bombardment of an initially elemental material with concurrent deposition of a second atomic species.

The equations of motion that apply after the beam switches direction are obtained from Eqs. (4.2) and (4.3) simply by replacing x by $-x$ everywhere that it appears. In Fourier space, this is equivalent to replacing ik_x by its complex conjugate $-ik_x$. Notice that only even powers of ik_y appear in the matrix $\hat{A}$ and that these factors are not affected by complex conjugation. The equation of motion for $\tilde{\boldsymbol{X}}$ that applies after the beam switches direction is therefore

$$\frac{d}{dt}\tilde{\boldsymbol{X}}(t) = \hat{A}^{*}\tilde{\boldsymbol{X}}(t), \tag{4.16}$$

where $\hat{A}^{*}$ denotes the complex conjugate of the matrix $\hat{A}$.

Clearly, whenever the angle of incidence is θ, Eq. (4.5) holds. Conversely, Eq. (4.16) is valid when the angle of incidence is $-\theta$.

We may now write down the solution to the problem in which the incidence angle of the ion beam periodically switches back and forth between θ and $-\theta$ with a dwell time of Δt in each orientation. If the total time T is $2n\Delta t$ where n is an integer, then

$$\tilde{\boldsymbol{X}}(T) = \left[\exp(\hat{A}^{*}\Delta t)\exp(\hat{A}\Delta t)\right]^{n}\boldsymbol{e}. \tag{4.17}$$

For notational convenience, we define

$$\hat{L} \equiv \exp(\hat{A}^{*}\Delta t)\exp(\hat{A}\Delta t). \tag{4.18}$$

Equation (4.17) then assumes the succinct form

$$\tilde{\boldsymbol{X}}(2n\Delta t) = \hat{L}^n \boldsymbol{e}. \tag{4.19}$$

More generally, if $2n\Delta t \leq T \leq (2n+1)\Delta t$ for some integer n, then

$$\tilde{\boldsymbol{X}}(T) = \exp\left(\hat{A}(T - 2n\Delta t)\right)\hat{L}^n \boldsymbol{e} \tag{4.20}$$

and for $(2n+1)\Delta t \leq T \leq (2n+2)\Delta t$,

$$\tilde{\boldsymbol{X}}(T) = \exp\left(\hat{A}^*[T - (2n+1)\Delta t]\right)\exp\left(\hat{A}\Delta t\right)\hat{L}^n \boldsymbol{e}. \tag{4.21}$$

Let λ_+ and λ_- denote the eigenvalues of $\hat{L}$, where $|\lambda_+| \geq |\lambda_-|$. In addition, let $\boldsymbol{v}_+$ and $\boldsymbol{v}_+$ be the associated eigenvectors. These vectors form a basis if λ_+ and λ_- are distinct. In that case, $\boldsymbol{e} = e_+\boldsymbol{v}_+ + e_-\boldsymbol{v}_+$, where e_+ and e_- are complex constants. Equation (4.19) then shows that

$$\tilde{\boldsymbol{X}}(2n\Delta t) \cong e_+\lambda_+^n \boldsymbol{v}_+ \tag{4.22}$$

for large n. Thus, $|\tilde{\boldsymbol{X}}(2n\Delta t)|$ grows exponentially with n if and only if $|\lambda_+| > 1$. More generally, the mode's amplitude $|\tilde{\boldsymbol{X}}(T)|$ grows exponentially with the time T if and only if $|\lambda_+| > 1$, although oscillations of period $2\Delta t$ are superimposed on this overall exponential increase. The growth rate of the mode's amplitude is $R \equiv \ln(|\lambda_+|)/(2\Delta t)$.

The analysis just given shows that surface disturbances of wavevector $\boldsymbol{k}$ are unstable if and only $\hat{L} = \hat{L}(\boldsymbol{k})$ has an eigenvalue whose magnitude is greater than 1. Thus, our next task will be to find the eigenvalues of $\hat{L}$. This is a nontrivial undertaking because the matrix $\hat{A}$ is not diagonal except if

the surface composition and morphology are completely decoupled. Moreover $\hat{A}$ and $\hat{L}$ are not in general Hermitian.

We define

$$\gamma \equiv \frac{\mathrm{tr}(\hat{A})}{2} \tag{4.23}$$

and

$$D \equiv \gamma^2 - \det(\hat{A}), \tag{4.24}$$

so that the eigenvalues σ_+ and σ_- of the matrix $\hat{A}$ may be written

$$\sigma_\pm = \gamma \pm \sqrt{D}. \tag{4.25}$$

The associated eigenvectors are

$$\boldsymbol{z}_\pm = \begin{pmatrix} F_\pm \\ 1 \end{pmatrix} \tag{4.26}$$

where

$$F_\pm \equiv \frac{\sigma_\pm - d}{c}. \tag{4.27}$$

It will be helpful to place $\boldsymbol{z}_+$ and $\boldsymbol{z}_-$ in the columns of a 2×2 matrix: we set

$$\hat{U} \equiv (\boldsymbol{z}_+, \boldsymbol{z}_-) = \begin{pmatrix} F_+ & F_- \\ 1 & 1 \end{pmatrix}. \tag{4.28}$$

We shall now use $\hat{U}$ to diagonalize the matrix exponentials in $\hat{L}$. This will enable us to compute the eigenvalues of $\hat{L}$. Due to the complexity of the final expression for these eigenvalues, it is preferable to express λ_+ and λ_- in terms of the trace and determinant of $\hat{L}$, which take on somewhat simpler forms. Having found the trace and determinant, we will obtain the eigenvalues from the

simple identity

$$\lambda_{\pm} = \tau/2 \pm \sqrt{\tau^2/4 - \det(\hat{L})}, \tag{4.29}$$

where

$$\tau \equiv \mathrm{tr}(\hat{L}). \tag{4.30}$$

In fact, it is easy to show that the determinant is given by

$$\det(\hat{L}) = |\det(\exp(\hat{A}\Delta t))|^2 = |\exp(2(\sigma_+ + \sigma_-)\Delta t)| = \exp(4\mathrm{Re}\,(\gamma)\Delta t). \tag{4.31}$$

The primary difficulty therefore arises in evaluating the trace of $\hat{L}$.

The matrix $\hat{U}$ is composed of the eigenvectors of $\hat{A}$. As long as the eigenvalues of $\hat{A}$ are distinct, then $\hat{U}^{-1}$ exists and is given by

$$\hat{U}^{-1} = \frac{c}{2\sqrt{D}} \begin{pmatrix} 1 & -F_- \\ -1 & F_+ \end{pmatrix}. \tag{4.32}$$

Let

$$G_{\pm} \equiv e^{\sigma_{\pm}\Delta t}, \tag{4.33}$$

$$G_{\gamma} \equiv e^{\gamma\Delta t}, \tag{4.34}$$

and

$$G_D \equiv e^{\sqrt{D}\Delta t}. \tag{4.35}$$

Noting that

$$\hat{U}^{-1}\hat{A}\hat{U} = \begin{pmatrix} \sigma_+ & 0 \\ 0 & \sigma_- \end{pmatrix}, \tag{4.36}$$

and therefore that

$$\exp(\hat{U}^{-1}\hat{A}\Delta t\hat{U}) = \begin{pmatrix} G_+ & 0 \\ 0 & G_- \end{pmatrix}, \tag{4.37}$$

we may write

$$\begin{aligned} \hat{L} &= \hat{U}^* \exp((\hat{U}^*)^{-1}\hat{A}^*\Delta t\hat{U}^*)(\hat{U}^*)^{-1}\hat{U}\exp(\hat{U}^{-1}\hat{A}\Delta t\hat{U})\hat{U}^{-1} \\ &= \hat{U}^* \begin{pmatrix} G_+^* & 0 \\ 0 & G_-^* \end{pmatrix} \hat{U}^{*-1}\hat{U} \begin{pmatrix} G_+ & 0 \\ 0 & G_- \end{pmatrix} \hat{U}^{-1}. \end{aligned} \tag{4.38}$$

Through explicit matrix multiplication, the trace of $\hat{L}$ is found to be

$$\begin{aligned} \tau &= \frac{|c|^2}{4|D|}\Big[|F_+G_+ - F_-G_-|^2 + |F_+G_- - F_-G_+|^2 - 2|G_+ - G_-|^2\mathrm{Re}\,(F_+F_-)\Big] \\ &= 2|G_\gamma|^2\Big[\frac{|\gamma - d|^2}{|D|}|\sinh(\sqrt{D}\Delta t)|^2 \\ &\quad + |\cosh(\sqrt{D}\Delta t)|^2 + |\sinh(\sqrt{D}\Delta t)|^2\frac{\mathrm{Re}\,(bc^*)}{|D|}\Big], \end{aligned} \tag{4.39}$$

where we have used the identities

$$|x_1 + x_2|^2 + |x_1 - x_2|^2 = 2(|x_1|^2 + |x_2|^2) \tag{4.40}$$

valid for arbitrary complex x_1 and x_2 and

$$|c|^2\mathrm{Re}\,(F_+F_-) = -\mathrm{Re}\,(bc^*). \tag{4.41}$$

We now break up the arguments of the hyperbolic trigonometric functions in Eq. (4.39) into their real and imaginary parts using the identities

$$|\cosh(x_1+ix_2)|^2=\frac{1}{2}[\cosh(2x_1)+\cos(2x_2)] \tag{4.42}$$

and

$$|\sinh(x_1+ix_2)|^2=\frac{1}{2}[\cosh(2x_1)-\cos(2x_2)] \tag{4.43}$$

that are valid for arbitrary real x_1 and x_2. Setting

$$z=\frac{\cos(2\Delta t\,\mathrm{Im}\,(\sqrt{D}))}{\cosh(2\Delta t\,\mathrm{Re}\,(\sqrt{D}))} \tag{4.44}$$

and

$$\Gamma=|D|^{-1}\Big[\frac{|a-d|^2}{4}+\mathrm{Re}\,(bc^*)\Big], \tag{4.45}$$

we finally arrive at a convenient expression for the trace of $\hat{L}$:

$$\tau=\frac{1}{2}\Big[\exp(2\mathrm{Re}\,(\sigma_+)\Delta t)+\exp(2\mathrm{Re}\,(\sigma_-)\Delta t)\Big]\,[1+z+(1-z)\Gamma]\,. \tag{4.46}$$

This may also be written

$$\tau=\exp(\mathrm{Re}\,(2\Delta t\gamma))\Big[\cosh(\mathrm{Re}\,(2\Delta t\sqrt{D}))(1+\Gamma)+\cos(\mathrm{Im}\,(2\Delta t\sqrt{D}))(1-\Gamma)\Big]. \tag{4.47}$$

The eigenvalues of L are obtained by inserting Eqs. (4.31) and (4.46) into Eq. (4.29). Equations (4.29), (4.31) and (4.46) may therefore be used to evaluate the stability of the surface, and are analyzed in greater detail in the following sections.

Notice that nowhere in this derivation have we used specific expressions for the constant coefficients that appear in the equations of motion (4.2) and (4.3). Our formalism therefore allows us to determine whether the initially flat surface with uniform surface composition is stable or unstable for an arbitrary problem of type I or II. Moreover, if the surface is unstable, our results can be used to find the selected wavevector and the growth rate of the associated mode. We have therefore obtained a very general result which may be used to analyze a wide variety of problems in which the sample is periodically rotated in discrete steps of 180°.

The limiting case in which Δt tends to zero is quite simple. If Δt is small, then to first order in Δt

$$\hat{L} = (\mathbb{I} + \hat{A}^* \Delta t)(\mathbb{I} + \hat{A}\Delta t) = \mathbb{I} + 2\mathrm{Re}\,(\hat{A})\Delta t = \exp(2\mathrm{Re}\,(\hat{A})\Delta t), \tag{4.48}$$

where $\mathbb{I}$ is the 2×2 identity matrix. Let ρ_+ and ρ_- be the eigenvalues of $\mathrm{Re}\,(\hat{A})$, where $\rho_+ \geq \rho_-$. Equation (4.48) shows that the growth rate $R = \ln(|\lambda_+|)/(2\Delta t)$ reduces to ρ_+ in the $\Delta t \to 0$ limit.

In the limit that Δt tends to zero, we expect the behavior of the surface in Problem I to be the same as if the sample were stationary and there were two diametrically opposed ion beams with incidence angles $\pm\theta$ that each have flux $J/2$. To confirm this expectation, we note that for the problem with diametrically opposed beams, the coefficients of all of the terms with odd powers of ∂_x vanish in Eqs. (4.2) and (4.3). Equation (4.5) is therefore replaced by

$$\frac{d}{dt}\tilde{\boldsymbol{X}}(t) = \mathrm{Re}\,(\hat{A})\tilde{\boldsymbol{X}}(t), \tag{4.49}$$

which shows that $\mathrm{Re}\,(\hat{A})$ plays the role of $\hat{A}$ in the dual-beam problem. We conclude that the growth rate R is ρ_+ in the dual beam problem, which is precisely the growth rate we found for the single beam problem with discrete rotation in steps of 180° in the $\Delta t \to 0$ limit.

We can proceed in a similar fashion to obtain an analogous conclusion for Problem II in the limit that the dwell time Δt tends to zero. In that limit, the surface behaves as if there were two diametrically opposed ions beams with flux $J/2$ and incidence angles $\pm\theta$ *and* two diametrically opposed atomic beams with flux $J_d/2$ and incidence angles $\pm\theta_d$.

It is instructive to compare the result given by Eqs. (4.29), (4.31) and (4.46) with the solution of a related but much simpler problem. Suppose that an elemental material is bombarded with an broad ion beam at oblique incidence, and there is no co-deposition of a second atomic species. The linearized equation of motion[13,41,117] takes the form

$$u_t = a_{10}u_x + a_{20}u_{xx} + a_{02}u_{yy} - B\nabla^2\nabla^2 u. \tag{4.50}$$

If the sample is periodically rotated in discrete steps of 180° with a dwell time of Δt, the growth rate of the amplitude of the mode with wavevector $\boldsymbol{k}$ is simply $-a_{20}k_x^2 - a_{02}k_y^2 - Bk^4$. This is precisely the same growth rate we would have if the sample were not rotated at all. Therefore, if the surface is unstable, the discrete rotation does not alter the selected wavelength or its growth rate. The only effect that the sample rotation has is that when the ripple is viewed in the co-rotating frame of reference, it translates back and forth as its amplitude grows or decays.

Our result for the growth rate for Problems I and II with periodic discrete rotations of 180° is much more complex and has an intriguing feature. D depends on the wavevector $\boldsymbol{k}$ but not on the dwell time Δt. If the real part of $\sqrt{D}$ is small compared to its imaginary part for a particular value of $\boldsymbol{k}$, the value of τ will oscillate as Δt is increased from zero [see Eq. (4.47)]. This in turn leads to oscillations of the growth rate $R = \ln(|\lambda_+|)/(2\Delta t)$ as Δt is varied. These oscillations have no analog

in the simple problem we discussed in the preceding paragraph — indeed, for that problem, the growth rate does not depend on Δt at all.

In Section 4.7, we will place the solution obtained in this section in mathematical context. Floquet theory applies to systems of ordinary differential equations with coefficients that vary periodically in time.[181] We will demonstrate that our solution can be written in the canonical Floquet form in the Section 4.7.

4.4 An Example

In this section, we will explore the implications of the solution we found in the previous section by considering a special case. In particular, we will study the simplified version of Problem II in which the equations of motion are given by Eqs. (4.13) and (4.14). The matrix $\hat{A}$ for this problem ($\hat{A}_0$) appears in Eq. (4.15).

Recall that the ripple amplitude grows with time for $|\lambda_+| > 1$ and that it decays for $|\lambda_+| < 1$. The dependence of $|\lambda_+| - 1$ on the dwell time Δt is shown in Fig. 1 for two values of the parameter v and for a particular choice of the wavevector $\boldsymbol{k}$ and the parameter $\tilde{D}$. In contrast to the behavior for an elemental material, $|\lambda_+|$ does depend on the value of Δt. Moreover, as Δt is increased from zero, there is a switch from stability to instability for both values of v. For the case in which v is close to the critical value -1, there is a narrow interval in which the ripple is again stable as Δt is increased further. This behavior is a result of the weak oscillations superimposed on the overall increasing trend in $|\lambda_+|$ for Δt greater than about 0.2.

In the linear theory, the experimentally observed wavevector $\boldsymbol{k}_{\max}$ is the wavevector with the highest growth rate. We have just seen that the growth rate of a sinusoidal surface disturbance

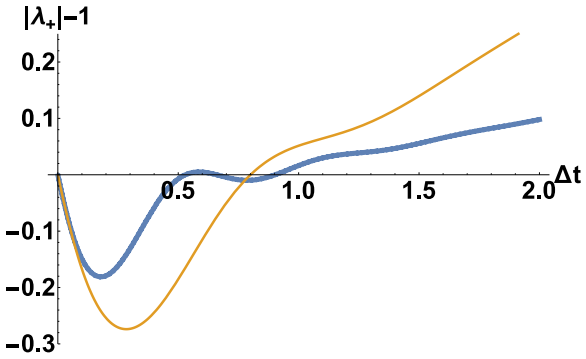

Fig. 4.1 A plot of $|\lambda_+| - 1$ vs Δt for $v = -0.923$ (blue curve) and $v = 0.5$ (orange curve). For both curves, $k_x = 11.46$, $k_y = 0$, $\tilde{D} = 10^{-4}$ and $\tilde{D}' = 0$. Points where the curves are greater than zero correspond to locations in parameter space which produce a surface instability.

depends on the dwell time Δt. It follows that the experimentally observed ripple wavevector depends on Δt as well.

In our example, the mode with the fastest growth rate has its wavevector along the x-direction. The value of the selected wavenumber $k_{\max}$ is plotted as a function of the rotational frequency $\omega \equiv 2\pi/t_0 = \pi/\Delta t$ in Fig. 2 for a particular choice of the parameters v and $\tilde{D}$. This plot shows that the observed wavenumber $k_{\max}$ indeed depends upon ω or, equivalently, on Δt. From a practical standpoint, this means that the ripple wavelength can be tuned by adjusting the value of the rotational frequency.

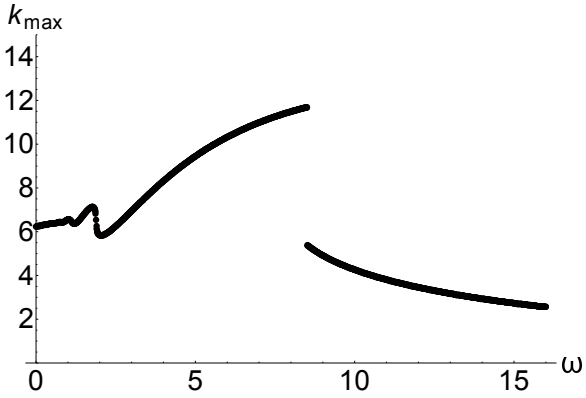

Fig. 4.2 A plot of the selected wavenumber $k_{\max}$ vs. ω for the parameters $\tilde{D} = 10^{-4}$, $\tilde{D}' = 0$ and $v = -0.8$. Notice that by a suitable choice of ω the wavelength of the resulting pattern can be tuned through a wide range of values.

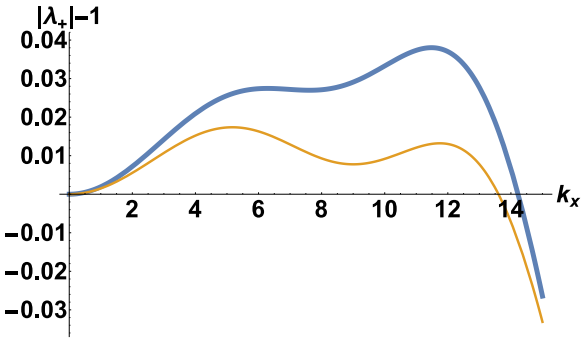

Fig. 4.3 A plot of $|\lambda_+| - 1$ vs. k_x for the parameters $\tilde{D} = 10^{-4}$, $\tilde{D}' = 0$ and $v = -0.8$ for $\omega = 8.0$ (blue curve) and $\omega = 8.7$ (orange curve). We can see the origin of the discontinuous jump in the selected value of k_x.

Figure 4.2 also demonstrates that k_{max} is not a monotone function of ω, and that it may even exhibit a jump discontinuity as ω is varied. The latter behavior is quite unexpected — at first blush, one would anticipate that a small change in the rotational frequency would always result in a small change in the selected wavenumber, but this is not so.

One can understand the origin of such discontinuous jumps by considering how $|\lambda_+| - 1$ depends on k_x — see Fig. 4.3. For $\omega = 8.0$, the global maximum is at approximately $k_x = 12$ and a local maximum is present near $k_x = 5$. As ω is increased, higher k_x values are suppressed to a greater extent than lower ones, and the result is that the local maximum at $k_x \cong 5$ becomes the global maximum. Thus, even though the dispersion relation is continuous, we can obtain discontinuous jumps in the wavenumber of the resulting pattern through a continuous change in the rotation frequency.

If the sample is stationary,[153] the growth rate of a long wavelength mode with wavevector $\boldsymbol{k}$ is

$$R = (v+1)k_x^2. \tag{4.51}$$

This result — which is valid to second order in k_x and k_y — shows that there is an instability for small k_x and k_y if and only if $v > -1$.

How does Eq. (4.51) change if the sample is rotated periodically in discrete steps of 180°? We find that to second order in k_x and k_y

$$\lambda_+ = 1 + (v+1)[1 + \coth(\Delta t)]H(\Delta t)k_x^2, \tag{4.52}$$

where

$$H(\Delta t) \equiv \Delta t[1 - \exp(-2\Delta t)] - 2[1 - \exp(-\Delta t)]^2. \tag{4.53}$$

The function $H(\Delta t)$ is positive for all $\Delta t > 0$. As a consequence, there is an instability for small k_x and k_y if and only if $v > -1$, just as in the case in which the sample is stationary. However, the rotation does reduce the growth rate if $v > -1$. To see this, note that to second order in k_x and k_y,

$$R = (v+1)[1 + \coth(\Delta t)]\frac{H(\Delta t)}{2\Delta t}k_x^2. \tag{4.54}$$

This is less than the growth rate in the absence of discrete rotation because $H(\Delta t)[1 + \coth(\Delta t)] < 2\Delta t$ for all $\Delta t > 0$.

In the small Δt limit, $H(\Delta t) = (\Delta t)^4/6 + O((\Delta t)^5)$ and Eq. (4.54) becomes

$$R \cong \frac{1}{12}(v+1)(\Delta t)^2 k_x^2 \tag{4.55}$$

The growth rate R is therefore small when $\Delta t \ll 1$. We conclude that although the sample rotation does not entirely suppress the long-wavelength instability for $v > -1$, it does drastically reduce the growth rate of the Fourier modes with small wavenumbers if the frequency of sample rotation is

high. In the opposite limit in which $\Delta t \to \infty$, the ratio $H(\Delta t)/\Delta t$ tends to unity and R reduces to its value for a stationary sample, as it must.

It is possible to gain physical insight into some of the results obtained in this section. For simplicity, we will consider the case in which the ion beam is normally incident upon the sample surface. We assume that $Y_B > Y_A$ and that θ_d is nonzero, so that there is an instability.[153] If the sample is stationary, the surface ripple propagates toward the source of A atoms as its amplitude grows. The surface composition is spatially modulated with the same period as the oscillation in the surface height. However, the concentration of A atoms is highest on the surface slopes that face the source of the A atoms, and so these oscillations are not in phase.

Now suppose that the sample is rotated in discrete steps of 180°. We will discuss what happens from the perspective of the frame of reference that moves with the sample. Just after the direction of the atomic beam is switched, the highest concentration of A atoms is on the slopes that face away from the incident beam of A atoms, i.e., the regions of highest concentration are on the "wrong" side of the ripples. In this situation, the rate of growth of the amplitude of the surface ripple declines. However, while this is occurring, the concentration of A atoms on the surface slopes that face the beam of A atoms increases. The concentration on the opposite side of the ripple crests, on the other hand, declines as sputtering continues. Once the concentration of A atoms on the slopes that face the atomic beam has risen sufficiently, the amplitude of the surface ripples begins to climb more rapidly. Thus, each time the beam direction switches, there is a period in which the surface concentration adjusts to the new beam direction and the growth rate of the ripple amplitude is reduced (see Fig. 4.4).

This discussion clearly shows that the growth rate of the ripple amplitude R depends on the rotation frequency ω. It is also apparent that R must be smaller when there are repeated discrete

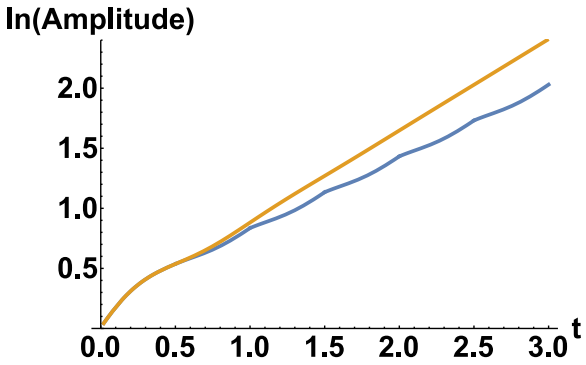

Fig. 4.4 The natural logarithm of the ripple amplitude vs time for the case in which $\Delta t = 0.5$ (blue curve) and for the case in which the sample is stationary (orange curve). The parameter values are $v = 1.0$, $\tilde{D} = 10^{-4}$ and $\tilde{D}' = 0$ for both cases.

rotations in 180° increments than when the sample is stationary. Both of these observations are in accord with the results of our analytical work.

4.5 Samples Rotating with Constant Angular Velocity

Are the intriguing results obtained in Section 4.4 special features of the problem with periodic discrete 180° rotations? To address this question, we will now consider the case in which the sample is rotated continuously with constant angular velocity ω. To begin, we will provide a brief description of how the equation of motion for a continuously rotated sample can be derived. This derivation closely parallels the derivation given in Sections 4.2 and 4.3 for the case of discrete sample rotation.

We will again study the growth or decay of the Fourier modes with wavevector $\boldsymbol{k}$. By simply rotating our coordinate system if necessary, we can arrange to have $\boldsymbol{k} = k\hat{\boldsymbol{x}}$.

Let us suppose once more that the behavior of the stationary sample is governed by Eqs. (4.2) and (4.3). To obtain the equations of motion that apply when the sample is rotating with constant

angular velocity, we transform to a frame of reference which rotates with the sample: we set

$$X = x\cos(\omega t) + y\sin(\omega t) \tag{4.56}$$

$$Y = -x\sin(\omega t) + y\cos(\omega t) \tag{4.57}$$

as in Ref. [173]. Equations (4.2) and (4.3) remain valid but with x and y replaced by X and Y. We then use the relations

$$\partial_X = \cos(\omega t)\partial_x + \sin(\omega t)\partial_y \tag{4.58}$$

$$\partial_Y = -\sin(\omega t)\partial_x + \cos(\omega t)\partial_y \tag{4.59}$$

to obtain the equations of motion in the laboratory frame of reference.

We next seek a solution of the form (4.4) with $\boldsymbol{k} = k\hat{\boldsymbol{x}}$. We find that Eq. (4.5) still applies, but the 2×2 matrix $\hat{A}$ now depends on both the wavenumber k and the time t. That matrix is still given by Eq. (4.6), but in Eqs. (4.7) - (4.10) we must make the replacements

$$\begin{aligned} k_x &\rightarrow k\cos(\omega t) \\ k_y &\rightarrow -k\sin(\omega t). \end{aligned} \tag{4.60}$$

The resulting time-dependent matrix $\hat{A} = \hat{A}(k,t)$ has period $t_0 = 2\pi/\omega$.

As a concrete example, we once again turn our attention to the simplified version of Problem II in which the equations of motion for the stationary sample are given by Eqs. (4.13) and (4.14). For

the case in which the sample is rotating with angular velocity ω,

$$\hat{A} = \begin{pmatrix} ivk\cos(\omega t) - \tilde{D}k^4 & 1 \\ ik\cos(\omega t) - \tilde{D}'k^4 & -1 \end{pmatrix}. \tag{4.61}$$

Our task at this point is to solve the system of two ordinary differential equations (4.5) with the matrix $\hat{A}$ given by Eq. (4.61). This was done numerically using Mathematica. Figure 4.5 — which is the continuous analog of Fig. 4.1 — shows the critical influence of the period t_0 on the stability of a mode with a particular value of k. Figure 4.6 demonstrates that the selected wavenumber $k_{\max}$ depends on ω and that it can exhibit jump discontinuities as ω is varied, just as in the case of repeated discrete rotations by 180°. These results establish that the effects described in Section 4.4 are not anomalous features of the case of discrete rotation.

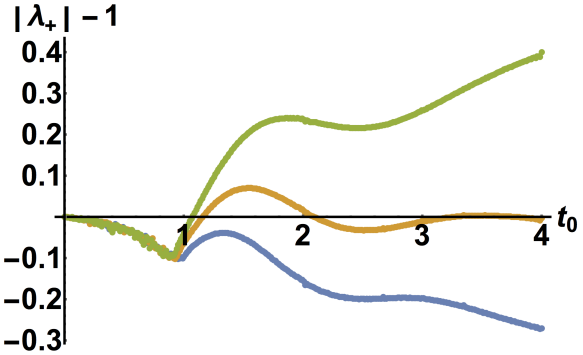

Fig. 4.5 Plots of $|\lambda_+| - 1$ vs t_0 for $v = -0.9$ (blue points), -0.8 (orange) and -0.7 (green). For each of the three plots, $\tilde{D} = 10^{-4}$, $\tilde{D}' = 0$ and $k = 11.46$. Just as for the discrete case, a particular wavenumber k may be made either stable or unstable by a suitable choice of t_0.

4.6 Discussion

In sequential ion beam sputtering (SIBS), a target is bombarded by a sequence of ion beams. Each beam may have a distinct ion energy and direction of incidence. SIBS permits the fabrication of patterns that cannot be obtained by bombarding with a single ion beam. For example, oblique-

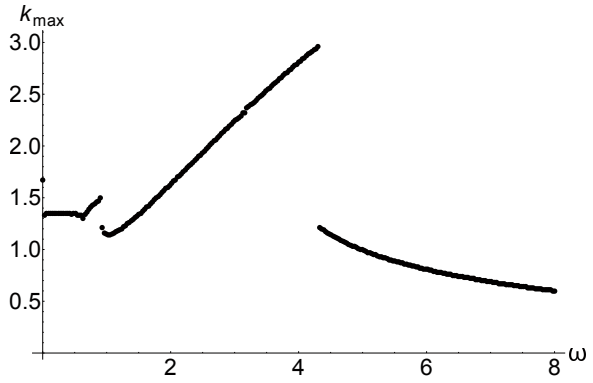

Fig. 4.6 A plot of the selected wavenumber k_{max} vs. ω for the parameters $\tilde{D} = 10^{-4}$, $\tilde{D}' = 0$ and $v = -0.92$. Notice that by a suitable choice of ω the wavelength of the resulting pattern can once again be tuned through a wide range of values.

incidence bombardment of an Au (100) surface with an Ar^+ beam followed by a period of normal-incidence bombardment resulted in the formation of a novel topography in which the surface was covered by parallel chains of nanodots.[182,183] Another type of SIBS produces ripples with substantially fewer defects than bombardment with only one beam.[184]

An experimental study of a particularly simple type of SIBS was carried out by Kim *et al.*, who first bombarded a sample for a time with an obliquely-incident ion beam, and then rotated the sample azimuthally by 90° before bombarding for a second time interval.[185,186] Kinetic Monte Carlo simulations of this process are in qualitative agreement with the results of these experiments.[174]

In this chapter, we explored the effect of periodic discrete rotations of a binary target material by 180° during oblique-incidence ion bombardment. This too is a type of SIBS. To the best of our knowledge, our study is the first in which the effect of SIBS on a binary material has been investigated.

Concurrent bombardment of an elemental material with multiple ion beams has also been studied in the hope that it too could lead to new types of pattern formation. Carter was the first to consider the effect of bombardment with two identical diametrically-opposed ion beams, although

he came to the conclusion that this could produce temporally-oscillating standing waves through the interference of counter-propagating ripples.[187] In fact, it is easy to see that this simply leads to a ripple pattern that does not propagate, and this has been confirmed in simulations.[174] Vogel and Linz later investigated the effect of bombardment with four identical beams with their azimuthal angles differing by 90°.[188] Adopting the damped anisotropic Kuramoto-Sivashinsky as the equation of motion, they found that well-ordered square arrays of nanodots could form for a range of parameter values.

It would be both expensive and impractical to bombard a sample with four identical ion beams. Vogel and Linz therefore suggested that much the same effect could be achieved by bombarding the sample surface with a single obliquely-incident ion beam if the sample was periodically and discretely rotated by 90° increments, provided that the dwell time Δt was small. Arguing in the same way, one could conclude that the effect of bombarding with dual diametrically-opposed ion beams could be reproduced with a single obliquely-incident ion beam if the sample was periodically and rotated by steps of 180° provided that Δt was small. This is certainly true for elemental target materials. However, this statement is *not* valid in general if two atomic species are present in a layer at the surface of the solid. To see this, note that in the case of the example we studied in Section 4.4, Eq. (4.55) shows that there is an instability no matter how small the dwell time Δt is if the parameter v is greater than -1. In contrast, if there are two diametrically-opposed beams and the sample is stationary, the terms proportional to u_x drop out of the equations of motion (4.13) and (4.14). There is no instability as a consequence.[153]

In the case of an elemental material, the only effect that periodic, discrete rotations by 180° have is that in the frame of the sample, the ripples move back and forth as their amplitude grows. The wavelength of the ripples has exactly the same value as it would if the sample were stationary.

Surprisingly, this is not necessarily so if two different atomic species are present at the sample surface. In particular, as we saw for the example we studied in Section 4.4, the wavelength of the ripples depends on the dwell time Δt. In general, therefore, the wavelength has a different value for a particular finite Δt than it does for $\Delta t = \infty$. This behavior is a consequence of the coupling between the surface topography and composition.

For the sake of simplicity, here we have confined our attention to the early time regime in which the surface is nearly flat and consequently the linearized equations of motion are valid. This permitted us to obtain the exact solution to the coupled equations of motion for a sample rotating in discrete increments of 180° for arbitrary values of the model parameters. At longer times, nonlinear terms in the equations of motion must be taken into account if the sample surface is unstable.

4.7 Comparison to Floquet Theory

In this section, we will make a connection between the solution constructed in Section 4.3 and the Floquet theory of systems of ordinary differential equations with coefficients that vary periodically in time.[181] In that theory, solutions of the matrix equation

$$\frac{dY}{dt} = \hat{J}(t)Y \tag{4.62}$$

are sought, where $\hat{J}(t)$ is an $N \times N$ matrix that has entries that are periodic functions of t with period t_0 and $\boldsymbol{Y} = \boldsymbol{Y}(t)$ is an N-component column vector. The fundamental solution matrix $\hat{\Phi} = \hat{\Phi}(t)$ for this equation is an $N \times N$ matrix whose columns are solutions to Eq. (4.62) and that reduces to the identity matrix for $t = 0$. One of the key results of the Floquet theory is that $\hat{\Phi}(t)$ may be written in

the canonical form

$$\hat{\Phi}(t) = \hat{P}(t)\exp(\hat{B}t), \tag{4.63}$$

where $\hat{P}(t)$ is an $N \times N$ matrix with period t_0 and $\hat{B}$ is a constant $N \times N$ matrix.

The matrix $\hat{C} \equiv \exp(\hat{B}t_0)$ is known as the monodromy matrix; its eigenvalues are called the characteristic multipliers. Each eigenvalue λ of $\hat{C}$ has an associated characteristic exponent κ defined by the relation

$$\lambda = \exp(\kappa t_0). \tag{4.64}$$

Let $\kappa_{\max}$ be the characteristic exponent with the largest real part. The growth rate R is then $\mathrm{Re}\,\kappa_{\max}$.

In the problem considered in Section 4.3, $N = 2$, the period t_0 is $2\Delta t$, and

$$\hat{J}(t) = \begin{cases} \hat{A} & \text{for } 2n\Delta t \le t \le (2n+1)\Delta t \\ \hat{A}^* & \text{for } (2n+1)\Delta t \le t \le (2n+2)\Delta t, \end{cases} \tag{4.65}$$

where n is an arbitrary integer. The general solution given in Eqs. (4.20) and (4.21) shows that

$$\hat{\Phi}(t) = \exp\left(\hat{A}(t - 2n\Delta t)\right)\hat{L}^n \tag{4.66}$$

for $2n\Delta t \le t \le (2n+1)\Delta t$ and that

$$\hat{\Phi}(t) = \exp(\hat{A}^*[t - (2n+1)\Delta t])\exp\left(\hat{A}(\Delta t)\right)\hat{L}^n \tag{4.67}$$

for $(2n+1)\Delta t \le t \le (2n+2)\Delta t$, where n is again an arbitrary integer. Setting t to zero in Eqs. (4.63) and (4.66), we immediately find that $\hat{P}(0) = \mathbb{I}$. Because $\hat{P}(t)$ is periodic with period $2\Delta t$, it follows that $\hat{P}(2\Delta t)$ is also the identity matrix. Therefore, when we set t to $2\Delta t$ in Eqs. (4.63) and (4.66), we

obtain

$$\hat{\Phi}(2\Delta t) = \hat{L} = \exp(2\Delta t \hat{B}) \tag{4.68}$$

and hence

$$\hat{B} = \frac{1}{2\Delta t} \ln(\hat{L}). \tag{4.69}$$

The monodromy matrix $\hat{C}$ is therefore $\hat{L}$. Finally, we compare Eq. (4.63) to Eqs. (4.66) and (4.67) for $0 \leq t \leq 2\Delta t$. This yields

$$\hat{P}(t) = \begin{cases} \exp(\hat{A}t)\exp(-\hat{B}t) & \text{for } 0 \leq t \leq \Delta t; \text{ and} \\ \exp(\hat{A}^*(t-\Delta t))\exp(\hat{A}\Delta t)\exp(-\hat{B}t) & \text{for } \Delta t \leq t \leq 2\Delta t. \end{cases} \tag{4.70}$$

$\hat{P}(t)$ is obtained for all times simply by recalling that it is a periodic function of t with period $2\Delta t$.

A serious limitation of Floquet theory is that no general method of finding $\hat{P}(t)$ or the characteristic multipliers is known.[181] Each differential equation with periodic coefficients must be analyzed from scratch, and in many cases that have been studied an analytical solution has not been found. In the case of our problem, however, we have succeeded in finding both $\hat{P}(t)$ and the characteristic multipliers λ_+ and λ_-.

4.8 Conclusions

In this chapter we explored the effects of sample rotation with a finite angular velocity during ion sputtering of binary materials. We also studied pattern formation on an initially elemental target that is rotated while being subjected to ion bombardment and concurrent deposition of a second atomic species. The early time regime in which linearized equations of motion are valid was investigated in detail.

An analytical general solution was obtained for the case in which the sample is periodically rotated in discrete steps of 180°. This solution revealed that it is possible to change the wavelength of the emergent ripple pattern by changing nothing but the frequency ω with which the discrete rotations of the sample are made. Moreover, a small change in ω can lead to a large change in the wavelength. The rate with which the surface roughens or smooths also depends on ω. Our numerical work shows that analogous phenomena occur if the sample is rotated not discretely, but instead with a constant angular velocity. All of these intriguing kinds of behavior are consequences of the coupling between the surface morphology and composition and cannot occur if two atomic species are not present at the surface of the solid.

CHAPTER 5

SAMPLE ROCKING

5.1 Introduction

Ion bombardment has the potential to be an extremely useful and economical way of producing patterns which have a characteristic length of tens of nanometers and which are well ordered over much longer distance.[168] A longstanding issue in this field, however, is the high density of defects in the patterns that typically form. This problem is the primary obstacle that prevents widespread use of ion bombardment as a nanofabrication tool, and much work has been done toward the goal of producing very well ordered patterns.[189,190,77,184,158,191,152,86] To date, no experiment has yielded highly ordered patterns on an elemental sample using a noble gas ion beam.

In this chapter, we present the results of numerical simulations of an elemental surface that is bombarded by a broad beam of noble gas ions with a polar angle of incidence that varies periodically in time. In an experiment, this could be achieved by rocking the sample about an axis orthogonal to the surface normal and the incident ion beam. We assume that the target material is amorphous, or that a surface layer is amorphized by the ion bombardment. We take the equation of motion in the absence of rocking to be the usual anisotropic Kuramoto-Sivashinsky (AKS) equation.[115,117,168] For a discussion of the history and physical interpretation of the AKS equation see Subsection 2.6.1. Several of the coefficients in this equation depend on the angle of incidence, and so periodic sample

rocking has the effect of making these coefficients periodic in time. We show that a remarkable and unforeseen degree of order emerges for a broad range of parameters in both one-dimensional (1D) and two-dimensional (2D) simulations. Thus, temporally periodic driving can lead to near perfect spatial periodicity.

5.2 Results in One Dimension

The equation of motion for the unrocked solid surface is the much-studied AKS equation,[141,142,192,193]

$$u_t = v_0' u_x - A u_{xx} + A' u_{yy} - B\nabla^4 u + \left(\lambda u_x^2 + \lambda' u_y^2\right)/2, \tag{5.1}$$

where u is the deviation of the surface height from its unperturbed steady-state value; x and y are the horizontal coordinates parallel and perpendicular to the projection of the ion beam direction onto the surface, respectively; t is the time; and the subscripts x, y, and t denote partial derivatives. All of the constant coefficients A, A', λ, λ' and B will be taken to be positive save for λ. The AKS equation has long been used as a model for the time evolution of an ion bombarded surface[115,117] and expressions that relate the coefficients to the underlying physical parameters have been given.[13,41,117] v_0' in Eq. (5.1) may be eliminated by transforming to a moving frame of reference, and so will be dropped for the remainder of this chapter.

In this section, we specialize to the case in which u is independent of y. This reduces Eq. (5.1) to the 1+1 dimensional Kuramoto-Sivashinsky (KS) equation,

$$u_t = -A u_{xx} - B u_{xxxx} + \lambda u_x^2/2. \tag{5.2}$$

For the case of time-independent coefficients, the KS equation can be rescaled to a completely parameter-free form by setting

$$u = (A/\lambda)\,\tilde{u}, \quad t = (B/A^2)\,\tilde{t}, \quad \text{and} \;\; x = \sqrt{B/A}\,\tilde{x}, \tag{5.3}$$

where $\tilde{u}$, $\tilde{t}$, and $\tilde{x}$ are the dimensionless surface height, time, and lateral coordinate, respectively.

To investigate the effects of periodic rocking on the pattern formation, we focus on the special case in which the sample is bombarded for a time $t = \pi/\omega$ at an angle of incidence θ_1, then for an equal time at an angle of incidence θ_2, and so forth. Without loss of generality, we may express the values of A and λ at these angles as

$$\lambda(\theta_1) = \lambda_0\,(1+r_1), \qquad A(\theta_1) = A_0\,(1+r_2), \tag{5.4}$$

$$\lambda(\theta_2) = \lambda_0\,(1-r_1), \quad \text{and} \;\; A(\theta_2) = A_0, \tag{5.5}$$

where $r_1 > 0$ and r_2 are dimensionless parameters and λ_0 and A_0 are constants. While $A(\theta)$ and $\lambda(\theta)$ are not simple functions of the angle of incidence θ, because we are switching the angle of incidence discretely, we only need the values of A and λ at two angles.

Because neither $\lambda(\theta)$ nor $A(\theta)$ is a monotone function[117] of θ, it is possible to choose values of θ for which $A(\theta_1) = A(\theta_2)$ and $\lambda(\theta_1) \neq \lambda(\theta_2)$. Thus, by a suitable experimental setup, a periodic, discrete variation in λ can be achieved while minimizing or eliminating any variation in A. As shown below, oscillations in A can be detrimental to the formation of highly ordered patterns, and should be minimized when possible. For simplicity, we assume that B is independent of θ. This is the case for sample temperatures high enough that the surface diffusion is thermally activated.[168]

Using exponential time differencing,[160,161] we have performed numerical integrations of Eq. (5.2) with λ and A periodically and discretely switching between the values given by Eqs. (5.4) and (5.5). We employed the rescaling given by Eq. (5.3) with A and λ replaced by A_0 and λ_0, respectively. The initial condition was low amplitude spatial white noise. The results are nothing short of astonishing. Figures 5.1 and 5.2 show the results of two simulations, one with rocking and one without, in real space and Fourier space. While the KS equation without rocking yields a surface which has a high degree of disorder, albeit with a characteristic length scale, the rocked KS equation with dimensionless frequency $\tilde{\omega} \equiv \omega B/A_0^2 = 0.15\pi$ produces ripples that are almost perfectly periodic. Figure 5.3 shows spacetime plots of time sequences taken from the same simulations. These demonstrate that without rocking the system exhibits the spatio-temporal chaos characteristic of the KS equation.[141,142] On the other hand, following a brief transient state, the rocked sample displays an extremely high degree of order which persists over time. Larger domain sizes L, finer spatial and temporal discretizations, and much longer simulation times have been investigated numerically, and give comparable results to those shown in Figs. 5.1 - 5.3.

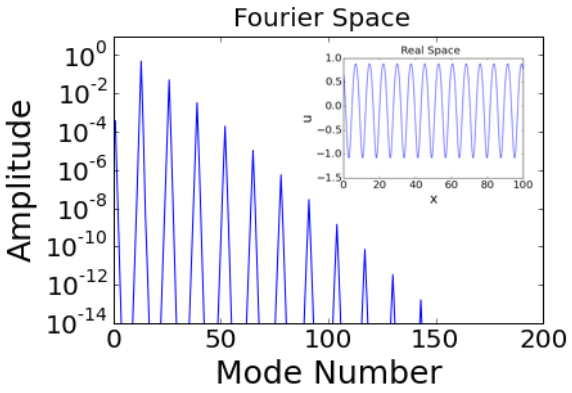

Fig. 5.1 Plots of the rocked surface in real space (inset) and in Fourier space for $r_1 = 2$, $r_2 = 0$, dimensionless frequency $\tilde{\omega} \equiv \omega B/A_0^2 = 0.15\pi$, domain length $L = 100$, and $\tilde{t} = 10^3$.

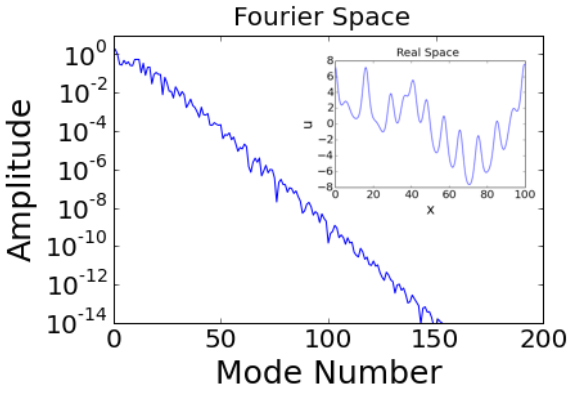

Fig. 5.2 Plots of the unrocked surface in real space (inset) and in Fourier space for $r_1 = r_2 = 0$, $L = 100$ and $\tilde{t} = 10^3$.

The oscillations in ripple amplitude evident in Fig. 5.3(a) may be explained by a scaling argument. As discussed above, if A and λ are time-independent constants, then Eq. (5.2) may be written in a parameter-free form via the rescaling given by Eq. (5.3). This shows that the characteristic ripple amplitude is proportional to $|A/\lambda|$. For the case in which the sample is rocked and $r_2 = 0$, we therefore expect that after a sudden change in the value of λ, the amplitude of the ripple pattern will evolve toward the amplitude associated with the new value of λ. When $|\lambda|$ decreases the ripples grow larger in amplitude, and when $|\lambda|$ increases the amplitude attenuates.

An intuitive understanding of the order produced by rocking may be gained by a heuristic argument. Consider what happens to the surface when $|\lambda|$ changes from a large value to a small value at a time t_1. In the moments before the switch, the term proportional to λu_x^2 in the rocked KS equation is on average comparable to the linear terms $-Au_{xx} - Bu_{xxxx}$ since in the steady-state limit, the ripple growth rate averages to zero. Immediately after the switch, therefore, the term $\lambda u_x^2/2$ will typically be small compared to the linear terms. Consequently, we expect the Fourier transform of the surface height $\tilde{U}(k,t)$ to grow approximately as

$$\tilde{U}(k,t) \simeq \tilde{U}(k,t_1) \exp\left((Ak^2 - Bk^4)\ (t - t_1)\right), \tag{5.6}$$

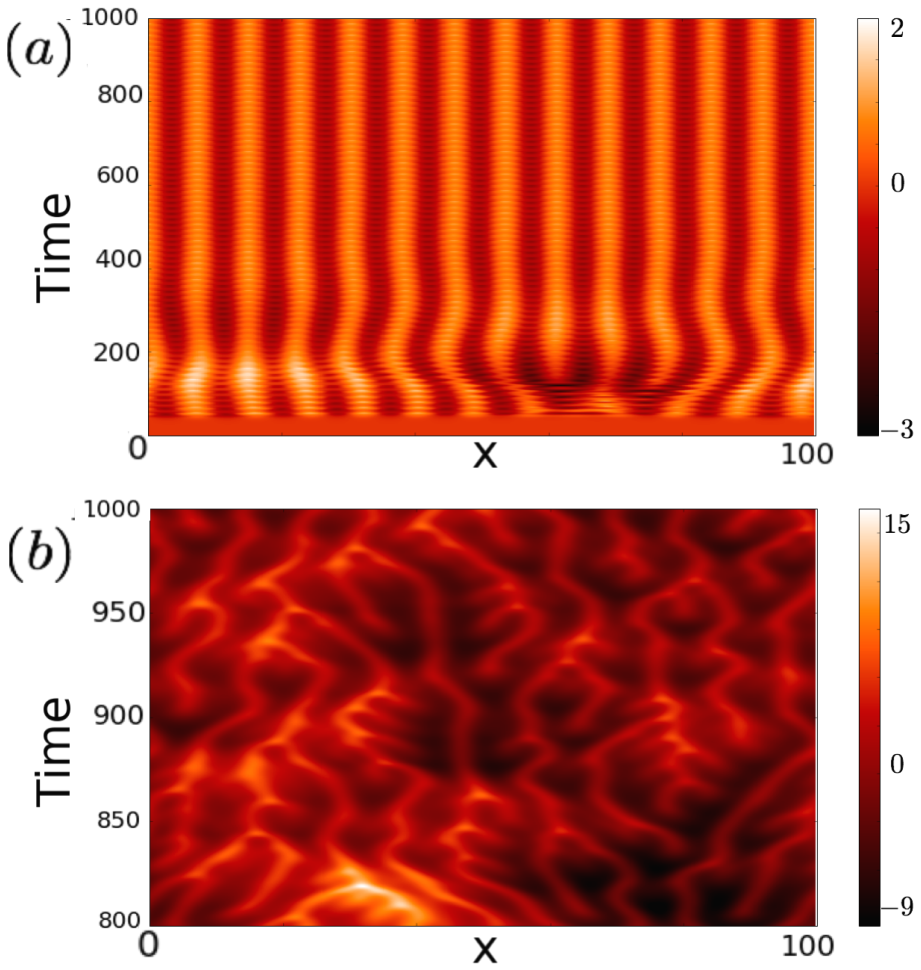

Fig. 5.3 Spacetime plots of the surface for (a) $r_1 = 2$ (rocked), and (b) $r_1 = 0$ (unrocked) respectively with $\tilde{\omega} = 0.15\pi$ and $r_2 = 0$. A shorter time scale was used for the unrocked case so that the finer structure is visible. For clarity, these plots show the deviation of the surface height from its average value.

where k is the wave number. Thus, periodically reducing the value of $|\lambda|$ allows the surface to periodically grow roughly as it would in the linear approximation. Ripples described by Eq. (5.6) become increasingly well ordered because the peak in the Fourier spectrum becomes higher and narrower as time passes. Conversely, when the value of $|\lambda|$ is increased, the amplitude gained during the stage of approximately linear growth attenuates according to the scaling argument given above. This ensures that the ripple amplitude does not become so large that higher order nonlinear effects would have to be taken into account. This explanation suggests that good order will not be

obtained if λ oscillates about an average value of zero, since then there is no opportunity for nearly linear growth to take place.

The excitation of Fourier modes which are multiples of the selected wave number seen in Fig. 5.1 arises as a consequence of the coupling between modes induced by the nonlinear term $\lambda u_x^2/2$. A large amplitude mode with wavenumber k will directly excite the mode of wavenumber $2k$. The coupling between these two modes will then excite the mode of wavenumber $3k$, and so on.

To characterize the quality of the order produced by the rocking procedure, we fit the peak surrounding the highest amplitude wavenumber in the Fourier spectrum to a Gaussian and record its width. In order to avoid sampling at the same point in each rocking cycle, the fits were performed at hundreds of randomly selected times throughout a given simulation and then averaged.

Figure 5.4 shows the width of the highest peak in the Fourier spectrum as a function of the rocking frequency for two values of r_1. It is clear that the effect of rocking is strongly dependent on the frequency with which the sample is rocked. However, within a broad range of frequencies, the surface becomes highly ordered for $r_1 = 4$, making this procedure feasible to implement experimentally. One important conclusion drawn from our simulations is that, just as our heuristic argument suggested, it is essential that $r_1 > 1$ (so that λ changes sign periodically) for good order to form. This is also illustrated by Fig. 5.4, since good order is not obtained for $r_1 = 0.5$. Increasing r_1 further than $r_1 = 4$ has the effect of slightly narrowing the band of frequencies which produce good order and reducing the amplitude of the resulting ripples. Nevertheless, for $1.5 \lesssim r_1 \lesssim 15$, scaled frequencies $\tilde{f} \equiv \tilde{\omega}/2\pi$ between 0.06 and 0.08 produce exceptionally good order.

An important physical consideration is the effect that a periodic variation of the coefficient A in Eq. (5.2) has on the order obtained by rocking. Since this coefficient depends on the angle of incidence, it is likely to vary in general unless θ_1 and θ_2 are carefully selected. For λ and A given

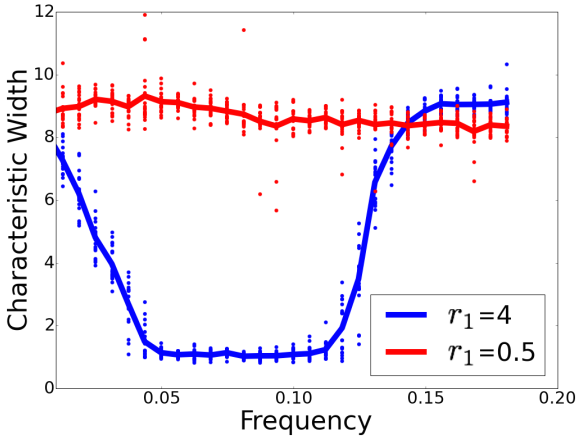

Fig. 5.4 Fourier peak width as a function of the scaled rocking frequency $\tilde{f} \equiv \tilde{\omega}/(2\pi)$ for two values of r_1 and with $r_2 = 0$. Each point represents a single simulation, and the average for each value of the frequency is shown. Note that for $r_1 = 0.5$ (upper, lighter line), λ always has the same sign, while for $r_1 = 4$ (lower, darker line), it changes sign.

by Eqs. (5.4) and (5.5), the characteristic width of the highest Fourier peak for $r_1 = 4$ and a range of r_2 values is shown in Fig. 5.5. For small positive values of r_2, the surface still becomes well ordered, but larger positive values of r_2 do not result in a well ordered surface. If $r_2 < 0$, on the other hand, the high degree of order develops even for relatively large values of $|r_2|$. Thus, the variation in A due to the rocking procedure is not expected to be a significant impediment to producing virtually defect free ripples by sample rocking.

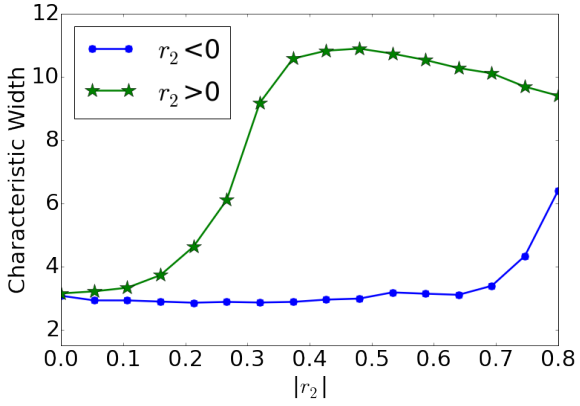

Fig. 5.5 Fourier peak width for $r_1 = 4$ and $\tilde{\omega} = 0.15\pi$ for opposite signs of r_2. For $r_2 < 0$ the surface continues to form nearly perfect ripples for relatively large values of $|r_2|$.

If the order seen in our simulations is to be achieved experimentally, it is crucial that the rocking frequency be chosen within the frequency range discussed above. Fortunately, finding the correct rocking frequency only requires that the linear growth rate be determined for one of the two angles of incidence. The dimensional and nondimensional rocking frequencies are related by $f = 4\sigma\tilde{f}$, where σ is the linear growth rate of the fastest growing mode for that angle of incidence. Experimentally, σ may be approximated by the rate at which the surface roughens at early times, since this roughening will be dominated by the most linearly unstable mode. Simulations indicate that the growth rate during the period where $|\lambda|$ is a minimum determines the optimal rocking frequency. Therefore, if r_1 is greater (less) than zero, then σ should be evaluated at θ_2 (θ_1).

As we have seen, for the rocking procedure to be effective, λ must change sign. There is strong theoretical and experimental evidence that λ passes through zero at a critical angle θ_c for unrocked samples.[117,64] Typically, $60^\circ < \theta_c < 80^\circ$. Given that the amplitude of the surface roughness scales as $|\lambda|^{-1}$, we expect that λ will vanish at the angle of incidence which maximizes the surface roughness. Note that while solutions to the KS equation grow without limit for a spatial white noise initial condition when $\lambda = 0$, the amplitude remains finite in an experiment because a finite ion fluence is used.

The case in which A and λ vary sinusoidally in time has been explored numerically, and was found to produce order comparable to discrete switching. Fig. 5.6 shows the results of two simulations with sinusoidal and discrete variation in λ, respectively. It is clear that discrete switching is not necessary to achieve the improvement in order. More complicated time dependencies are beyond the scope of this chapter, but are not expected to produce substantially different results.

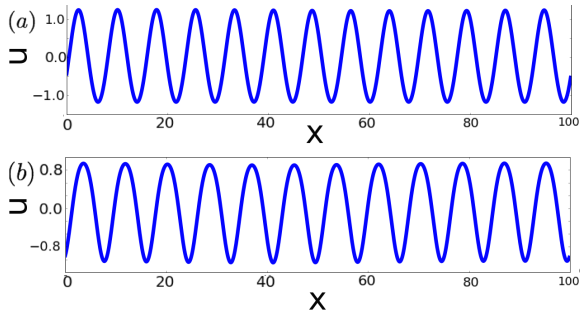

Fig. 5.6 Real space plots of surfaces produced by (a) a sinusoidal and (b) a discrete variation of λ, respectively. For both surfaces $\tilde{\omega} = 0.15\pi$, $r_2 = 0$, $L = 100$, and $t = 10^3$. In (a) $\lambda = 1 + 5\sin(\omega t)$ whereas in (b) $\lambda = 1 + 5\text{sgn}(\sin(\omega t))$.

5.3 Results in Two Dimensions

Given the degree of order that can form on a rocked surface in 1D, it is natural to ask whether a 2D rocked surface will produce similar results. Physically, this means we are no longer requiring that h be independent of y. We return to Eq. (5.1), keeping $v_0' = 0$. With temporally periodic coefficients, Eq. (5.1) is the rocked AKS equation. Panels (a)-(c) of Fig. 5.7 show the surface for a particular set of parameters for which λ oscillates between the values 10 and -6. As in 1D, the unrocked equation of motion displays spatio-temporal chaos with a characteristic length scale (see Fig. 5.7 (d)). The rocked AKS equation, on the other hand, initially forms a transient state which contains numerous defects. The rocking procedure causes these defects to move together and annihilate. Eventually, even long wavelength Fourier modes are suppressed.

The rocked AKS equation has more parameters than the rocked KS equation, and the computational time required for a complete investigation of the parameter space of the rocked AKS equation would be prohibitively long. However, variation in the coefficient λ' is likely unavoidable during rocking, since this coefficient also depends on the angle of incidence θ. We therefore considered the effect of simultaneously varying λ' and λ. The results of a simulation for which

$\lambda' = 2 + 0.2\,\mathrm{sign}(\sin(\omega t))$ and $\lambda = 2 + 8\,\mathrm{sign}(\sin(\omega t))$ are shown in Fig. 5.8. This simulation reveals that periodic oscillations of λ' with this amplitude do not have a detrimental effect on the resultant order for A, A', B, and λ equal to their values in the first three frames of Fig. 5.7.

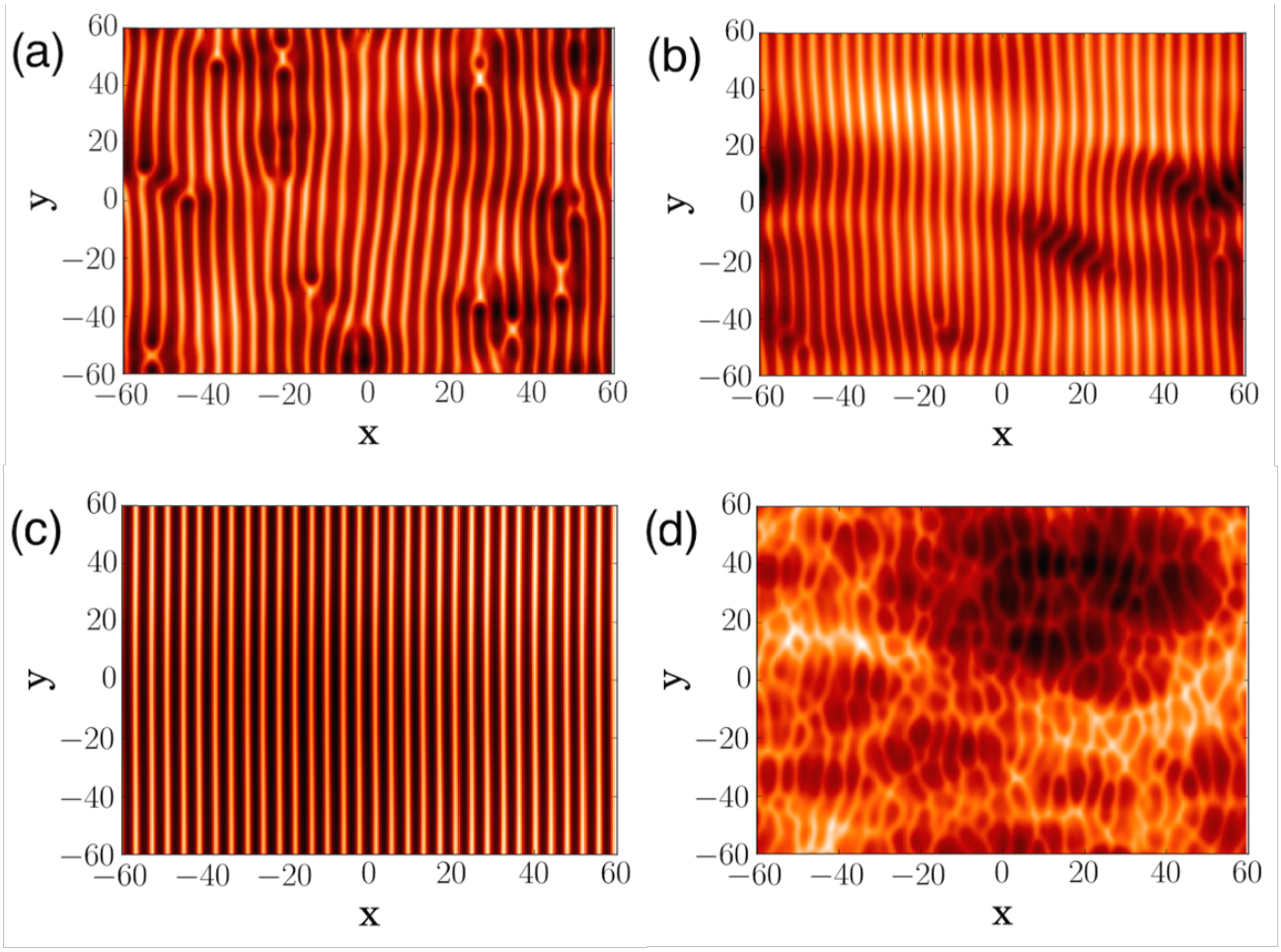

Fig. 5.7 (a) - (c) A time series of a surface for a square domain of side length $L = 120$ with $A = A' = 1$, $B = 1$, $\lambda = 2 + 8\,\mathrm{sign}(\sin(\tilde{\omega}\tilde{t}))$, $\lambda' = 2$, and $\tilde{\omega} = 0.15\pi$ at times $\tilde{t} = 106, 330$, and 1840. (d) A simulation with the same parameters as in (a) - (c) but with $\lambda = 2$ so that there is no rocking. The time is $\tilde{t} = 1840$.

5.4 Discussion

The consequences of a time-periodic coefficient in the KS equation have been considered in the context of annular fluid flow.[194] Due to computational limitations at the time of that work, the

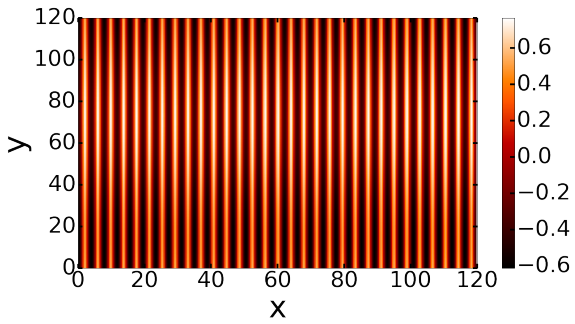

Fig. 5.8 A plot of the surface for a square domain of side length $L = 120$ with $A = A' = 1$, $B = 1$, $\lambda = 2 + 8\,\mathrm{sign}(\sin(\tilde{\omega}\tilde{t}))$, $\lambda' = 2 + 0.2\,\mathrm{sign}(\sin(\tilde{\omega}\tilde{t}))$, and $\tilde{\omega} = 0.15\pi$ at time $\tilde{t} = 1840$.

phenomenon reported here was not discovered. In the first theoretical study of a periodically rocked, ion bombarded surface,[195] several important physical contributions to the dynamics were neglected, including curvature dependent sputtering.[13] In a later theoretical treatment of ion bombardment with sample rocking,[196] nonlinear terms were omitted from the equation of motion and consequently no increase in order was found. Experiments have not yet been performed in which a sample was bombarded while being periodically rocked. Our results give a compelling motivation for conducting experiments of that kind. By contrast, azimuthal sample rotation during ion bombardment has been studied intensively, and gives a means of producing ultra-smooth surfaces,[171,172,173,19] generating hexagonal order,[74] and controlling ripple patterns.[197]

5.5 Conclusion

Our simulations demonstrate that if a sample is bombarded with a broad noble gas ion beam while simultaneously being rocked, nearly perfect nanoscale ripples can result. Unlike other methods,[152,86] ours can be used to produce highly ordered surface ripples on an elemental material and does not require the implantation of an undesirable second atomic species or a high sample

temperature. We also discussed how optimal values of the rocking frequency and the angles of incidence may be determined in an experiment.

CHAPTER 6

BLAZED DIFFRACTION GRATINGS

6.1 Introduction

A blazed grating (BG) is a special type of diffraction grating that is optimized to achieve maximum efficiency in a given diffraction order. It is engineered so that the maximum optical power is concentrated in the desired diffraction order while the residual power in the other orders is minimized. Like every optical grating, a BG has a constant line spacing. However, the lines in a BG have a triangular, sawtooth-shaped cross section, and so the surface has a terraced form. Figure 6.1 shows an example of a typical BG cross section.

Producing high quality BGs for use in optical applications has been an important technological goal for decades.[20] BGs must have feature sizes on the order of hundreds of nanometers, and yet must be well ordered over much longer length scales. In addition, the flatness of the blazed facets is critical to the efficiency of the grating. High efficiency BGs are an essential component in performing some forms of high-precision spectroscopy, which itself has a wealth of applications.[20]

In this chapter, we introduce and analyze a new method of fabricating high quality blazed gratings which combines conventional lithographic techniques and bombardment with a broad ion beam. When a nominally flat solid surface is bombarded with a broad ion beam at oblique incidence, nanoscale ripples often develop on the surface.[168] The surface typically develops a

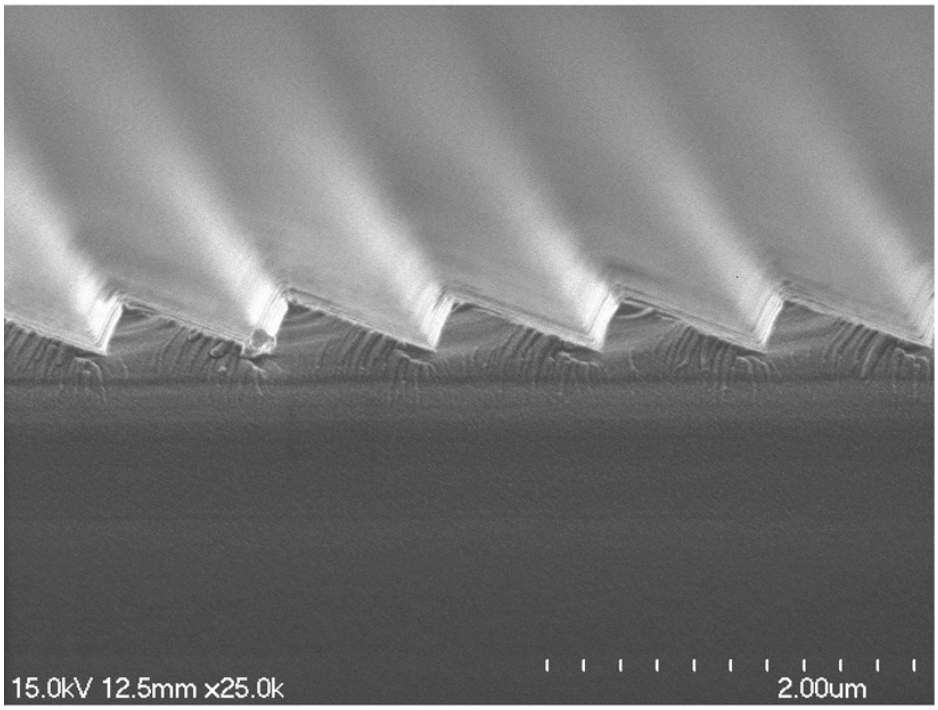

Fig. 6.1 Cross section of a BG made using ion bombardment. This SEM image was taken from Ref. [8]

terraced form at the late stages of its time evolution for high angles of ion incidence, i.e., for near grazing incidence.[53,54,55,56,57,58,59,60,61,62,63,51,52,27,64] A height profile taken along the projected ion direction is not sinusoidal. Instead, as we trace along the height profile, the surface slope is nearly equal to a constant value m_+ for a long spatial interval. At some point, the slope changes rapidly, and then is nearly equal to a constant negative value m_- for a long interval. The slope once again changes rapidly at some point, and then is approximately equal to m_+. The height profile continues in this fashion, and so takes on an irregular sawtooth form in which most of the surface has a slope that is nearly equal to one of the two selected slopes m_+ and m_-. For examples of simulated terraced topographies, see Figs. 2.6 and 2.7. For an example of an experimental result displaying terrace formation, see Fig. 2.8.

Our proposed fabrication method is a two-stage procedure for producing high efficiency BGs which takes advantage of the near perfect periodicity produced by conventional lithography and the slope selection that results from bombardment with a broad ion beam at a relatively high angle of incidence. In the first stage, conventional lithography is used to produce a periodic height modulation on the surface of the sample. The second stage consists of bombarding this pre-patterned or "templated" surface with a broad ion beam of noble gas ions at a high angle of incidence. As we shall see, this serves to transform the periodic pattern into a sawtooth form.

Simply bombarding a nominally flat surface is not sufficient to produce an efficient BG, since the surface does not evolve into a state which is nearly periodic.[53,54,56,57,55,58,59,60,62,63,52,27,64] By contrast, conventional lithographic methods produce nearly perfectly periodic structures, but normally fail to achieve the regions of nearly constant slope and the sharp slope transitions characteristic of a high quality BG. Our proposed fabrication method overcomes the shortcomings of broad beam ion bombardment and conventional lithography by wedding the two.

Because traditional lithographic techniques are highly developed, stage one of our procedure does not pose a significant challenge. Suitable periodic patterns have been produced by light interference lithography combined with ion etching as well as by e-beam lithography.[198,4,5,6,7,8] Consequently, we will focus on stage two in this work. In accord with this and for the sake of simplicity, we will refer to the topography that results from the first step of our procedure as the initial surface.

Our simulations give compelling evidence that initial periodic patterns with a broad range of amplitudes and wavelengths may be used to produce a high quality BG. It is important to choose an angle of ion incidence that is large enough that the effect of the key cubic nonlinearity in the equation of motion is significant. By the same token, the amplitude of the initial pattern must be sufficiently large. Most of our simulations of our proposed method of BG fabrication were carried out with sinusoidal initial conditions because any periodic structure of sufficiently high amplitude may be effectively reduced to a sinusoid by annealing the sample.[126] We will, however, demonstrate that both sinusoidal initial conditions and a variety of periodic initial structures can lead to high quality BGs. It is therefore not necessary to precisely tailor the surface produced by the first step of our procedure. Low amplitude surface roughness may also be superimposed on the initial periodic pattern without compromising the efficiency of the resulting BG. Finally, we show that even if additional linear and nonlinear terms are present in the equation of motion for the surface, our method can still produce high quality BGs.

In Sec. 6.2, we will begin by investigating the special case in which the surface is independent of the transverse coordinate y. We will call this the one-dimensional case. In Sec. 6.3, we will extend this analysis to the full two-dimensional problem in which the surface height depends on

both x and y and demonstrate that our conclusions continue to hold in this more general setting. We place our results in context in Sec. 6.4 and present our conclusions in Sec. 6.5.

6.2 One-dimensional Results

Consider a solid surface that has height $h(x,y,t)$ above the arbitrary point (x,y) in the $x-y$ plane at time t. A broad ion beam with the uniform flux $\boldsymbol{J} = -J\hat{\boldsymbol{e}}$ is incident upon the surface, where $\hat{\boldsymbol{e}} \equiv \hat{\boldsymbol{x}}\sin\theta + \hat{\boldsymbol{z}}\cos\theta$ and θ is the angle of incidence. Thus, x and y are the horizontal coordinates parallel and perpendicular to the projection of the ion beam direction onto the $x-y$ plane, respectively.

For simplicity, we first consider the special case in which the surface height h does not depend on the transverse coordinate y, hereafter referred to as the 1D case. We take the time evolution of the ion bombarded surface to be described an extension of the Kuramoto-Sivashinsky (KS) equation[141,142] that includes an additional nonlinear term. The KS equation has been widely used[168,115] as a model of ion sputtering of surfaces, but is not sufficient to describe experiments in which terraced topographies develop. In order to better model the surface, a term proportional to u_x^3 is appended to the KS equation.[65] The resulting equation of motion is

$$h_t = -v_0 + v_0' h_x - \kappa h_{xx} - B h_{xxxx} + \frac{c_2}{2} h_x^2 + \frac{c_3}{6} h_x^3, \tag{6.1}$$

where v_0 is the erosion velocity of an unperturbed flat surface, v_0', κ, B, c_2, and c_3 are constants, and the subscripts x and t denote partial derivatives. The constant B is positive, and we restrict our attention to the case in which $\kappa > 0$ so that ripples form if a nominally flat surface is bombarded.

Equation (6.1) has been has been shown to model the terracing and coarsening behavior seen in experiments quite well.[65] From a physical standpoint, the terms proportional to v_0, h_x, h_x^2, and h_x^3 result from an expansion of the sputter yield of the surface to third order in the slope h_x. The term proportional to κ on the right-hand side of Eq. (6.1) represents a curvature dependent instability, which is in general due to a combination of curvature dependent sputtering[13] and the Carter-Vishnyakov[41] mechanism. The term proportional to B accounts for the effects of thermally activated surface diffusion[126] and ion-induced viscous flow.[127] For more background on Eq. (6.1), see Subsection 2.6.2. The solutions to Eq. (6.1) are propagating trains of undercompressive shocks at sufficiently long times. The shocks are the regions in which the slope changes rapidly; they are separated by regions of nearly constant slope. Undercompressive shocks have been observed in other models of ion bombardment as well.[143, 146, 145, 144]

To simplify the equation of motion (6.1), we transform to a moving frame of reference given by

$$x' = x + v_0' t \tag{6.2}$$

and

$$u = h + v_0 t, \tag{6.3}$$

which eliminates the first two terms on the right-hand side of Eq. (6.1). Further simplification is achieved by introducing the dimensionless quantities

$$\begin{aligned} \tilde{u} &\equiv \frac{c_2}{\kappa} u, \\ \tilde{t} &\equiv \frac{\kappa^2}{B} t, \\ \tilde{x} &\equiv \operatorname{sgn}(c_3) \sqrt{\frac{\kappa}{B}} x', \end{aligned} \tag{6.4}$$

and

$$\gamma \equiv \frac{|c_3 \kappa^{\frac{3}{2}}|}{c_2^2 \sqrt{B}}. \tag{6.5}$$

Substituting Eqs. (6.4) and (6.5) into Eq. (6.1) and suppressing the tildes results in the nondimensional 3KS equation,[199]

$$u_t = -u_{xx} - u_{xxxx} + \frac{1}{2}u_x^2 + \frac{\gamma}{6}u_x^3. \tag{6.6}$$

A single non-negative free parameter γ remains in the equation of motion. The parameter γ may be interpreted as an indication of the relative strength of the cubic and quadratic nonlinearities, or as an indication of the degree to which the lack of reflectional symmetry about the $y-z$ plane influences the surface evolution. Since the nonlinear terms render this equation resistant to analytical techniques, we will impose periodic boundary conditions and integrate it numerically using exponential time differencing.[160] This method has been widely used to integrate nonlinear partial differential equations, and is both accurate and efficient.[161]

We will use the first-order diffraction efficiency as a gauge of the quality of the BGs that our fabrication method produces. The first-order diffraction efficiency is defined to be the fraction of the incident power that is diffracted into the first-order diffraction mode. To evaluate the efficiency of the gratings produced by our simulations, we implemented a numerical simulation of diffraction using the scalar diffraction approximation.[200] For low blaze angle gratings, polarization effects are negligible and this approach is quite accurate.[20,200]

For the efficiencies reported here, we use the first-order Littrow configuration, which means that the location of the first-order diffraction peak coincides with the light source itself. For brevity, the first-order diffraction efficiency in the first-order Littrow configuration will be referred to as the efficiency for the remainder of this chapter.

The scalar diffraction approximation assumes coherent monochromatic light is incident on the BG from a single angle of incidence. Each point on the BG'S surface is considered to be a source of spherical waves whose initial phase depends on the phase of the light incident at that point on the surface. Similarly, the amplitude of this spherical source is proportional to the projected incident intensity at that point. In order to determine the diffraction pattern of the grating as a whole, the contributions of the spherical waves emanating from each discretized point on the surface are combined to yield the intensity at a plane of constant z. The distance between this plane and the BG is much greater than the width of the BG. If the incidence angle and wavelength of the light are chosen appropriately, a good BG produces a spatially narrow band of high intensity centered on a particular position in this plane.

There is an important subtlety that must be addressed before we compute the diffraction efficiencies of surfaces generated by numerically integrating Eq. (6.6). The dimensionless equation of motion (6.6) was obtained by scaling vertical and horizontal distances in different ways, as seen in Eq. (6.4). Before we simulate the diffraction of light using the scalar diffraction approximation, however, we must rescale the surface so that the horizontal and vertical scales are the same.

If all of the coefficients in Eq. (6.1) are known, we can restore the dimensions and transform a dimensionless surface obtained from a simulation to the corresponding dimensional one. However, it is actually sufficient to specify the quantity $\sqrt{\kappa^3/(c_2^2 B)}$, since this is the dimensionless ratio between the vertical and horizontal scales. Blaze angles on the order of 6° are typically observed in experiments in which terraced surfaces develop.[61,51,52,64] In order to obtain comparable blaze angles in our simulations, we chose $\sqrt{\kappa^3/(c_2^2 B)} = 3 \times 10^{-3}$ for all simulations described in this chapter. The quantity $\sqrt{\kappa^3/(c_2^2 B)}$ is the ratio of the characteristic height and width of the structures which result from the ion bombardment. All other things being equal, experiments in which this

combination of parameters is large will have steeper features than experiments in which this ratio is small.

To evaluate the quality of the BG produced by the two-step procedure in a way that is invariant under rescaling, we define a slope fraction quality factor Q as follows:

1. Determine the slope u_x of the surface at N equally-spaced discrete points.

2. Produce a histogram of slopes with N_B bins such that the bin centers are evenly spaced, every point has a corresponding bin, and the bins corresponding to the greatest magnitude slopes are not empty. Identify the most populated bin. $N_B = 16$ for all results shown here.

3. Find the total number of points on the surface which fall inside the most populated bin.

4. Divide this total by the total number of surface points N to obtain the fraction of the surface that has a slope close to the most common slope. The Q value is this fraction expressed as a percentage, so that a perfect sawtooth surface with vertical antiblazed faces would have $Q = 100\%$ and a completely noisy surface will have on average $Q = 100\%/N_B$.

While our choice of N_B is not fundamental, we have chosen $N_B = 16$ so that computing Q produces results similar to the first-order diffraction efficiency calculated using the scalar diffraction approximation. Furthermore, Q has the desirable property that it is invariant under a change of aspect ratio.

In order to determine the optimal initial conditions for producing a blazed grating, we performed many simulations for different values for the wave number K_0 and amplitude A_0 of an initially sinusoidal surface. For simplicity, in what follows we will refer to the nondimensional integer $\tilde{K}_0 \equiv K_0 L/(2\pi)$ as the wave number and suppress the tilde. Here L is the sample length. We also

added low amplitude spatial white noise to the initial conditions. This had a maximum value of 0.01% of the amplitude of the initial condition. As asserted above, a low noise sinusoid may be produced by annealing any periodic initial pattern provided that the initial pattern has sufficiently high amplitude and very little long wavelength noise. We therefore expect these initial conditions to be well within the reach of conventional lithographic methods. The impact of initial conditions with a noise amplitude greater than 0.01% of the amplitude of the sinusoid itself is explored below.

A simulation of a typical 1D surface profile for a low amplitude white noise initial condition is shown in Fig. 6.2. A terraced topography emerges with an inconsistent spacing between shocks. For appropriately selected initial conditions, however, the results of ion bombarding a templated surface are impressive. Figure 6.3 shows the initial and final state for a templated surface governed by the equation of motion (6.6). In what follows, we will explore the necessary conditions for a good BG to be produced by our method.

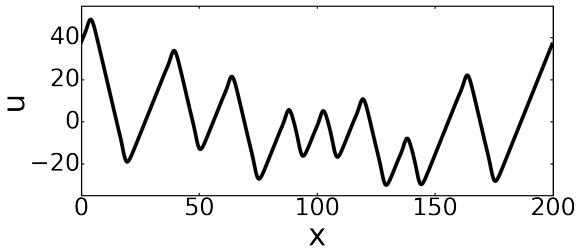

Fig. 6.2 A typical solution to Eq. (6.6) with a low amplitude spatial white noise initial condition. Notice the preponderance of two selected slopes and the inconsistent spacing between peaks. The parameter value was $\gamma = 1$ and total bombardment time was $t = 600$. In addition, the domain size L was 200 and the number of gridpoints N was 441.

Figure 6.4 shows the Q values for a range of initial conditions. For all values of K_0, an increase in the amplitude A_0 results in an increase in Q, i.e., an improvement of the resulting grating. This is readily understood, since the term proportional to u_x^3 in Eq. (6.6) is responsible for the formation of terraces. The magnitude of this term scales as the cube of the initial amplitude and hence its relative

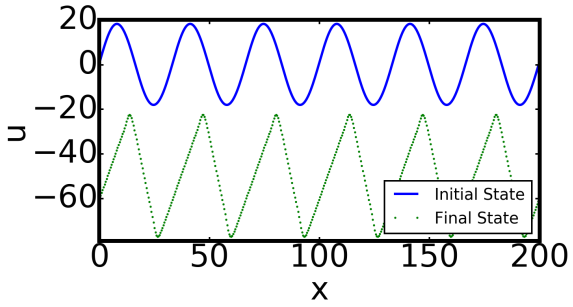

Fig. 6.3 An example of the influence of ion bombardment on an initially sinusoidal surface topography. The initial condition (solid blue) and final state (dotted green) are shown with a vertical offset for clarity. The parameter value was $\gamma = 1$ and the total bombardment time t was 100. The initial condition amplitude, initial condition wave number, sample size, and the number of gridpoints were $A_0 = 20$, $K_0 = 6$, $L = 200$ and $N = 441$, respectively.

importance in the dynamics grows with the initial amplitude. Conversely, for very small values of the amplitude of the initial sinusoid, the solutions resemble those for a low amplitude white noise initial condition.

A plot of the efficiency as a function of K_0 and A_0 calculated using the scalar diffraction approximation is shown in Fig. 6.5. The surfaces analyzed in Figs. 6.4 and 6.5 are identical, and these plots show good agreement between these two methods of evaluating the quality of BGs.

Figures 6.4 and 6.5 show that there is an optimal value of the initial wave number K_0 that leads to BGs with the highest values of Q and the efficiency. This may be understood by looking at the growth of the Fourier modes with wave number $2K_0$ and $3K_0$. We find that a surface that has a Fourier spectrum that has high amplitudes for the odd multiples of the fundamental (wave numbers $3K_0$, $5K_0, \ldots$, etc.) has a higher value of Q than surfaces with high amplitudes for the even modes ($2K_0$, $4K_0, \ldots$, etc.). To produce such a surface, K_0 should be chosen so that the linear growth rate of the mode with wave number $3K_0$ is larger than the growth rate of the mode with wave number

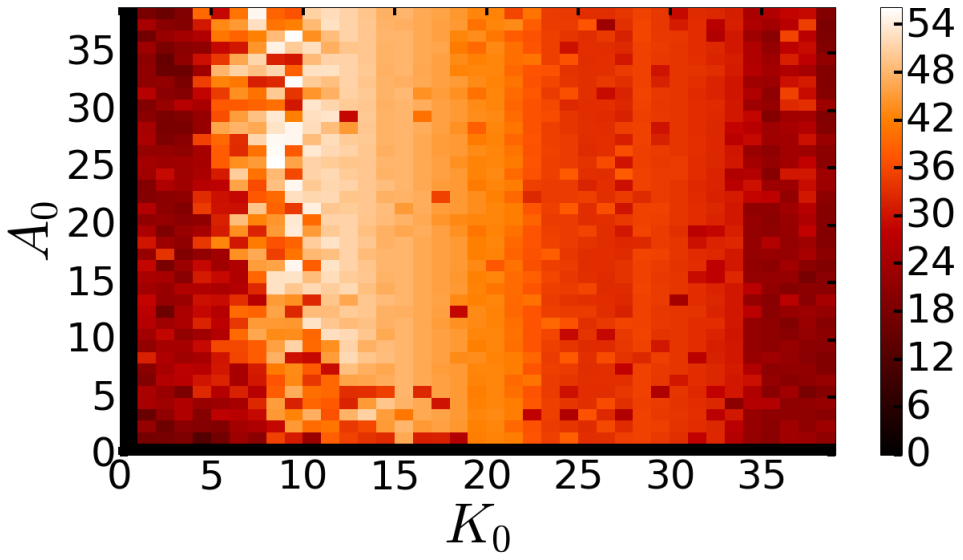

Fig. 6.4 Q evaluated for a 1D surface and a range of initial sinusoids. The amplitude A_0 and wave number K_0 of the initial condition are as labeled, $\gamma = 0.5$, and the total bombardment time t was 80. The sample size and the number of gridpoints were $L = 400$ and $N = 381$, respectively. The mode with the highest linear growth rate has $K_0 = 45$.

$2K_0$. This can be arranged by choosing a value of K_0 small enough that $3K_0$ is less than the value of the wave number K that gives the highest linear growth rate. Thus, the initial sinusoid should have a wavelength larger than three times the linearly selected wavelength.

The periodicity of the initial surface is not disrupted by the ion bombardment. In contrast to the surfaces produced using a low amplitude white noise initial condition, the surfaces produced starting from a template of sufficient amplitude have a very regular spacing between shocks. In order to evaluate the degree of periodicity, for each simulation the highest peak in the Fourier spectrum was fitted to a Gaussian. For small K_0 or A_0, the time evolution leads to an appreciable disruption of the periodicity. However, for the region of the $K_0 - A_0$ plane which produces surfaces with a high value of Q, the periodicity remains nearly perfect. The Gaussian fitting algorithm applied to the simulations with parameters in the range $15 < A_0 < 35$ and $8 < K_0 < 14$ resulted in a maximum nondimensional width of 0.156 at time $t = 80$. By comparison, this algorithm applied to the nearly

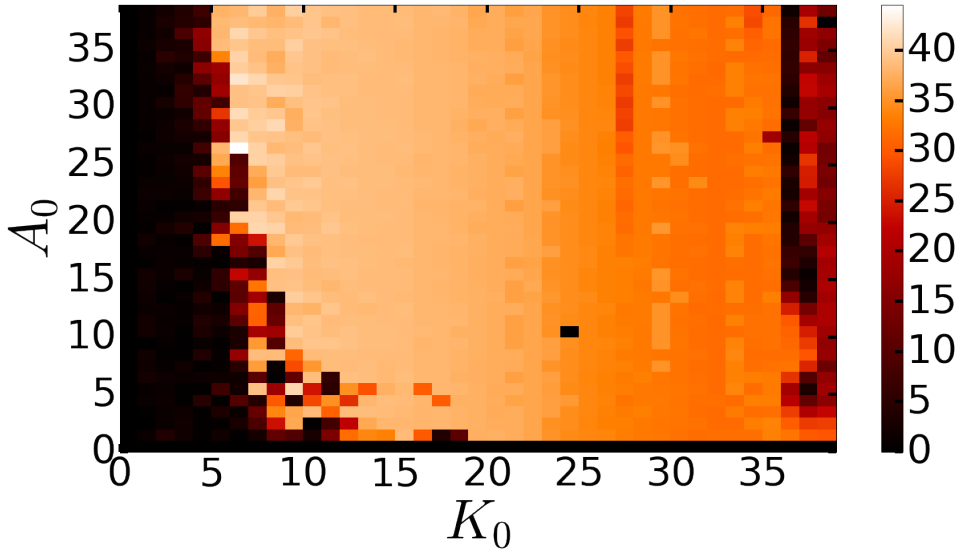

Fig. 6.5 First order Littrow efficiency evaluated for a 1D surface and a range of initial sinusoids. The surfaces analyzed are identical to those in Fig. 6.4.

perfectly periodic sinusoidal initial condition produced a nondimensional characteristic width of 0.125, implying that the surfaces remain highly periodic during the ion sputtering.

Reducing the value of the coefficient γ does affect the quality of the BG produced. However, this effect is rather small provided that γ remains above a threshold value. Figure 6.6 shows Q and the diffraction efficiency for a range of γ values for surfaces which had the same templated initial condition. Surfaces below the threshold value of γ (which is approximately $\gamma = 0.27$ for the simulations shown in Fig. 6.6) typically exhibit a reduction of the period by a factor of two as a result of the strong influence of the u_x^2 term relative to the u_x^3 term. As seen in Fig. 6.7, the even overtones of the initial wave number are driven so strongly that the number of maxima and minima of the surface double, and so a BG with the desired wavelength is not produced. Another feature that Fig. 6.6 demonstrates is that Q is closely related to the diffraction efficiency of the grating.

Although the absolute efficiency is a function of the particular rescaling chosen, the slope fraction quality factor Q is clearly a useful way of identifying well formed BGs. The gradual decrease in efficiency with increasing γ that occurs for $\gamma > 0.27$ results from the fact that the magnitude of the slope of the antiblazed faces decreases more quickly than the magnitude of the slope for the blazed faces when γ is continually increased. As a consequence, for surfaces formed by Eq. (6.6) with a large value of γ, a smaller fraction of the incident light strikes the blazed faces.

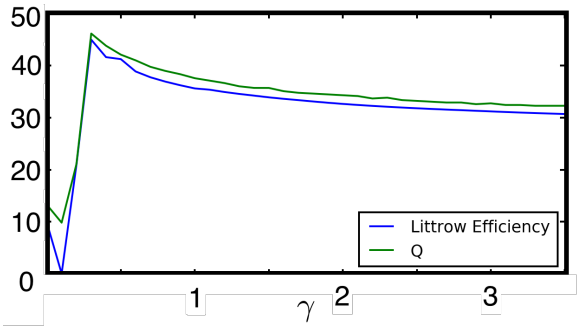

Fig. 6.6 A plot of Q (upper green line) and the diffraction efficiency (lower blue line) for a range of γ values on surfaces which had a sinusoidal initial condition. Above a threshold value, changing the magnitude of γ has a modest effect on the quality of the BG produced. The parameters were $A_0 = 30$, $K_0 = 6$, $N = 641$, $L = 100$, and the total bombardment time t was 60.

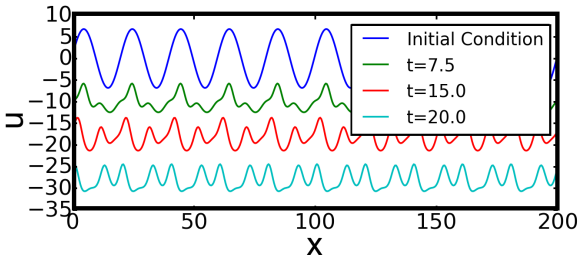

Fig. 6.7 A time sequence showing the period halving that results from an insufficiently large value of γ. In this case, shocks do not form. For this simulation $\gamma = 0.2$, $A_0 = 7.5$, $K_0 = 10$, $N = 441$, and $L = 200$. For clarity, downward offsets have been applied to the surfaces. These offsets increase in magnitude as we go from $t = 0$ to $t = 20.0$.

It has been shown previously that the coefficient γ determines the values of the selected slopes.[65] Since γ depends on the angle of incidence and the periodicity of the pattern is selected by the initial condition, it is likely possible to adjust the parameters of the BG to select for a particular frequency of light and diffraction order.

Figure 6.8 shows the values for the selected slopes obtained from simulations with sinusoidal initial conditions. The slopes are in excellent agreement with the predictions of Ref. [65]. These results demonstrate that the slopes may indeed be varied over a wide range by varying γ when sinusoidal initial conditions are employed.

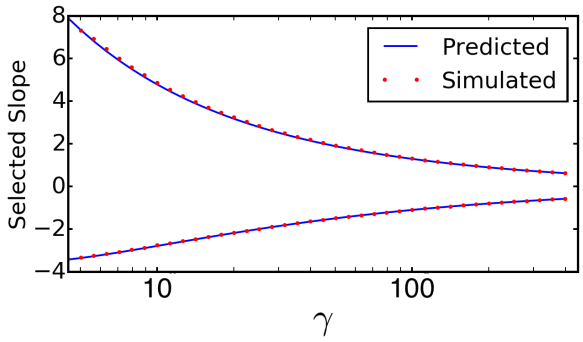

Fig. 6.8 The selected slopes for simulations with a sinusoidal initial condition and the prediction of previous work on the 3KS equation (6.6).[65] The simulation parameters were $A_0 = 20$, $K_0 = 3$, $L = 100$ and $N = 181$. The total bombardment time was 120.

Simulations of the 3KS equation (6.6) with low amplitude white noise initial conditions have revealed that increasing γ leads to an increase in the density of shocks in the long time limit.[66] One might therefore ask whether changing the value of γ used in simulations starting from a templated surface would affect the shock density and therefore the overall periodicity of the final pattern. The answer to this question is no, provided the initial amplitude is sufficiently large, $\gamma > 0.27$, and the amplitude of the superimposed noise is sufficiently low. Put simply, if the initial pattern has points which have sufficient curvature to initiate the formation of a shock, then shocks will form only at these locations and nowhere else. For a sinusoidal initial condition, this results in the points of

maximal curvature sharpening into shocks. Figure 6.9 shows a spacetime plot of the local maxima and minima during bombardment. The extrema of the initial sinusoid become the extrema of the BG.

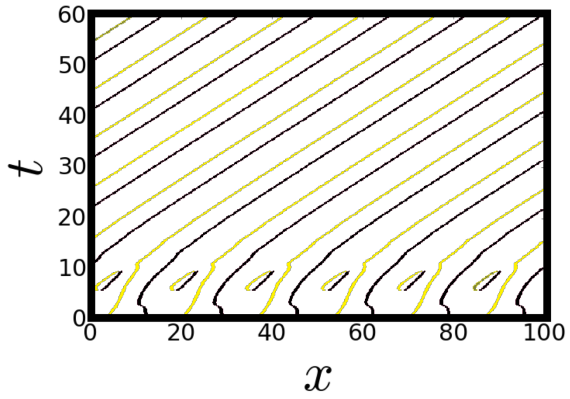

Fig. 6.9 A spacetime plot of the local maxima (black) and minima (yellow) for a typical templated surface. There are transient pairs of maxima and minima during the formation of the BG, but the initial extrema persist and become the extrema of the surface in its steady state. For this simulation, $\gamma = 1$, $A_0 = 20$, $K_0 = 6$, $L = 100$ and $N = 351$.

6.2.1 Possible Additional Contributions to the Equation of Motion

In the equation of motion (6.6) for the surface, we retained a term which is third order in ∂_x and u, but did not include a term proportional to u_{xxx}, which is also third order in ∂_x (although it is only first order in u). We now consider the effect that such a term has on the evolution of a templated surface that would otherwise develop into an efficient BG. This term has previously been considered in the context of ion bombardment in Ref. [201]. In that work it originated from stress in the bombarded material. A term proportional to $u_x u_{xx}$ will not be considered because it produces unphysical singularities.[202]

Figure 6.10 shows the effects of adding a term $r_1 u_{xxx}$ with nonnegative r_1 to the right-hand side of Eq. (6.6). We chose to simulate a surface with an initial condition that produced a good BG

for $r_1 = 0$ and $\gamma = 1$. As r_1 increases, the Littrow efficiency of the BG declines, but the effect is relatively modest.

The sign of r_1 is of critical importance to the success of our fabrication method. If r_1 is negative, the surface evolution is qualitatively different. As we have stated, the 3KS equation (6.6) produces shock waves that propagate along the surface. A related equation of motion, which is obtained from Eq. (6.6) by setting $\gamma = 0$ and adding the term $r_1 u_{xxx}$, is known as the Benney equation and may be written

$$u_t = -u_{xx} - u_{xxxx} + \frac{1}{2}u_x^2 + r_1 u_{xxx}. \tag{6.7}$$

The solutions to Eq. (6.7) for sufficiently large r_1 are trains of solitons which propagate along the surface.[203] These solutions give some insight into the effect that the added $r_1 u_{xxx}$ term has on solutions to Eq. (6.6). Both Eqs. (6.6) and (6.7) produce patterns which propagate along the surface with velocities dependent on the values of γ and r_1, respectively. If the propagation directions of the solitons and the undercompressive shocks are the same (i.e., r_1 is positive), the formation of a BG is largely unaffected by the additional term $r_1 u_{xxx}$. If, however, these propagation directions are opposite to one another, then we get solutions which resemble counter-propagating trains of solitons and undercompressive shocks. The result is a surface whose Q value is periodic in time and which is at no point suitable for use as a blazed grating. It is therefore of critical importance that the coefficient r_1 be positive or negligibly small.

Fortunately, there is reason to believe that the coefficient r_1 is positive or small. Simulations of Eq. (6.6) with the added term $r_1 u_{xxx}$ with a low amplitude white noise initial condition reveal the same qualitative difference between the cases $r_1 > 0$ and $r_1 < 0$ as the templated simulations. In the former case, we see coarsening into a steadily propagating terraced surface pattern, as observed

experimentally. In the latter, we do not observe coarsening, terracing or an approach to a steady state. Since the experimentally observed behavior is much better described by the case in which $r_1 > 0$, we fully expect this condition to be satisfied if and when our BG fabrication procedure is implemented.

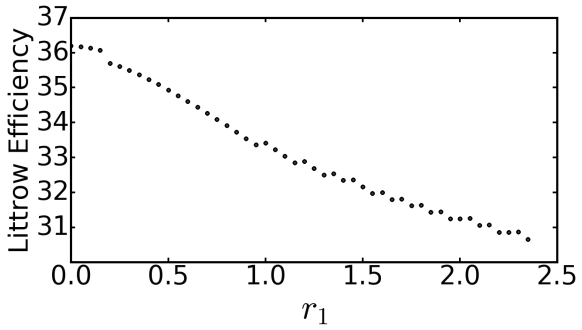

Fig. 6.10 A plot showing the effect that an additional term $r_1 u_{xxx}$ added to the equation of motion (6.6) has on the diffraction efficiency. While the efficiency decreases with increasing r_1, the overall effect is rather small. The simulation parameters were $\gamma = 1$, $A_0 = 10$, $K_0 = 30$, $t = 60$, $L = 500$ and $N = 2051$.

6.2.2 Dependence on the Form of the Initial Pattern

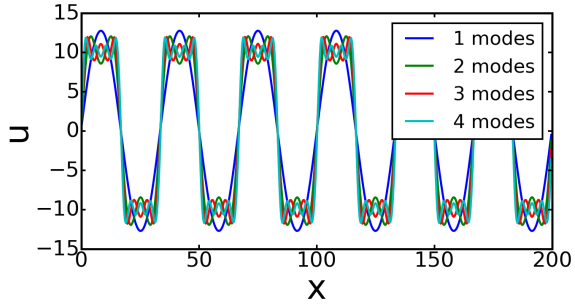

Fig. 6.11 The initial conditions used in the simulations that yielded the surfaces shown in Fig. 6.12. These initial conditions were generated by discarding all but the first m Fourier modes of a square wave and adding low amplitude white noise. The initial conditions shown have $m = 1$, 2, 3 and 4. The amplitude and wave number of the square wave were $A_0 = 10$ and $K_0 = 6$, respectively, and the sample length was $L = 200$.

We have primarily considered sinusoidal initial conditions since they may be produced from any periodic structure of sufficiently high amplitude. A remarkable property of the equation of

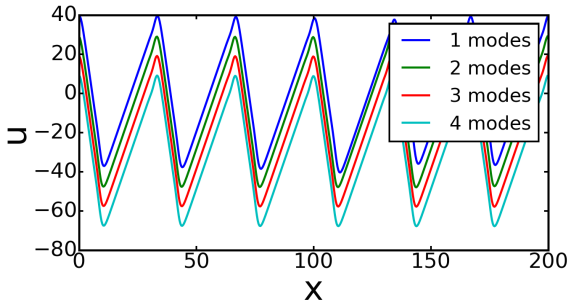

Fig. 6.12 The state of the surface corresponding to the initial conditions shown in Fig. 6.11 at $t = 200$. The value of γ was 0.4. For clarity, the surfaces have been phase shifted so their maxima coincide and have also been vertically offset from one another. It is clear from these results that the differently shaped initial conditions lead to virtually identical steady-state surface shapes.

motion (6.6) is that at long times its solutions are rather insensitive to the detailed shape of the initial surface if it has an appropriate wavelength and amplitude. An illustration of this is shown in Figs. 6.11 and 6.12, which show the results of using various approximations to a square wave as the initial condition and the resulting surfaces at time $t = 50$. The initial conditions were generated by taking the Fourier transform of a perfect square wave, discarding all but the first m modes, and then adding low amplitude white noise. After the surfaces at time $t = 50$ have been translated laterally so that their maxima coincide, they become virtually indistinguishable.

While it is not possible to examine all possible initial surface shapes, specific examples such as those shown in Fig. 6.11 indicate that a great variety of periodic initial surfaces may be used to produce a high quality BG. Other examples of initial conditions that were used as starting points for simulations include successive approximations to a sawtooth profile, square profiles and good BGs smoothed by annealing (not shown). In all cases considered, the final surface was virtually unaffected by the details of the initial surface shape apart from its period and amplitude. We expect this insensitivity to be a significant advantage of our proposed two-stage procedure for the fabrication of BGs.

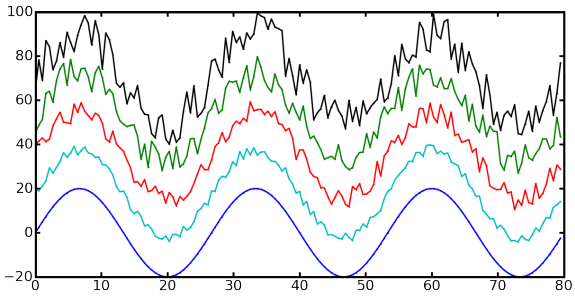

Fig. 6.13 Sinusoidal initial conditions with added noise of various amplitudes, shown with vertical offsets for clarity. The added noise ranges from 0.01% (lowermost, blue line) to 100% of A_0 (uppermost, black line). The corresponding final states are shown in Fig. 6.14. The simulation parameters were $K_0 = 3$, $L = 80$, $A_0 = 20$, $\gamma = 1$, $N = 150$, and $t = 500$.

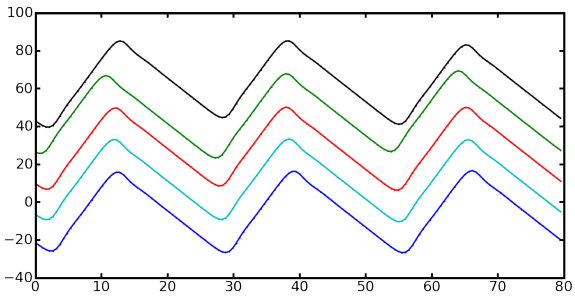

Fig. 6.14 The final state of the simulations with initial conditions shown in Fig. 6.13. For the extremely noisy cases, the periodicity is somewhat disrupted, but the moderately noisy initial conditions form excellent BG profiles. See the caption of Fig. 6.13 for the simulation parameters.

Another demonstration of this insensitivity to initial conditions is given in Figs. 6.13 and 6.14, in which increasingly noisy sinusoidal initial conditions and the corresponding final states are shown. The initial conditions shown in Fig. 6.13 are perfect sinusoids to which spatial white noise has been added. The noise amplitudes chosen are 0.01%, 25%, 50%, 75% and 100% of the amplitude of the sinusoid itself. For the noisiest initial conditions, the periodicity of the final state is somewhat disrupted, but for a 25% level of the amplitude of the added noise, the periodicity remains almost perfect during the ion bombardment.

To make this statement quantitative, we fit the highest peak in the Fourier spectrum of each final surface to a Gaussian function and averaged over ten simulations. The resulting average peak width

— which is a gauge of the degree of periodicity — increased by only 2.5% as the noise amplitude was increased from 0.01% to 25%.

6.3 Two-dimensional Results

In this section, we analyze a two-dimensional generalization of Eq. (6.1) in which u depends on the transverse coordinate y as well as on x and t. It is given by

$$u_t = -\kappa_1 u_{xx} - \kappa_2 u_{yy} - B\nabla^2\nabla^2 u + \frac{c_{1x}}{2}u_x^2 + \frac{c_{1y}}{2}u_y^2 + \frac{c_2}{6}u_x^3 + c_3 u_x u_y^2, \tag{6.8}$$

where $\kappa_1 > 0$, κ_2, $B > 0$, c_{1x}, c_{1y}, c_2, and c_3 are constants, and the subscripts on $u = u(x,y,t)$ denote partial derivatives. In writing this equation of motion, we have replaced the terms proportional to u_{xx}, u_x^2 and u_x^3 in Eq. (6.1) by anisotropic two-dimensional expressions. We have excluded all terms which are not symmetric under the transformation $y \to -y$, since the proposed experimental setup possesses such a symmetry. Physically, the terms proportional to κ_1 and κ_2 result from a generalization of the curvature-dependent instabilities which gave rise to the term proportional to κ in Eq. (6.6). Similarly, the terms proportional to c_{1x}, c_{1y}, c_2, and c_3 result from a small slope expansion of the sputter yield that has been extended to two dimensions.[66]

If Eq. (6.8) were rescaled, four free parameters would remain. This is too large a parameter space to be exhaustively explored. For this reason, we will begin by focusing on the nearly isotropic case in which $\kappa_1 = \kappa_2 \equiv \kappa > 0$, $c_3 = 0$, and $c_{1x} = c_{1y} \equiv c_1$. For this special case, Eq. (6.8) reduces to

$$u_t = -\kappa\nabla^2 u - B\nabla^2\nabla^2 u + \frac{c_1}{2}(\nabla u)^2 + \frac{c_2}{6}u_x^3. \tag{6.9}$$

Later in this section, we will explore the case $c_3 \neq 0$ as well as the effects of reintroducing anisotropies in the terms in Eq. (6.9) that are proportional to $\nabla^2 u$ and $(\nabla u)^2$. For $c_2 = 0$, Eq. (6.9) reduces to the isotropic KS equation, a much-studied model for describing the evolution of a surface bombarded by a broad ion beam at normal incidence. For $c_2 \neq 0$, Eq. (6.9) is a two-dimensional extension of the 3KS equation.

An additional term u_{xyy} is consistent with the symmetry of the system, and will in general appear in the equation of motion. We performed simulations with this term appended to Eq. (6.9) with a coefficient equal to a range of values between -2 and 2, with all other coefficients equal to unity, and did not observe an effect on the average Q value of the resulting surface that exceeded 0.001%.

Since we wish to produce a pattern that varies in the x-direction while suppressing all variation in the y direction, the linear instability in the y-direction should be absent or as weak as possible. In practice, therefore, our fabrication method is expected to work well only for angles of incidence θ small enough that $\kappa_1 \leq \kappa_2$. This is the regime in which terraced topographies develop from a nominally flat initial surface. For higher values of θ, ripples with their wave vector in the y-direction will develop, compromising the efficiency of the gratings. Thus, by studying the case in which $\kappa_1 = \kappa_2$, we will evaluate the efficacy of our fabrication method in an extreme situation in which it might be expected to fail.

We produce a nondimensional form of Eq. (6.9) by setting

$$\begin{aligned} x &= \operatorname{sgn}(c_3)\sqrt{\frac{B}{\kappa}}\tilde{x}, \quad y = \sqrt{\frac{B}{\kappa}}\tilde{y}, \\ t &= \frac{B}{\kappa^2}\tilde{t}, \qquad \text{and} \qquad u = \frac{\kappa}{c_2}\tilde{u}. \end{aligned} \tag{6.10}$$

We take c_2 to be positive without loss of generality and suppress the tildes. Equation (6.9) becomes

$$u_t = -\nabla^2 u - \nabla^2 \nabla^2 u + \frac{1}{2}(\nabla u)^2 + \frac{\gamma}{6} u_x^3, \tag{6.11}$$

where γ is once again given by Eq. (6.5). Note that γ is the only free parameter that appears in this equation of motion.

To extend the definition of the slope fraction quality factor Q to two dimensions, we modify the four part definition of Q described in Sec. 6.2. In particular, in part 1 of the definition, we determine the value of u_x on a square grid of N points. Additionally, in part 2 of the definition, we do not bin the u_x values for any points on the surface whose transverse slope u_y has a magnitude above a threshold value. To retain the invariance of Q under rescaling, this threshold is taken to be a fraction of the mean of the magnitude of the surface slope rather than an absolute quantity. The fraction was taken to be 0.2 for all of the results reported here.

Once again the results of our proposed fabrication method are very encouraging. Figures 6.15 and 6.16 show two views of a surface that was obtained from a sinusoidal initial condition. There are two selected slopes and nearly perfect spatial periodicity, as in 1D. The surface becomes terraced before appreciable disturbances in the transverse direction have time to emerge, even though there is an isotropic linear instability. This is brought into sharper relief if we examine the time-dependence of the surface widths σ_x and σ_y in the x- and y-directions. These are defined to be the average of the root-mean-square deviations of N real-space cross sections in the x- and y-directions, respectively. Exponential growth is clearly visible in the transverse width (see Fig. 6.17). Q attains its maximum value before σ_y has become an appreciable fraction of σ_x. The maximum value,

$Q = 36$, is substantial, and so a high quality BG can be produced by stopping the bombardment at an appropriate time.

The high quality BGs that can be produced from sinusoidal templates contrast sharply with the surfaces that emerge from a low amplitude white noise initial condition. As seen in Fig. 6.18, substantial variation can develop in the transverse direction, and the final state is far from being a well ordered BG. This occurs because the time required to form a terraced state from a low amplitude initial condition is long enough to allow ripples with their wave vector in the transverse direction to form.

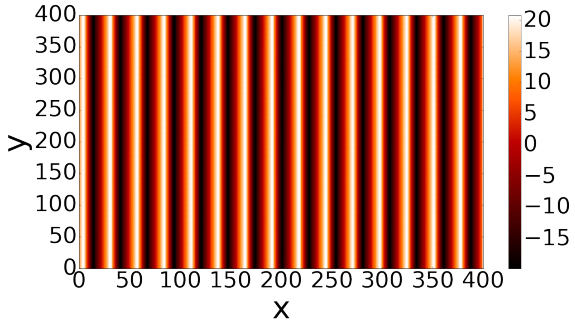

Fig. 6.15 A typical final state for a surface governed by Eq. (6.11) with a sinusoidal initial condition. The simulation parameters were $\gamma = 1$, $A_0 = 10$, $K_0 = 15$, $L = 400$ and $N = 500$, and the total bombardment time was 30.

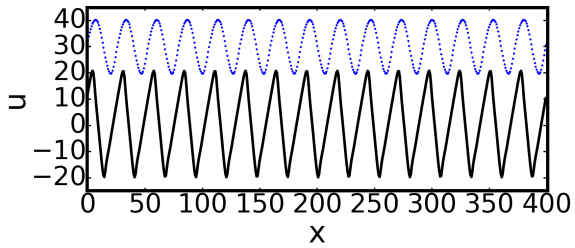

Fig. 6.16 Cross sections taken from the initial (upper blue dots) and final (lower black line) states of the sinusoidally-templated surface shown in Fig. 6.15. These cross sections are nearly identical to the analogous 1D plots shown in Fig. 6.3. The cross sections were taken along the line $y = L/2$ and are shown with a vertical offset for clarity.

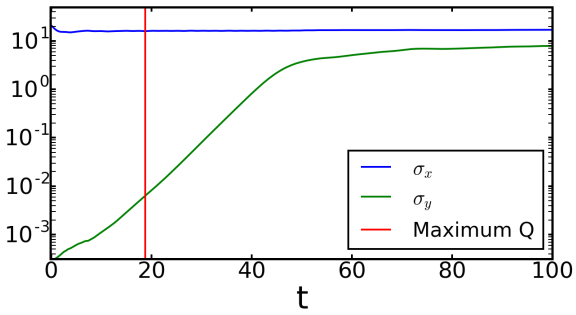

Fig. 6.17 Surface widths σ_x (upper blue line) and σ_y (lower green line) of an initially sinusoidal surface over time. The simulation parameters were $A_0 = 30$, $K_0 = 6$, $L = 100$, and $N = 250$. The vertical red line shows the bombardment duration that gives the BG with the highest value of Q, which was $Q \simeq 36$.

A plot analogous to Fig. 6.4 is given in Fig. 6.19. We see that the results are very similar to those found for the 1D case. Our observations regarding the optimal initial amplitude and wave number of the initial sinusoid carry over without change. Similarly, the dependence of Q on the remaining free parameter in the equation of motion (γ) is comparable to the result shown in Fig. 6.6.

6.3.1 Linear Anisotropy

As we have just seen, our method can produce high quality BGs if $\kappa_1 = \kappa_2$. We argued that our fabrication method will work well for $\kappa_1 < \kappa_2$ if it works well for $\kappa_1 = \kappa_2$. We therefore expect that good BGs will emerge for $\kappa_1 < \kappa_2$ if the initial wavelength and amplitude are appropriately chosen. To confirm this, we carried out numerical integrations of Eq. (6.11) with γ set to 1 and with $-\nabla^2 u$ replaced by $-u_{xx} + A_2 u_{yy}$ for a particular choice of initial sinusoid and for a range of A_2 values. As shown in Fig. 6.20, Q is substantial for both $A_2 = -1$ (the case of an isotropic linear instability) and for $A_2 > -1$ (the case in which the surface is less unstable in the y-direction than it is in the x-direction). Thus, our expectation is borne out. We also argued that our method will perform poorly if the surface is more unstable in the transverse direction than in the longitudinal

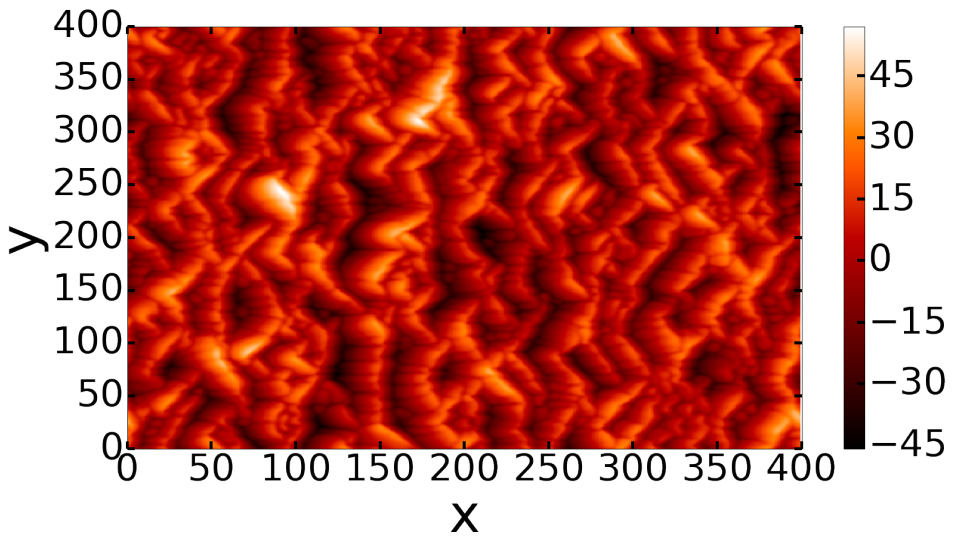

Fig. 6.18 An untemplated surface governed by Eq. (6.11). The simulation parameters were $\gamma = 1$, $L = 400$ and $N = 500$, as in Fig. 6.15. The initial condition was low-amplitude spatial white noise, however, and the total bombardment time was 125.

direction. This too is confirmed by Fig. 6.20, since Q drops precipitously for $A_2 < -1$ and then becomes rather small.

6.3.2 Nonlinear Anisotropy

We also considered the effect of making the quadratic nonlinearity in Eq. (6.11) anisotropic by making the replacement

$$(\nabla u)^2 \to u_x^2 + r_2 u_y^2.$$

We calculated the Q values for a templated surface for a range of r_2 values. For the range $-10 < r_2 < 10$, Q varied by less than 1%. We may qualitatively understand the influence of varying the parameter r_2 by observing that for a surface that has negligibly small values of u_x and its derivatives, u satisfies 1D Kuramoto-Sivashinsky equation with y and t as the independent variables,

$$u_t = -u_{yy} - u_{yyyy} + \frac{r_2}{2} u_y^2. \tag{6.12}$$

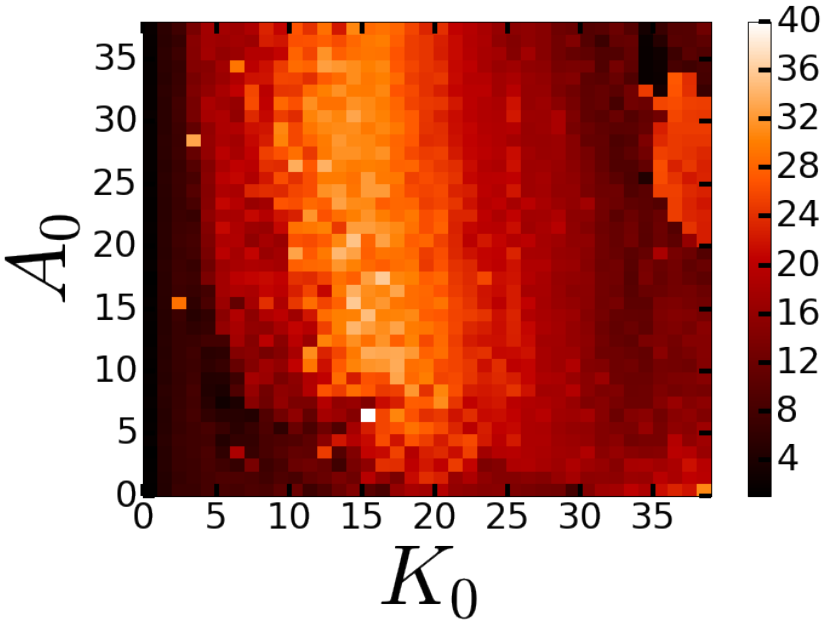

Fig. 6.19 The Q value for two-dimensional simulations with a range of initial sinusoids. The initial sinusoid's amplitude A_0 and wave number K_0 are as labeled, $\gamma = 1$, $L = 400$ and $N = 400$. The Q values shown were averaged over the time interval from $t = 10$ to $t = 50$ to reduce noise.

It is easy to show that the steady-state amplitude of solutions to this equation scale with $|r_2|^{-1}$. It is therefore natural to conclude that if increasing r_2 affects the resulting BGs at all, it improves the BGs produced by reducing the maximum amplitude of ripples with their wave vector in the y-direction. This conclusion is well supported by our simulations. Our simulations also show that the effect of varying r_2 is very small (not shown). Anisotropy in the quadratic nonlinearity is therefore not expected to be an impediment to the successful implementation of our fabrication method.

6.3.3 A Possible Additional Contribution to the Equation of Motion

We now turn to the effect of nonzero c_3 in the equation of motion (6.8). This leads us to append a term $r_3 u_x u_y^2$ to the right-hand side of Eq. (6.11). The resulting equation will be referred to as the semi-isotropic 3KS equation. Figure 6.21 shows the results of simulations of the semi-isotropic

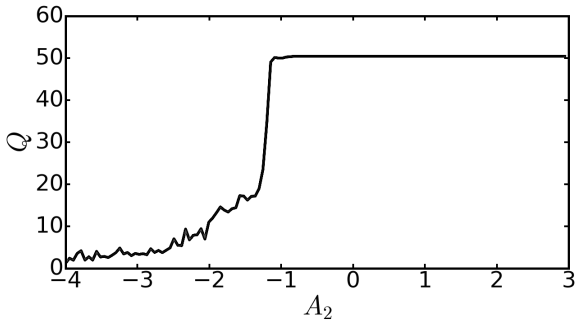

Fig. 6.20 Q values for an initially sinusoidal surface for a range of A_2 values. The simulation parameters were $A_0 = 20$, $K_0 = 6$, $L = 200$, and $N = 250$, and the total bombardment time t was 100.

3KS equation for a wide range of r_3 values. We choose the semi-isotropic case to demonstrate that the presence of the term $r_3 u_x u_y^2$ actually promotes the formation of a high quality blazed grating in the case of a strong transverse instability.

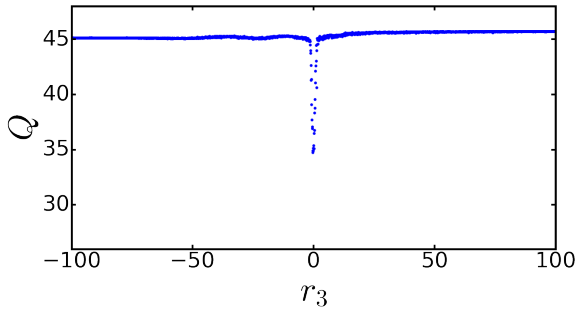

Fig. 6.21 Q values for an initially sinusoidal surface for a range of r_3 values. The simulation parameters were $A_0 = 20$, $K_0 = 6$, $L = 200$, and $N = 250$. The Q values shown represent a temporal average from $t = 10$ to $t = 50$.

6.4 Discussion

Pre-patterned surfaces have been bombarded with broad ion beams to produce novel or highly ordered patterns.[190,182,204] Blazed gratings have also been fabricated in this way.[198,4,5,6,7,8] The basic procedure that has been used is to create regularly spaced lines of photoresist on an initially planar solid surface, and then bombard with a broad ion beam at a high angle of incidence. The

photoresist shadows the surface until it is itself sputtered away, yielding a periodically varying surface height. By carefully selecting the shape of the photoresist lines, one can gradually expose more and more of the underlying solid surface to the ion beam and produce a BG.[198,4,5,6,7,8]

A distinct advantage of our two-stage method is that it could be used as the initial step in the fabrication of multilayer-coated blazed gratings (MBGs) with unprecedented efficiency. Normally, a MBG is produced by depositing a multilayer atop a BG. To obtain a high diffraction efficiency, nearly perfect replication of the sawtooth profile should be achieved during the deposition of every layer that makes up the coating. Each time a new layer is deposited, however, the profile smooths.[205,206,207,208,209,210,21,22,23,24] Cumulatively, this results in considerable rounding and flattening of the profile and so to a significant loss of efficiency. We propose to improve the efficiency of a MBG consisting of alternating layers of materials *A* and *B* by first producing a BG in a substrate composed of *A*. This BG would be produced using our two-stage method. Then, after each new layer of material *A* is deposited, it would be bombarded briefly, partially removing the newly deposited material. The same obliquely-incident ion beam that was originally used to produce the terraced substrate would be used for the bombardment. A layer of material *B* would then be deposited, and so forth. We expect that the bombardment will serve to sharpen the corners in the profile and to very nearly restore it to its original sawtooth form.

Since the angles of the blazed and anti-blazed facets are determined by the choice of ion beam and the substrate material *A*, the success of the proposed method of producing a MBG hinges on first producing a BG by our two-stage method. If the initial sawtooth surface were produced using an alternate fabrication method, ion bombardment of the layers of material *A* would drive the surface to a sawtooth form with different blaze angles than the underlying substrate surface, reducing the efficiency of the MBG.

In the present chapter, we confined our attention to our proposed two-stage method of BG fabrication. Ion-assisted deposition of MBGs atop these BGs will be studied elsewhere.

Recently, there has been work on using ion bombardment to produce BGs without the need for a templating step.[86] Ou *et al.* bombarded a single crystal GaAs target that initially had a nearly flat surface with a normally-incident, low-energy beam of noble gas ions. The target material was maintained at a temperature in excess of its recrystallization temperature. Ou *et al.* found that a terraced surface with a remarkable degree of order emerged with a wavelength of 46 nm. When the surface was illuminated with light of this wavelength, the first-order diffraction peak was readily observed.

While the results of Ref. [86] are exciting, they are limited in their application to the fabrication of blazed gratings. The efficiency of a blazed grating is heavily dependent on having precisely the correct blaze angles and periodicity. The templating procedure described in this chapter allows for selection of the periodicity directly, and control of the blaze angle through variation of the ion incidence angle and energy. By contrast, the method of Ref. [86] is dependent on properties of the underlying crystal to determine the periodicity and blaze angle, and its application is therefore restricted to a narrow range of wavelengths. Furthermore, our method is capable of producing a blazed grating on an elemental target material, while the method of Ref. [86] requires a GaAs or InAs target.

6.5 Conclusions

In this chapter, we introduced and analyzed a novel method for producing high efficiency blazed gratings. Our simulations show that by exploiting the near perfect periodicity of patterns produced by conventional lithography and the terraced topographies which emerge naturally from high-angle, oblique-incidence ion bombardment, one can produce a high quality BG. The effect of the amplitude and wave number of the initial pattern, as well as the influence of the free parameter in the equation of motion, were investigated systematically. Finally, we demonstrated that additional terms which may appear in the equation of motion do not pose a significant impediment to the utility of our proposed method.

CHAPTER 7

MULTILAYER BLAZED GRATINGS

7.1 Introduction

As described in the Chapter 6, a blazed grating (BG) is a special type of diffraction grating that is optimized to achieve maximum efficiency in a given diffraction order. Like every optical grating, a BG has a constant line spacing. However, the lines in a BG have a triangular, sawtooth-shaped cross section, and so the surface has a terraced form.

For light in the extreme ultraviolet or soft X-ray regime, however, a BG often has insufficient reflectivity to perform as desired. This issue may be addressed to some extent by depositing thin layers of alternating composition on a BG, resulting in a multilayer blazed grating (MBG). While MBGs have been shown to possess better efficiencies than BGs, the multilayer deposition process has the unintended consequence of smoothing the surface profile. As a result, even if the initial BG is shaped perfectly, the subsequent layers will become increasingly flat and imperfect as the fabrication proceeds.[21,22,23,24] See Fig. 7.1 for an example of a well formed MBG.

In this chapter, we propose a method of fabricating MBGs that avoids unwanted smoothing and attenuation of the surface profile. Our analysis suggests that by using bombardment with a broad ion beam at oblique incidence during the multilayer deposition process, a nearly perfect BG profile may be retained for an arbitrary number of deposited layers. This work builds upon the previously presented simulations (See Chapter 6 and Ref. [211]) that indicated that ion bombardment could

be used to sculpt a BG from an initially sinusoidal surface for a broad range of parameter values. The work on BG fabrication was in turn based upon the observation that nominally flat surfaces surfaces subjected to ion bombardment can spontaneously form terraced structures for high angles of incidence.[53,54,55,56,57,58,59,60,61,62,63,51,52,27,64]

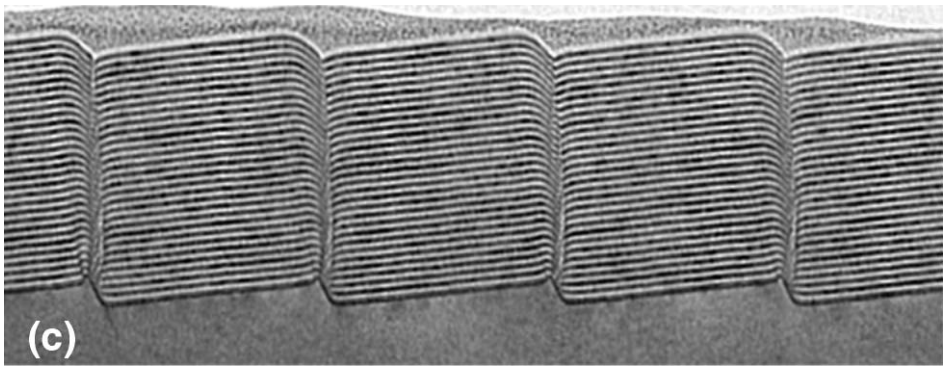

Fig. 7.1 A TEM image of a portion of a typical MBG. This result has been taken from Ref. [21].

Our numerical simulations indicate that our proposed procedure is indeed effective at producing high quality MBGs. Furthermore, for well selected experimental conditions, we find that consecutive BG layers are very similar to one another. This implies that ion beam assisted deposition may be used to fabricate high quality MBGs with an arbitrary number of layers. We examine the necessary and sufficient conditions for which this procedure is successful. This includes a systematic investigation of the influence of the templated initial condition, the material-dependent parameters in the equations of motion, and the experimental geometry.

This chapter is organized as follows. In Sec. 7.2 we will provide background information on MBG design and operating principles. In Sec. 7.3, we describe the proposed fabrication method, introduce some of the equations of motion (EOMs) we will study, and identify the parameter space to be investigated. In Sec. 7.4, we present the results of extensive numerical simulations performed for the special case in which the surface does not vary in the transverse direction, hereafter referred

to as the one-dimensional (1D) case. In Sec. 7.5, we extend the results of Sec. 7.4 to the case of a surface which varies in both the longitudinal and transverse directions, hereafter referred to as the two-dimensional (2D) case. In Sec. 7.6, we place our results in context and review our key findings. Finally in Sec. 7.7 we provide an explicit demonstration of a technique which may be used to select deposition beam parameters in an experiment.

7.2 Background on Multilayer Blazed Gratings

In order for a MBG to operate with high efficiency, the relative positions of consecutive layers in the multilayer stack must be precisely controlled. In order to understand why this is the case, one must first understand the principles govern the operation of a MBG. In what follows, we provide a general description of these principles for a MBG composed of alternating layers of materials B and D. For a more detailed discussion, see Ref. [20].

BGs have a sawtooth form. The nearly flat regions of the surface that face the incident light beam are called blazed faces. Anti-blazed faces, on the other hand, are sides of the sawteeth that face away from the incident light. BGs are optimized for a particular wavelength of light (hereafter referred to as the selected wavelength) at a particular angle of incidence (hereafter referred to as the selected angle of incidence). Consider a well made BG of material B that is illuminated with monochromatic light of the selected wavelength at the selected angle of incidence. The blaze angle is defined to be the angle between the blazed faces and the x axis. This angle is taken to be strictly greater than zero here for simplicity. To obtain an additional simplification, we will consider a BG with vertical anti-blazed faces so that the light exclusively strikes the blazed faces for incidence angles $\theta_i \leq 0$. In general, light of wavelength λ incident on a periodic structure of wavelength d at

angle θ_i will have produce a sequence of local intensity maxima at angles θ_m given by

$$d[\sin(\theta_i) + \sin(\theta_m)] = m\lambda, \tag{7.1}$$

where m is an integer.[20] This is true for a general periodic surface pattern, not just a BG.

In order to gain an intuitive understanding of the operation of a BG, consider now the light intensity as a function of angle from light incident on a single period of a BG. In general, due to the relatively small size of a single grating period, an appreciable fraction of the light will be scattered in a broad range of angles due to diffraction. However, there will also be a maximum in the scattering intensity that corresponds to the incident beam simply reflecting from the flat blazed face.[20] While it is of course true that a complete description of the scattering of light from the surface cannot be captured by simple ray diagrams, it is useful for heuristic purposes to think of the flat blazed faces as simple reflecting surfaces. We will refer to the angle relative to the global surface normal corresponding to a simple reflection from a blazed face as the "reflection angle" (e.g. light propagating in the $-\hat{z}$ direction incident on a surface with the blaze angle θ would have a reflection angle of -2θ relative to the z axis).

A well made BG is constructed in such a way that, for light of the selected wavelength and incidence angle, there exists a value for m in Eq. (7.1) such that θ_m is equal to the reflection angle from a blazed face. The value of $|m|$ for which this is true is often referred to as the order of the grating.[24] The result of the constructive interference between the diffraction due to the periodic pattern and the enhanced reflection due to the blazed faces is that this particular diffraction mode has a much greater intensity than any other mode.[20] One common arrangement is the so-called "Littrow Configuration," in which the propagation direction of the incident light is parallel to the

local normal of the blazed faces. BGs designed to operate in the Littrow configuration can be achieved for any value of m. In general, BGs designed to operate at higher values of $|m|$ are less efficient than lower order gratings, but this is not always the case. In Ref. [24], for example, Voronov *et al.* were able to obtain an improvement in the efficiency of a MBG by increasing $|m|$ from 1 to 2 and doubling the period of their gratings. In this case the improvement was attributed to a reduction of the fraction of the total illuminated area that was not a blazed face.

The principles that govern the operation of a MBG whose top layer is composed of material B (D) are very similar to those for a BG, but now one must consider diffraction and reflection off of three different kinds of interfaces: vacuum/B (D), B/D, and D/B. Depending on the specific material characteristics of the materials B and D and the wavelength of the incident light, some fraction of the incident beam will penetrate the vacuum/B interface at the top of the multilayer stack. Similarly, some fraction of the light which penetrates the first interface will penetrate the underlying B/D interface, and so on throughout the stack.[212,213] For a well made MBG illuminated by incident light with the selected wavelength and angle of incidence, the diffraction and reflection from interface layers in the multilayer stack will constructively interfere with diffraction and reflection from the vacuum/B interface. For light in the extreme ultraviolet or soft X-ray (EUV/SXR) regime, reflection from a single interface is not sufficient for many applications. The enhanced reflectivity of the multilayer stack due to the constructive interference of reflected waves from within the multilayer translates directly into enhanced efficiency of the MBG compared to a BG. Furthermore, because the constructive interference is a wavelength-dependent effect, the multilayer stack acts to further differentiate any incident light which does not have the selected wavelength.[20]

A priori one might expect that the ideal inter-layer thickness in the Littrow configuration would be $\lambda/2$ as measured in the direction normal to the blazed faces. While this satisfies the constructive

interference condition, it in general may not be the choice which maximizes the efficiency of the MBG. This is because for many materials, the absorption of light in the EUV/SXR regime is significant. In many cases it is preferable to choose layer thicknesses which are not optimal with regard to the interference criterion in order to reduce the thickness of layers of a material which has a permittivity with a large imaginary component.[212,213] In general, the optimal values of the thickness of layers of material B and the thickness of layers of material D will depend on many material factors.

7.3 Proposed Fabrication Method

The goal of our proposed procedure is to create a MBG which is composed of alternating layers of materials B and D. Ideally, the surfaces of each of these layers will have a good BG profile. In this section, for the sake of simplicity, we will restrict our attention to the special case that the surface does not vary in the transverse (y) direction. The more general case that the surface depends on both x and y is considered in Sec. 7.5.

The fabrication method we propose is the following: Begin with a surface which has a periodic height modulation in one direction with the periodicity desired for the final MBG. Suitable surfaces have been produced by light wave interference or e-beam lithography.[198,4,5,6,7,8] In what follows, we will take this initial periodic pattern to be a sinusoid, since any sufficiently high amplitude periodic structure may be reduced to a sinusoid by annealing.[126] This pre-patterned, or "templated", surface is then bombarded at a high angle of incidence with a broad ion beam. During this bombardment step, a second beam that deposits material B is also incident on the surface. We will refer to this as stage B, the *B*ombardment with deposition stage. For appropriately selected

conditions, the combined effects of these two beams result in a deposited layer of material B with a surface that is a good BG. Both beams are to have a projection onto the surface parallel or anti-parallel to the wavevector of the periodic initial condition, but will in general have an oblique angle of incidence. The ion beam in particular must be obliquely incident. The time evolution of such a surface in the absence of deposition was the primary focus of Chapter 6 and Ref. [211], and we will not repeat that analysis here. As we will show, the addition of a deposition beam modifies the values of some coefficients in the EOM, but does not affect which terms appear. We therefore expect that ion bombardment with concurrent deposition will produce high efficiency BGs which are similar to those found in Chapter 6 and Ref. [211], if appropriate beam parameters are chosen.

Once a good BG profile has been obtained, the concurrent ion bombardment and deposition of material B is terminated, and a broad beam that deposits material D is activated. Just as for the beam that deposits material B, the azimuthal angle of the beam depositing material D is zero relative to the x axis, but in general it can have a nonzero polar angle. This results in a layer of material D growing on the surface, albeit with a BG profile which degrades as this stage proceeds. We will refer to this as stage D, or the pure *D*eposition stage. Once a suitably thick layer of material D has been deposited, stages B and D are alternately and repeatedly applied. This results in a multilayer stack of layers with BG profiles whose chemical composition alternates between materials B and D in the vertical direction.

Simultaneous bombardment and deposition during stage B reduces our parameter space substantially since we need only consider the effective coefficients in the EOM which arise from the combined effects of deposition and bombardment. For all results presented here, we will begin and end with stage B. This is done so that the initial sinusoidal profile is made into a BG during the first step, and so that the final surface profile is as close to a well formed BG as possible.

We take the EOM for stage D to be a modification of the noiseless Kardar-Parisi-Zhang (KPZ) equation,[214] which is given by

$$h_t = v_D + v'_D h_x + A_2 h_{xx} - \frac{1}{2}\lambda h_x^2, \tag{7.2}$$

where v_D, A_2, and λ are positive constants, $h = h(x,t)$ is the surface height above the point x at time t, and v'_D is a constant. The KPZ equation is a well established model for the time evolution of the surface of a thin film during deposition.[214] The terms v_D and $v'_D h_x$ on the right-hand side (RHS) of Eq. (7.2) come from a small slope expansion of the projection of the deposition current onto the surface. The term proportional to λ results from the assumption that the surface grows along the local surface normal. Finally, the term proportional to A_2 describes the curvature dependent smoothing that occurs during deposition.

The EOM for stage B is taken to be a generalization of the Kuramoto-Sivashinsky (KS) equation[141,142] known as the 3KS equation,[199,65] which is given by

$$h_t = v_B + v'_B h_x - \kappa h_{xx} - \beta h_{xxxx} + \frac{c_2}{2} h_x^2 + \frac{c_3}{6} h_x^3, \tag{7.3}$$

where κ and c_2 are determined by averaging the coefficients that would be produced by sputtering and deposition separately, v_B and β are positive constants, and v'_B and c_3 are constants. By assuming that v_B is positive, we are assuming that the rate of deposition of material B on average exceeds the rate of sputtering due to the concurrent ion bombardment. The term proportional to κ on the RHS of Eq. (7.3) represents a curvature dependent instability, which is in general due to a combination of curvature dependent sputtering[13] and the Carter-Vishnyakov effect.[41] The term proportional

to β, on the other hand, accounts for the effects of thermally activated surface diffusion[126] and ion-induced viscous flow.[127]

The KS equation, which is obtained by setting $c_3 = 0$ in Eq. (7.3), is the most widely accepted model for the time evolution of an ion bombarded surface.[115,168] However, experiments with high angles of ion incidence have shown that the surface develops terraced topographies with two selected slopes that coarsen in time.[53,54,55,56,57,58,59,60,61,62,63,51,52,27,64] In order to explain these experimental results, Pearson and Bradley[65] extended the derivation of the KS equation to account for the effects of the angular dependence of the sputter yield to third order in the surface slope. The terms proportional to v_B, v'_B, c_2, and c_3 on the RHS of Eq. (7.3) result from this expansion. Because we are proposing that the surface be bombarded with an ion beam at a high angle of incidence, this EOM is expected to produce more accurate results than the KS equation would.

During stage D we shall analyze the surface in a frame of reference that moves with a constant velocity $-v'_D$ in the x direction and with a velocity v_D in the z direction. Similarly, during stage B we will analyze the surface in a frame of reference that moves with a constant velocity $-v'_B$ in the x direction and velocity v_B in the z direction. We consider the evolution of the variable u as a function of $\bar{x}$ and t, which are defined as

$$\begin{aligned} u &\equiv h - v_D t \\ \bar{x} &\equiv x + v'_D t \end{aligned} \tag{7.4}$$

during stage D, and

$$\begin{aligned} u &\equiv h - v_B t \\ \bar{x} &\equiv x + v'_B t \end{aligned} \tag{7.5}$$

during stage B. In what follows, we will suppress the bar on x. The EOM for stage D takes the form

$$u_t = A_2 u_{xx} - \frac{1}{2}\lambda u_x^2, \tag{7.6}$$

while the EOM for stage B is

$$u_t = -\kappa u_{xx} - \beta u_{xxxx} + \frac{c_2}{2}u_x^2 + \frac{c_3}{6}u_x^3. \tag{7.7}$$

The solutions to Eq. (7.7) have been studied previously.[199,65,211,66] These solutions develop small regions of rapidly changing slope separated by large regions of nearly constant slope provided that the coefficient of the cubic nonlinearity c_3 is sufficiently large. These constant slopes take on two selected values, which are determined in part by the coefficients of the nonlinear terms. Interested readers are referred to Refs. [65], [66], [199], and [211] for a thorough investigation of the solutions to Eq. (7.7).

For simplicity, we will consider the special case in which the ideal thickness of layers of materials B and D are the same, and, in addition, the desired horizontal translation between adjacent layers is the same for materials B and D (this is the case for the MBGs fabricated in, for example, Refs. [21] and [22]). The extension to the more general case in which the thicknesses of the layers of materials B and D are not the same is straightforward. Let the duration of stages D and B be denoted by T_D and T_B, respectively. The desired layer thickness in the z direction Δh and the desired horizontal translation of the surface pattern between layers Δl are given by

$$T_B v_B = T_D v_D = \Delta h \tag{7.8}$$

$$T_B v_B' = T_D v_D' = \Delta l. \tag{7.9}$$

(The definitions of Δh and Δl are illustrated in Fig. 7.2.) We want the spacing between layers to be consistent as measured in the direction normal to the blazed faces. This is ensured by the condition that Δh and Δl are the same for layers of material B and material D. Equations (7.8) and (7.9) result from general principles of MBG design which are not covered here. Interested readers are directed to Ref. [20] for a thorough description of MBG design considerations.

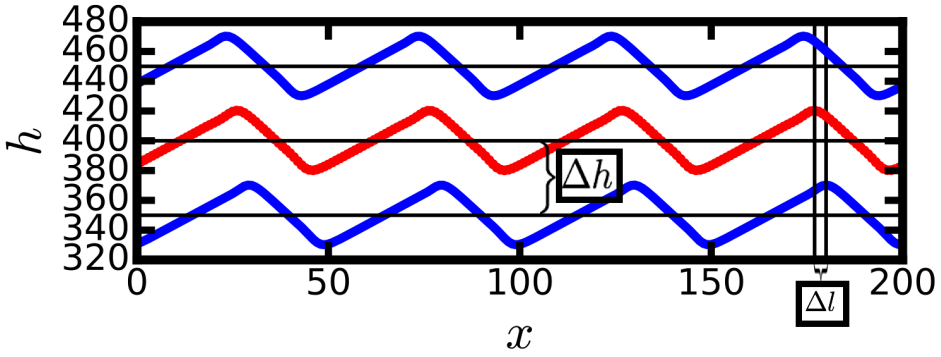

Fig. 7.2 A portion of a typical MBG with the quantities Δl and Δh labeled. See the caption of Fig. 7.3 for the details of the simulation which produced these results. The thin horizontal lines indicate the average value of the height of the layer they intersect. The thin vertical lines indicate the location of a local maximum in the surface height. The red (blue) lines correspond to boundaries between materials D and B (B and D) moving from bottom to top. The simulation parameters were $v_D = 100$, $v_B = 0.5$, $v'_D = 6$, $v'_B = 0.03$, $\gamma = 1$, $r_1 = 0.5$, $A_0 = 30$, $K_0 = 4$, $T_D = 0.5$, $T_B = 100$, and $L = 100$.

In addition to the conclusions we reach in the following sections regarding optimal values of T_B and T_D, it is essential that the interlayer spacing and lateral translation between layers be carefully chosen and precisely controlled. Fortunately, we do not expect restrictions of the form of Eqs. (7.8) and (7.9) to be a significant impediment to implementation of our proposed fabrication method. The parameters v_B, v'_B, v_D, and v'_D may readily be manipulated by changing the angle of incidence of the ion beam, the incidence angles of the deposition beams, and the fluxes of these three beams. Furthermore, we will demonstrate that the values of T_B and T_D which lead to good MBGs in our simulations may be selected from a wide range of values. Equations (7.8) and (7.9) are thus not

expected to represent a severe restriction on the range of acceptable parameter values. In Section 7.7 we demonstrate that there exist values for the angles and fluxes of the beams depositing materials B and D such that Eqs. (7.8) and (7.9) are satisfied for a special case. The special case considered in Section 7.7 is equivalent to the special case described in the previous paragraph, but with the additional condition that $\Delta l = 0$. The argument for the existence of deposition angles and fluxes which satisfy these criteria is shown to hold for any possible values of Δh, ion beam flux, ion beam incidence angle, T_D, and T_B.

We now seek to eliminate as many free parameters as possible from Eqs. (7.6) and (7.7). We cannot use a horizontal or vertical scale for stage B that is different than the scale for stage D, but we can use a different time scale. It is advantageous to use a different time scale for stages B and D because it serves to reduce the number of free parameters by one. We make the following substitutions:

$$\tilde{u} \equiv \frac{c_2}{\kappa} u, \tag{7.10}$$

$$\tilde{x} \equiv \sqrt{\frac{\kappa}{B}} x, \tag{7.11}$$

$$\tilde{t} \equiv \frac{\kappa^2}{B} t, \tag{7.12}$$

and

$$\tilde{t}' \equiv \frac{c_2}{\lambda} \tilde{t}. \tag{7.13}$$

Here $\tilde{t}$ is the rescaled time for stage B and $\tilde{t}'$ is the rescaled time for stage D. Suppressing the tildes, we have

$$u_{t'} = r_1 u_{xx} - \frac{1}{2} u_x^2 \tag{7.14}$$

for stage D and

$$u_t = -u_{xx} - u_{xxxx} + \frac{1}{2}u_x^2 + \frac{\gamma}{6}u_x^3 \tag{7.15}$$

for stage B. Here

$$r_1 = \frac{A_2 c_2}{\lambda \kappa} \tag{7.16}$$

and

$$\gamma = \frac{|c_3 \kappa^{\frac{3}{2}}|}{c_2^2 \sqrt{B}}. \tag{7.17}$$

Note that $\gamma > 0$, and that in order for the theory to be well posed, it is necessary that $r_1 > 0$.

Following the rescaling given by Eqs. (7.10)-(7.13), we are left with 6 quantities that characterize our system: Firstly, we must specify the scaled wave number K_0 and amplitude A_0 of the initial condition. These may be chosen during the fabrication of the templated surface, and may therefore be thought of as control parameters. The free parameter γ in Eq. (7.15) influences the success of our proposed method. As we showed in previous work,[211] γ must exceed a threshold value for bombardment of a templated surface to result in a sawtooth profile. We must also determine the influence of the free parameter r_1 in Eq. (7.14) on the proposed procedure. This parameter characterizes the rate at which the surface smoothes during deposition. Finally, we must consider the duration of stages D and B, T_D and T_B. While Eqs. (7.8) and (7.9) give restrictions on these parameters, we must also determine whether values of T_D and T_B which satisfy these conditions also produce layers which have a good BG profile. In the following two sections, we will use simulations to explore the influence of these six quantities on the efficacy of our proposed procedure to fabricate high quality MBGs.

7.4 One Dimensional Results

In this section we consider the special case in which the surface does not vary in the transverse direction y. We begin by discussing the method that we will use to evaluate the influence of the six simulation parameters on the quality of the MBGs produced. We introduce a quantitative measure of how similar the surface at time t_1 is to the surface at time t_2. We define our "Correlation Metric" $C(t_1,t_2)$ as follows:

1. Consider the surface $u(x,t)$ at two different times t_1 and t_2. $u(x,t_1)$ will be taken to be a well formed BG surface, and will be referred to as the "reference state". We will assume that $u(x,t)$ may be accurately represented by its values at N evenly spaced points along the x direction. The spacing between these points is $\Delta x \equiv L/N$, where L is the sample length. Periodic boundary conditions are imposed for all simulations considered here.

2. Define

$$\tilde{C}(j,t_1,t_2) \equiv \sum_{i=1}^{N} |u(i\Delta x,t_1) - u((i+j)\Delta x,t_2)|, \tag{7.18}$$

   where $i, j \in \mathbb{Z}$ and $0 \leq j < N$.

3. Obtain the correlation metric by setting $C(t_1,t_2)$ equal to the minimum value of $\left[\tilde{C}(j,t_1,t_2)\right]/N$, where j ranges from 1 to N.

We divide $\tilde{C}$ by N in the third step so that we have an intrinsic measure of the persistence of the surface profile which is well behaved in the limit that $N \to \infty$. We minimize $\tilde{C}(j,t_1,t_2)$ with respect to j so that surfaces which differ only by a phase shift have $C = 0$. In what follows, we will choose

t_1 to be a time at which a good BG surface profile has been obtained and use $C(t_1,t_2)$ to determine whether the surface has a similar profile at time $t_2 > t_1$.

One of the remarkable features of solutions to Eq. (7.15) is that once the surface has become terraced, to a good approximation the surface pattern simply translates with constant velocity. Thus, if the surface is in a well formed terraced state at time t_s, then $C(t_s,t)$ remains small for all $t > t_s$. The error in approximating the surface by an unchanging travelling wave stems from small amplitude ripples which form on the terraces. It has been shown[66] that the amplitude of these ripples scales as $1/\sqrt{\gamma}$, and so the accuracy of approximating the surface by a steadily propagating periodic state improves monotonically with increasing γ.

We now demonstrate that our proposed procedure can be effective in counteracting the undesirable smoothing of the surface brought about by deposition. We choose a particular initial condition and set of parameters and determine the effects of alternately propagating the surface according to Eqs. (7.14) and (7.15). Figures 7.3 and 7.4 display the results of one such simulation. The initial condition for these simulations was obtained by applying stage B to a sinusoidal template for a time $T_0 = 1000$. As seen in Fig. 7.3, the spacing between layers is very consistent, and there is no evidence of degradation in the surface profile as layers are added. Figure 7.4 shows that the value of $C(T_0 + t_B,t)$ spikes as smoothing occurs during stage D, but it quickly returns to a small value during stage B. Our proposed fabrication procedure produces a high quality MBG in this simulation. By contrast, Fig. 7.5 shows the results of a simulation with the same parameters as those used in Fig. 7.3, except that T_B was set to zero. Physically, this corresponds to depositing multiple layers of the same material with no ion assist. The contrast between Figs. 7.3 and 7.5 is stark - the BG profile rapidly attenuates if an ion beam is not employed to restore the terraced form. We therefore

have ample motivation for a more thorough investigation into the circumstances in which ion beam assisted deposition improves the quality of MBGs.

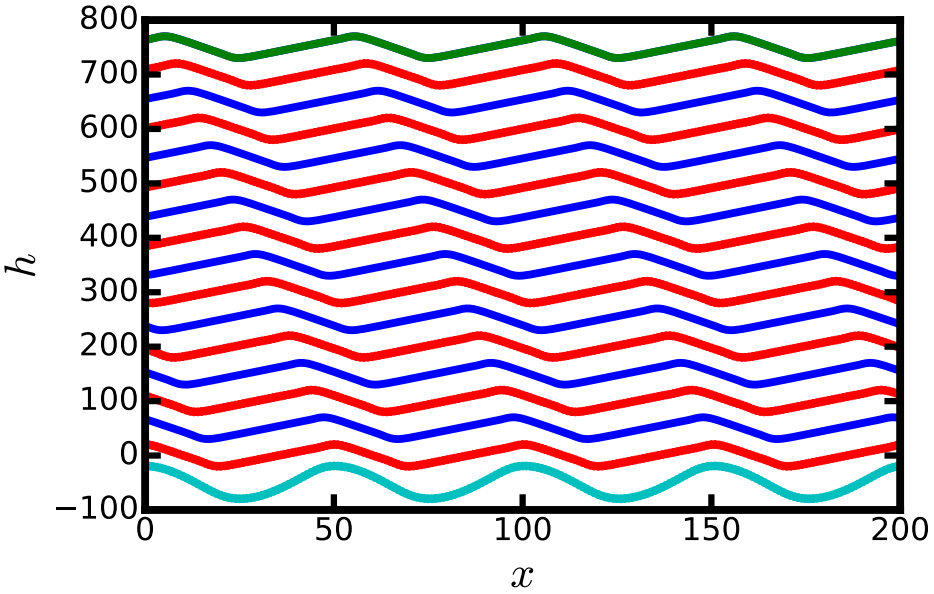

Fig. 7.3 A simulation of the multilayer fabrication procedure carried through the deposition of eight bilayers. The simulation parameters were the same as Fig. 7.2. The lowermost (cyan) line shows the templated initial condition. The red (blue) lines correspond to boundaries between materials B and D (D and B) moving from bottom to top. The uppermost (green) line indicates the vacuum-D interface.

To this end, we have performed extensive numerical simulations of Eqs. (7.14) and (7.15) for a broad range of parameters. To perform these simulations, we used the method of exponential time differencing proposed by Cox and Matthews[160] and improved by Kassam and Trefethen.[161] From these simulations, we will gain insight into the robustness and potential limitations of our MBG fabrication procedure, and how the values of the six simulation parameters influence the resulting multilayer. Throughout this work, we will use K_0 to refer to the integer number of oscillations a pattern has in the sample length L. Furthermore, for results presented in the remainder of this section, all simulations will be of stage B with a templated initial condition, followed by a simulation of stage D, followed by an additional simulation of stage B. The final time for these simulations

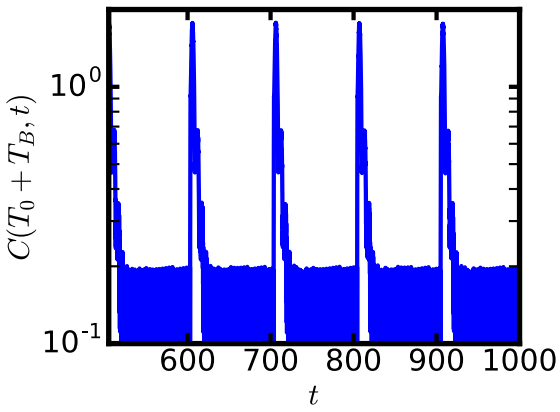

Fig. 7.4 A semi-log plot of $C(T_0+t_B,t)$ for the simulation shown in Fig. 7.3. The upward spikes occur during stage D, while the return to small values occurs during stage B.

will therefore be $t_f = 2T_B + T_D$. We will also use the end of the first stage B as the reference state for the metric C, since we expect that the surface will be a good BG profile at the end of the first stage B for appropriately chosen initial conditions and time T_B.

We begin by investigating the effect that the initial amplitude A_0 and scaled wave number K_0 have on the multilayer. We choose to examine these parameters together since they are the only two parameters which are determined during the formation of the templated surface. The values of A_0 and K_0 can be selected in an experiment, and thus represent parameters which can be tuned with relative ease. Figure 7.6 shows the value of $C(T_B,t)$ averaged over the final 10 time units of each simulation for a range of values of A_0 and K_0. Note that for all simulations considered here T_B is significantly larger than 10, and so this average is performed entirely over times close to the end of the second stage B. A low value of the average of C indicates that the surface at time $t_f = 2T_B + T_D$ is very similar to the surface at time $t = T_B$. Figure 7.6 strongly resembles the plots of efficiency as a function of A_0 and K_0 for BGs.[211] This plot indicates that the ideal values for K_0 for a MBG are the same as those for a BG. The influence of A_0 can be summarized simply: If A_0 is large enough

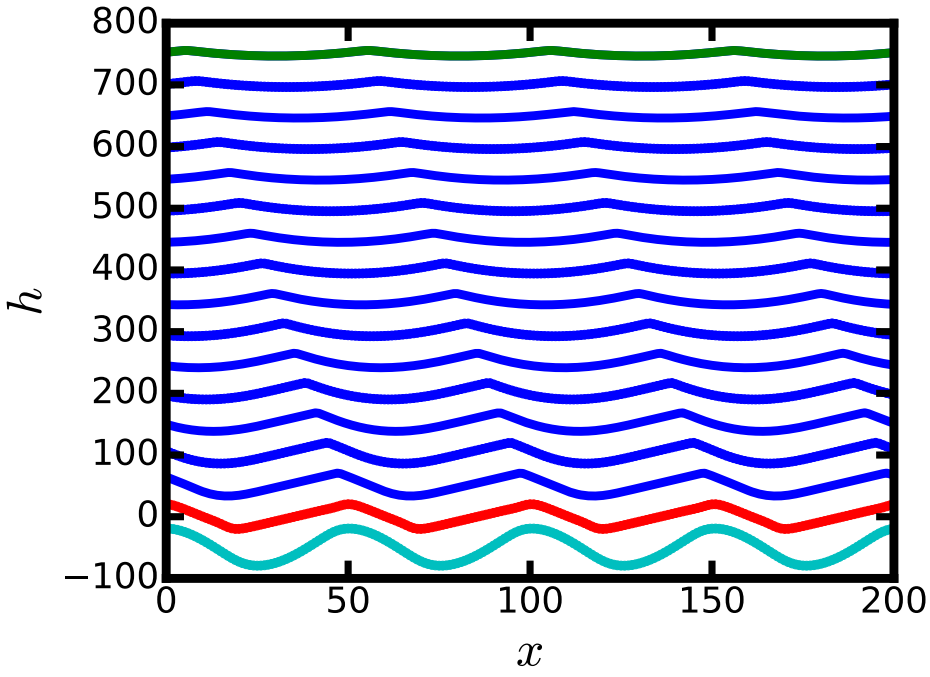

Fig. 7.5 A simulation of the multilayer deposition procedure carried through 16 layers. The simulation parameters were identical to those used in Fig. 7.3 except that after the first stage B, T_B was set to zero. The lowermost (cyan) line indicates the templated initial condition. The red (second to lowest) line shows the surface profile at the end of the first and only stage B. The multiple blue lines display the surface profile at the end of each subsequent stage D, except for the final stage D. The uppermost (green) line represents the vacuum-D interface.

that the surface has formed a good BG by the end of the first stage B, it is sufficiently large for the proposed MBG fabrication procedure to be implemented successfully.

The next area of interest is the combined influence of the scaled wave number of the MBG K_0 and the strength of the smoothing during stage D given by r_1. To this end, we simulated our proposed fabrication procedure for a range of values of these parameters. We chose to examine this pair of parameters to verify that values of K_0 which produced good MBGs in Fig. 7.6 continue to produce good MBGs for different deposition conditions. Figure 7.7 demonstrates that the persistence of the BG profile depends strongly on the wavelength of the pattern. In the bands of acceptable values of K_0, the degree of smoothing during the pure deposition stage D can be quite large and yet the

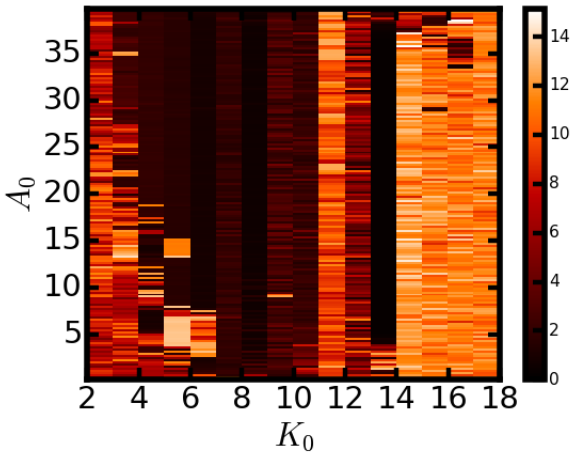

Fig. 7.6 The value of $C(T_B,t)$ averaged over the final 10 time units. The parameters were $\gamma = 1$, $r_1 = 1$, $T_D = 2$, $T_B = 200$, and $L = 200$. Black regions correspond to surfaces which are nearly identical to the initial BG apart from a phase shift. Each cell in this figure represents an average over 10 simulations with random initial noise of amplitude $10^{-4}A_0$ added to the pre-pattern. The final time T_f is $2T_B + T_D = 402$.

surface almost exactly returns to the original BG state at the end of the second stage B. However, for values of K_0 outside of these bands, a much smaller degree of smoothing is required for the surface to evolve into a state which does not resemble the initial BG profile. In particular, surface patterns with the wavenumber values in the interval $9 < K_0 < 12$ have a tendency to reform into a state with twice as many local maxima as the original state. Figure 7.8 shows an example of this behavior for a different set of parameters than those represented in Fig. 7.7.

We will now examine the limits of a very good BG state by sweeping through values of r_1 and T_D. We chose to examine this pair of parameters because together they completely characterize the surface smoothing which occurs during stage D. Figure 7.9 shows the value of $C(T_B,t)$ averaged over the final 10 time units for a range of values for r_1 and T_D. The large dark regions in Fig. 7.9 correspond to parameter sets which produce a high quality MBG. It is clear from this figure that r_1 and T_D can adopt a broad range of values without disrupting the proposed procedure.

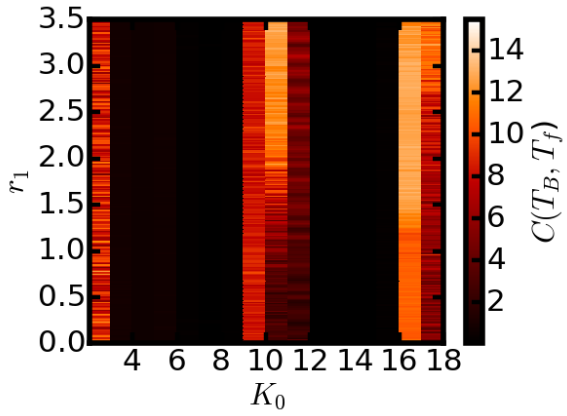

Fig. 7.7 The value of $C(T_B,t)$ averaged over the final 10 time units. The parameters were $\gamma = 1$, $A_0 = 30$, $T_B = 500$, $T_D = 2$, and $L = 200$. Black regions correspond to surfaces which are nearly identical to the initial BG. Each cell in this figure represents an average over 10 simulations with random initial noise of amplitude $10^{-4}A_0$ added to the pre-pattern. The final time T_f is $2T_B + T_D = 1002$.

It is worth noting that based on experimental results on the deposition of thin films, all but the very smallest values of T_D and r_1 included in Fig. 7.9 correspond to very thick deposited layers. In order to demonstrate this, we will compare the order of magnitude of the smoothing seen in our simulations with the smoothing observed in experiments. Since we are considering MBGs which operate in the soft X-ray or extreme ultraviolet regime, we expect that it will be necessary to deposit layers whose thickness is on the order of 10 nm. Experimental results directly relevant to our proposed procedure may be found in Ref. [21]. In that work, alternating layers of Mo and Si were deposited on a BG substrate. Comparing the results in that work to Fig. 7.5, we see that Fig. 7.5 depicts a case of exceptionally strong smoothing. The parameters used to generate Fig. 7.5 correspond to values in the very lower left-hand corner of Fig. 7.9.

Consider also the results of Ref. [208]. In that work, layers of ZrO_2 were deposited on a rough Ag surface. For deposited layers less than 30 nm thick, there was no statistically significant reduction in surface roughness. In Ref. [210], the smoothing of a sinusoidal surface profile during deposition was studied. In that work, a 10 nm thick layer of C deposited on a rippled Si surface was found to reduce

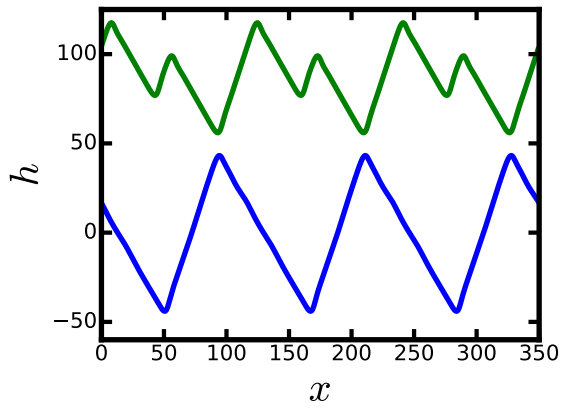

Fig. 7.8 A demonstration of the maxima doubling that results in the failure of our MBG procedure. The lower (blue) line shows the surface profile after one stage of simultaneous bombardment and deposition of material B. The upper (green) line shows the surface profile after a subsequent deposition of material D followed by another stage of concurrent bombardment and deposition of material B. The simulation parameters were $\gamma = 1$, $r_1 = 2.38$, $T_D = 22.5$, $T_B = 100$, $A_0 = 20$, $K_0 = 3$, and $L = 80$.

the root-mean-square surface width by only about 5%. By contrast, consider Fig. 7.5, for which $T_D = 0.5$ and $r_1 = 0.5$. In this case, the surface profile attenuates markedly after the deposition of a few layers. Based on these experimental results, we conclude that the majority of our simulations are in the regime in which smoothing is very strong.

We have performed numerical simulations with large values of r_1 and/or T_D both for the sake of completeness and to identify the circumstances in which our method fails. Figure 7.10 demonstrates the degree to which a smoothed surface is restored to a good BG profile as a result of stage B. The amplitude of the pattern is greatly reduced by stage D, and yet the surface still returns to a form very close to that produced by the initial stage of deposition and bombardment.

One somewhat surprising result of the analysis of the influence of r_1 and T_D is the band of inferior results for the range $T_D \simeq 13$ to $T_D \simeq 18$ seen in Fig. 7.9. For somewhat larger values of T_D, we see that the surface reproduces its initial state more quickly and accurately. Inspection of the inferior states reveals that the maxima doubling effect responsible for the band of intermediate K_0

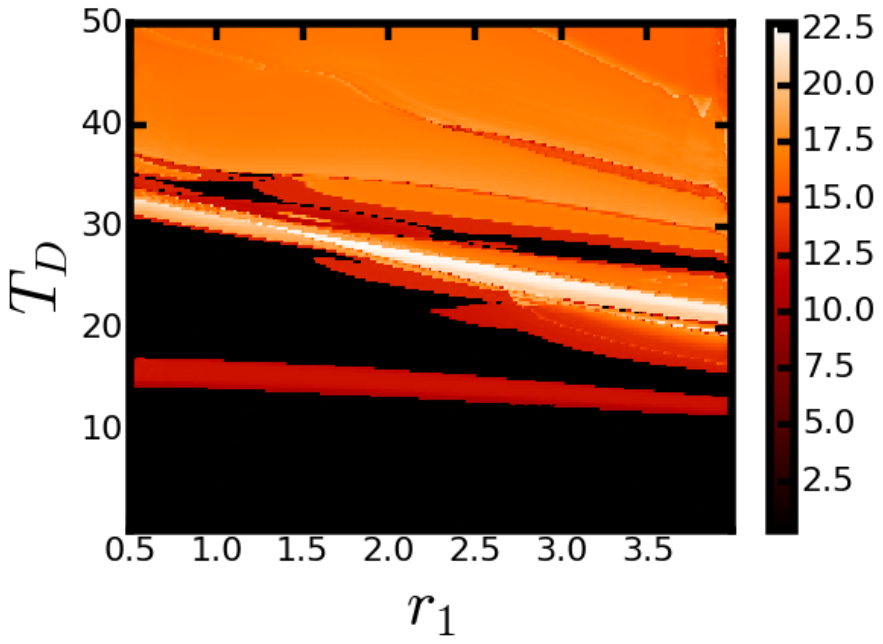

Fig. 7.9 The value of $C(T_B,t)$ averaged over the final 10 time units as a function of T_D and r_1. The parameters were $\gamma = 1$, $T_B = 100$, $A_0 = 20$, $K_0 = 3$, and $L = 160$. Black regions correspond to surfaces which are nearly identical to the initial BG.

values which produce poor quality MBGs in Fig. 7.7 is also responsible for these inferior states. Surface profiles at two times are shown for such an inferior MBG in Fig. 7.8. Surprisingly, in some cases it is better to increase T_D, the length of the deposition step D. Once again, however, these values of T_D and r_1 correspond to extreme smoothing of the surface, and it is very likely that any real experiment would correspond to values in the lower left corner of Fig. 7.9.

For all of the simulations presented so far, it has been the case that T_B significantly exceeds T_D. Although the duration of stages B and D in real time units depends on the rescaling given by Eqs. (7.12) and (7.13), there are two reasons why we might expect T_B to exceed T_D after restoring physical units. The first is that during stage B material is sputtered away during deposition. We have assumed that the relative fluxes of the deposition beam and the ion beam are such that a layer of

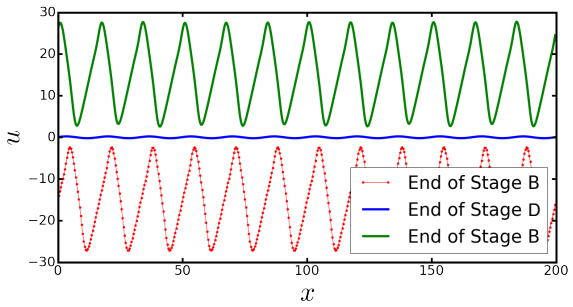

Fig. 7.10 Snapshots of a simulated surface just before the deposition step (lower red line), just after the deposition step (middle blue line), and after subsequent bombardment and deposition (upper green line). The simulation parameters were $\gamma = 1$, $r_1 = 1$, $T_D = 20$, $T_B = 100$, $A_0 = 30$, $K_0 = 12$, and $L = 200$.

material B is deposited. However, for equal thicknesses of layers B and D, the volume of material B deposited during stage B must exceed the volume of material D deposited during stage D. If the fluxes of the two deposition beams are equal, and the atomic volumes of materials B and D comparable, we would expect that stage D will take longer than stage B.

The second reason why $T_B > T_D$ in our simulations is that the surface profile is not degraded by a long stage B. Consider, for example, Fig. 7.4. Following stage D, the surface rapidly returns to a good BG profile. For the majority of time in stage B, the BG profile is not improved or degraded. The quality of the MBG is unaffected by choosing a value of T_B which is too long, but choosing one that is too short may give poor results.

In order to investigate the minimum value of T_B which may be used to successfully return a surface to a good BG profile following the smoothing that occurs during stage D, we have simulated a slightly different situation than we have considered so far. Previously we began with a sinusoidal profile, then simulated stage B for a time T_B, followed by stage D for a time T_D, followed by stage B for time T_B. We now begin with a sinusoidal profile, simulate stage B for a time $T_0 = 100$, followed

by a simulation of stage D for a time T_D, followed by a simulation of stage B for a time T_1. From these simulations we wish to extract the minimum value of T_1 which results in the surface becoming sufficiently similar to the BG profile obtained at time T_0. In this case we will define "sufficiently similar" to mean that $C(T_0, T_0 + T_D + T_1) \leq C^*$, where C^* is a threshold value and $T_1 > 0$. Previous work has revealed that, for a surface governed by Eq. (7.15), and with t_a and t_b chosen to be sufficiently large that these times are long after a well formed terraced state has developed, the average value of $C(t_a, t_b) \simeq (2.5\gamma)^{-\frac{1}{2}}$.[66] This is true provided $|t_a - t_b|$ is not very small. We will take this average value of C to be our threshold value C^*.

Figure 7.11 shows T_1^{min}, the minimum positive value of T_1 for which $C(T_0, T_0 + T_D + T_1) \leq C^*$ for a range of values for r_1 and T_D. This should be interpreted as the minimum value of T_B that could be used to successfully restore a BG profile which has been smoothed by deposition of material D. We have not investigated the minimum value of T_0 or its influence on T_1^{min}. The results which did not cross the threshold C^* before the simulation was terminated were assigned a value of $T_1^{min} = 100$, but would in fact never fall below the threshold. For these simulations, the surface formed into an approximate steady state that was not very similar to the initial BG profile, and thus $C(T_0, T_0 + T_D + T_1)$ never became small. These states suffered from the maxima doubling effect seen in Fig. 7.8.

7.5 Two-Dimensional Results

It is important to verify that the encouraging results found in the preceding sections continue to hold for surfaces which have a height h that varies in the transverse direction y [i.e. $h = h(x, y, t)$ and $u = u(x, y, t)$]. Extending our investigation to two dimensions increases the parameter space

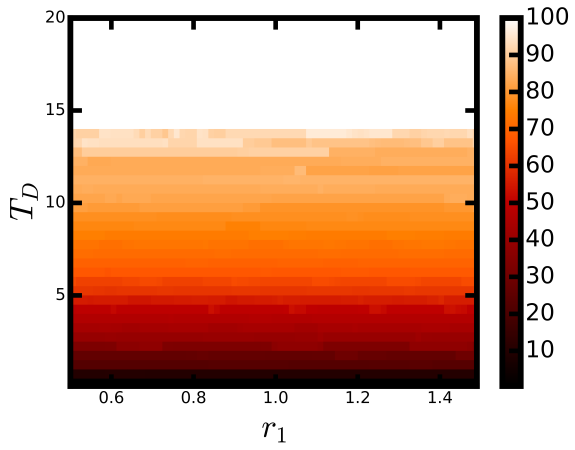

Fig. 7.11 A plot T_1^{min} vs r_1 and T_D. The simulation parameters were identical to those in Fig. 7.9. The white regions have been assigned a time of $T_1^{min} = 100$, but in fact have adopted approximately steady states that are not similar to the original BG profile, and for which $C(T_0, T_0 + T_D + T_1)$ never falls below the threshold C^* for $T_1 > 0$. For these simulations $T_0 = 100$.

substantially while making each simulation much more computationally intensive. The correlation metric $C(t_1,t_2)$ may be readily extended to a 2D surface on an $L \times L$ domain with N^2 evenly spaced gridpoints by defining

$$\tilde{C}_2(j,t_1,t_2) \equiv \sum_{m=1}^{N} \sum_{i=1}^{N} |u(i\Delta x, m\Delta x, t_1) - u((i+j)\Delta x, m\Delta x, t_2)|, \tag{7.19}$$

and setting $C_2(t_1,t_2)$ equal to the minimum value of $\left[\tilde{C}_2(j,t_1,t_2)\right]/N^2$, where j ranges from 1 to N.

A thorough investigation of the parameter space for the case of a BG formed by bombarding a pre-patterned surface was provided in Ref. [211], and we will not reproduce those results here. Instead, we focus on whether $C_2(T_B,t)$ behaves in a fashion similar to $C(T_B,t)$ for the case in which there is a linear instability in the transverse direction.

As mentioned previously, Eq. (7.3) results from extending the derivation of the KS equation to third order in the surface slope.[65] A natural extension of this equation to the case in which the surface varies in the y direction is therefore the anisotropic KS (aKS) equation with an added cubic

nonlinearity. The resulting anisotropic 3KS (a3KS) equation is given by

$$h_t = v_B + v'_B h_x + \kappa(-h_{xx} + A_y h_{yy}) - \beta\nabla^2\nabla^2 h + \frac{c_2}{2}\left(h_x^2 + \lambda_y h_y^2\right) + \frac{c_3}{6}h_x^3, \tag{7.20}$$

where v_B, v'_B, κ, A_y, β, c_2, λ_y, and c_3 are constants, and the subscripts on h denote partial derivatives. We shall take the extension of the KPZ equation (7.2) to 2+1 dimensions to be given by

$$h_t = v_D + v'_D h_x + A_2(h_{xx} + R'_1 h_{yy}) - \frac{\lambda}{2}(h_x^2 + R'_2 h_y^2), \tag{7.21}$$

where the constants R'_1 and R'_2 characterize the anisotropies in the linear and nonlinear terms, respectively. For the case of normal-incidence deposition, $R'_1 = R'_2 = 1$. We shall adopt the same rescalings and frames of reference used to obtain Eqs. (7.14) and (7.15). Additionally, we define

$$\tilde{y} \equiv \sqrt{\frac{\kappa}{\beta}}y, \tag{7.22}$$

and suppress the tilde. Equations (7.20) and (7.21) reduce to

$$u_t = -u_{xx} + A_y u_{yy} - \nabla^2\nabla^2 u + \frac{1}{2}\left(u_x^2 + \lambda_y u_y^2\right) + \frac{\gamma}{6}u_x^3 \tag{7.23}$$

and

$$u_t = r_1(u_{xx} + R'_1 u_{yy}) - u_x^2 - R'_2 u_y^2, \tag{7.24}$$

respectively. The task at hand is to confirm that the conclusions of the previous section hold for reasonable values of the new parameters λ_y, R'_1, R'_2, and A_y. There are some qualitative differences between the solutions to Eq. (7.15) and the solutions to Eq. (7.23) that further complicate this investigation. For low amplitude white noise initial conditions, solutions to Eq. (7.15) tend to form

an approximate steady state which propagates with little change. By contrast, solutions Eq. (7.23) may not spontaneously form such an approximate steady state, and under some circumstances they appear to coarsen indefinitely.[66]

Despite this qualitative difference between solutions, simulations of the proposed MBG fabrication procedure indicate that small variations in the transverse direction may not have a significant negative effect on the MBGs produced. For the case in which $A_y \gg 1$, the transverse direction is very stable, and terms proportional to h_y and its derivatives in Eqs. (7.20) and (7.21) are likely to be negligible. In this limit, the 1D analysis presented in the previous section is a very good approximation.

We therefore focus on the case in which the transverse direction is moderately stable or even unstable. Figures 7.12 and 7.13 show snapshots of the surface and the value of $C_2(T_B,t)$ respectively during the deposition of multiple layers for a case in which $A_y = -0.2$ (i.e., a moderate instability in the transverse direction). Just as in the 1D case, there is a spike in the value of $C_2(T_B,t)$ during the deposition stage, followed by a decay during the subsequent stage in which concurrent ion bombardment and deposition occurs. Furthermore, the value of $C_2(T_B,t)$ remains small until another deposition stage begins.

In Ref. [211], it was found that even for the case of an isotropic linear instability, high quality BGs could be produced if the time scale of transverse ripple formation was significantly longer than the time scale of terrace formation. For MBGs, however, we would like to be able to deposit a large number of layers without a significant deterioration of the pattern, and thus we cannot rely on such a time scale argument.

Numerical simulations such as those summarized in Fig. 7.13 indicate that the MBG fabrication procedure we have proposed can be successfully implemented even in the case that there is a

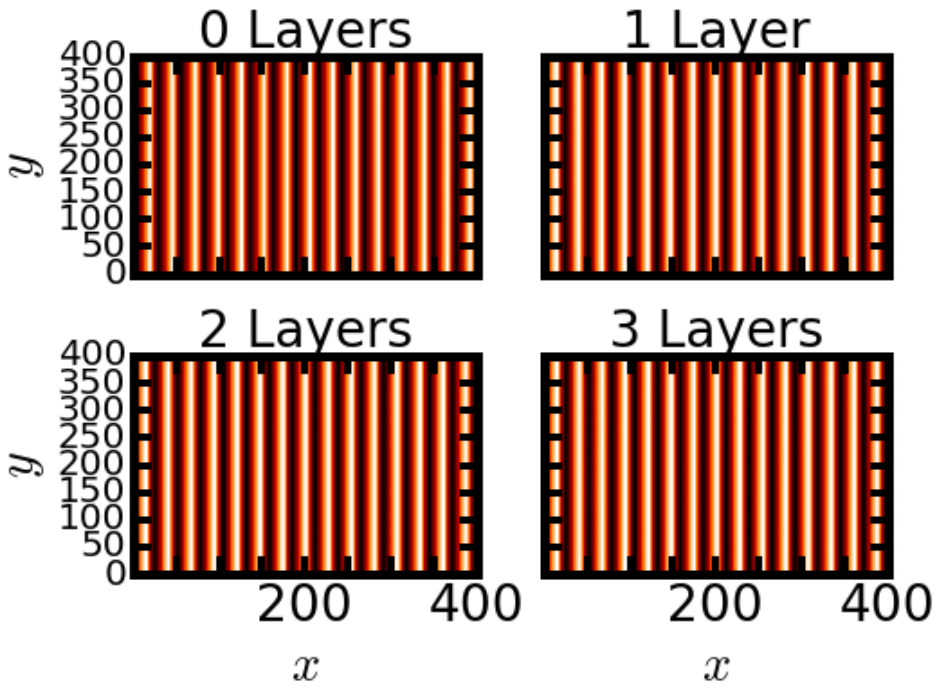

Fig. 7.12 Snapshots of the simulated surface during the MBG fabrication procedure. The simulation parameters were $A_2 = -0.2$, $\lambda_y = 1$, $\gamma = 1$, $r_1 = 1$, $T_B = 200$, $T_D = 5$, $A_0 = 10$, $K_0 = 15$, and $L = 400$. The labels "n layers" mean that the surface is shown after $n+1$ applications of stage B, and n applications of stage D. The vertical scale ranges from -20 to 20.

transverse instability, provided that this instability is not too strong compared to the instability in the x direction. Figure 7.14 shows the surface following the deposition of several layers for a case in which $A_2 = -0.5$. In this case, the transverse instability is strong enough to disrupt the formation of a highly ordered MBG, and our proposed fabrication method fails to produce a high quality MBG. Figure 7.15 shows the value of $C_2(T_B,t)$ for the simulation shown in Fig. 7.14. In contrast to Fig. 7.13, the average value of $C_2(T_B,t)$ grows due to the strong transverse instability, eventually reaching a state which is not at all similar to the surface at time T_B.

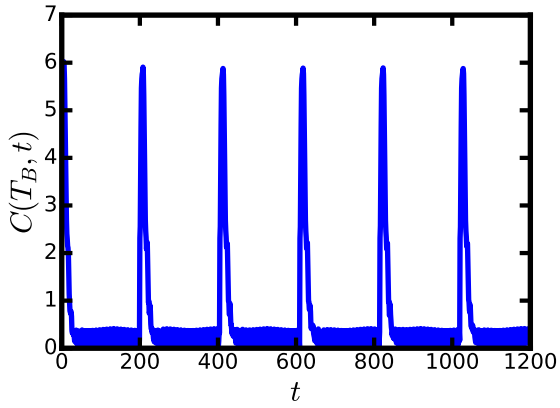

Fig. 7.13 The value of $C_2(T_B,t)$ over the course of several stages for the simulation depicted in Fig. 7.12. Notice that as in the one-dimensional case, $C_2(T_B,t)$ exhibits rapid growth during stage D, and subsequently returns to a small value during stage B.

7.6 Conclusion

A great deal of research has been done on improving the efficiency of multilayer blazed gratings (MBGs).[21,22,23,24] Several methods exist for creating a nearly ideal blazed grating (BG) profile, including methods which utilize bombardment with a broad ion beam.[198,4,5,6,7,8] The degradation of this profile during the deposition of a multilayer stack remains the primary obstacle to improving the efficiencies of MBGs, however.[21,22,23,24]

We have proposed and analyzed a method for producing MBGs whose surface profile does not significantly degrade in quality as additional layers are deposited. This procedure consists of two distinct phases, B and D, which are alternately and repeatedly applied. During phase B, a surface which has been prepatterned with a scaled wave number K_0 and amplitude A_0 is bombarded by an obliquely incident noble gas ion beam. Concurrently, a deposition beam of material B is also incident on the surface. During phase D, a beam of material D is incident on the surface. The durations of stages B and D are T_B and T_D, respectively. The primary results of this study are as follows:

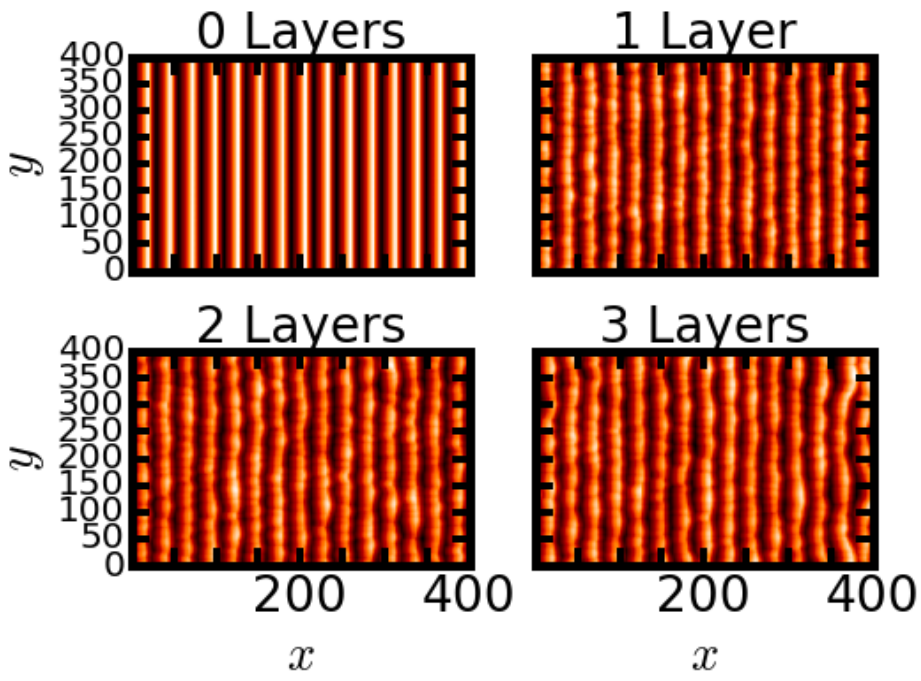

Fig. 7.14 Snapshots of the simulated surface during the MBG fabrication procedure. The simulation parameters were identical to those in Fig. 7.12 except that $A_2 = -0.5$. The stronger instability in the transverse direction leads the good BG pattern formed after the first stage B to degrade as additional layers are deposited. The vertical scale ranges from -20 to 20.

1. Employing bombardment with oblique-incidence broad ion beam during the deposition of thin layers on a BG profile has the potential to create a MBG whose surface profile does not degrade during the deposition of multiple layers.

2. The wavelength and amplitude of the template must be carefully chosen in order for a BG to form. Once a good BG has been formed, however, it is nearly always a sufficient starting point for fabricating a high quality MGB using our proposed method. For a detailed analysis of the A_0 and K_0 values which produce efficient BGs readers are directed to Ref. [211] (see, in particular, Figs. 3 and 4 of that paper). Figure 7.6 of the present work demonstrates which of these good initial BG states are suitable for our proposed MBG fabrication procedure.

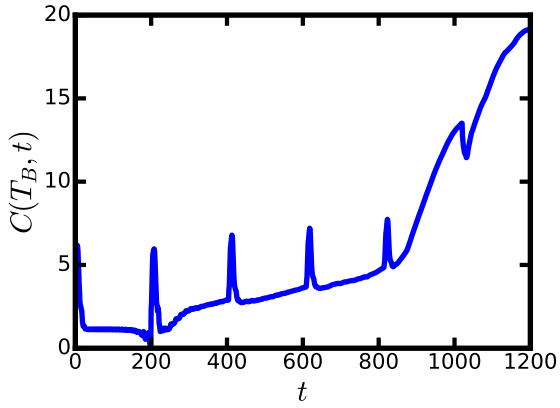

Fig. 7.15 A plot of $C_2(T_B,t)$ for the simulation shown in Fig. 7.14.

3. The surface may be smoothed to a considerable degree during stage D and yet it can still return to a good BG profile during stage B. As noted in the text, most of the parameter values characterizing stage D considered here correspond to experimental conditions which strongly favor smoothing. These extreme conditions were explored so as to identify the limits of our proposed procedure, but related experimental results[208,210,21] indicate that these limits will not be an impediment to the successful implementation of our proposed procedure.

4. To nearly perfectly recover the desired BG profile, the duration of stage B needs only to exceed a threshold value. This is provided that other conditions are chosen in such a way that Eqs. (7.8) and (7.9) are satisfied.

5. These results extend to a surface whose height varies in the transverse direction y, provided that the surface is stable or moderately unstable in the transverse direction.

Our numerical results strongly suggest that our proposed fabrication procedure may be used to circumvent the primary obstacle to good MBG fabrication in the SXR/EUV regime: the smoothing that occurs during thin film deposition. It is our hope that this work will inspire experimental work investigating the utility of ion-assisted deposition in the fabrication of MBGs.

7.7 Selection of Deposition Beam Parameters

To show how a judicious selection of the incidence angles and fluxes of the two deposition beams may be used to accommodate a particular interlayer spacing Δh, we will examine a particular case in detail. For this special case, we adopt the condition that the vertical thickness of layers of material A is the same as the vertical thickness of layers of material B. We also require that the horizontal translation between all layers be zero (i.e. $\Delta l = 0$). This special case is particularly relevant since it corresponds to the geometry of the MBGs produced in Refs. [21] and [22]. We will show that, for this special case, it is possible to choose values for the fluxes and incidence angles of the two deposition beams to accommodate an arbitrary choice of Δh, T_B, and T_D for any choice of ion beam incidence angle and flux.

Let θ_B, θ'_B, and θ'_D be the polar angle of the ion beam during stage B, the deposition beam during stage B, and the deposition beam during stage D, respectively. Let us assume that the rate with which material is deposited is proportional to the projection of the deposition flux onto the surface normal vector. This will be the case if the density of the film remains constant during deposition. For simplicity, we will suppress all time dependence on the surface curvature, since it does not contribute to propagation of the surface pattern. It follows from these assumptions that the contribution to h_t due to deposition may be written

$$\frac{h_t^{(deposition)}}{\sqrt{1+h_x^2}} = \Omega_i J_i \cos(\theta'_{i,local}), \tag{7.25}$$

where Ω_i is the atomic volume of species i, J_i is the flux of species i, $\theta'_{i,local}$ is the angle between the deposition beam of species i and the local surface normal, and $i = D, B$. Similarly, we assume

that the rate at which material is removed by the ion beam is proportional to the sputter yield $Y(\theta)$ evaluated at the local angle of ion beam incidence θ_{local}. Thus

$$\frac{h_t^{(erosion)}}{\sqrt{1+h_x^2}} = -\Omega_B J_{ion} Y(\theta_{local}) \cos(\theta_{local}), \tag{7.26}$$

where J_{ion} is the flux of the ion beam. The EOM for stage B is

$$h_t = h_t^{(deposition)} + h_t^{(ion)}, \tag{7.27}$$

with $i = \mathrm{B}$. The EOM for stage D is simply

$$h_t = h_t^{(deposition)} \tag{7.28}$$

with $i = \mathrm{D}$.

By expanding Eqs. (7.27) and (7.28) to first order in h_x, we obtain the following expressions for v_B, v'_B, v_D, and v'_D :

$$v_B = \Omega_B J_B \cos(\theta'_B) - \Omega_B J_{ion} Y(\theta_B) \cos(\theta_B), \tag{7.29}$$

$$v_D = \Omega_D J_D \cos(\theta'_D), \tag{7.30}$$

$$v'_B = -\Omega_B J_B \sin(\theta'_B) - \Omega_B J_{ion} \frac{\partial}{\partial \theta} \left[Y(\theta) \cos(\theta) \right] \Big|_{\theta_B}, \tag{7.31}$$

and

$$v'_D = -\Omega_D J_D \sin(\theta'_D). \tag{7.32}$$

Since we have assumed $\Delta l = 0$, we immediately conclude that we must have

$$v'_D = v'_B = 0. \tag{7.33}$$

Hence $\theta'_D = 0$ and

$$J_B \sin(\theta'_B) = -J_{ion} \frac{\partial}{\partial \theta} \left[Y(\theta) \cos(\theta) \right] \Big|_{\theta_B}. \tag{7.34}$$

Equation (7.8) yields

$$\Delta h = T_B \left[\Omega_B J_B \cos(\theta'_B) - \Omega_B J_{ion} Y(\theta_B) \cos(\theta_B) \right], \tag{7.35}$$

and

$$\Delta h = T_D \Omega_D J_D. \tag{7.36}$$

Equation (7.36) gives simple relationship between T_D and J_D. Because we have chosen $\theta'_D = 0$, we simply deposit long enough to get a layer of the desired thickness.

We are now left with the task of choosing values for J_B and θ'_B in such a way that Eqs. (7.34) and (7.35) are satisfied. It is very likely that we would be required to choose a value of θ_B within a particular range, so that the surface spontaneously forms terraces. However, for any value of θ_B, we may define

$$a_0 \equiv Y(\theta_B) \cos(\theta_B) \tag{7.37}$$

and

$$a_1 \equiv \frac{\partial}{\partial \theta} \left[Y(\theta) \cos(\theta) \right] \Big|_{\theta_B}. \tag{7.38}$$

Given arbitrary positive values for T_B, J_{ion}, and Δh, we may solve Eqs. (7.34) and (7.35) for the values of θ_B' and J_B. Assuming $a_0 a_1 \neq 0$, these are given by

$$\tan(\theta_B') = -\frac{J_{ion} a_1}{\frac{\Delta h}{T_B \Omega_B} + a_0 J_{ion}} \tag{7.39}$$

and

$$J_B = -\frac{J_{ion} a_1}{\sin(\theta_B')}. \tag{7.40}$$

Every term in the denominator of Eq. (7.39) is positive, and so θ_B' and a_1 have opposite signs. This implies that Eq. (7.40) always gives a positive value of J_B, as required.

This solution is presented as a demonstration of the flexibility of our proposed fabrication procedure. The deposition angles and fluxes are expected to be relatively easy to adjust in an experiment, and have been shown here to accommodate arbitrary positive values of Δh, J_{ion}, T_D, and T_B, as well as an arbitrary value of θ_B. It will therefore always be possible to choose the deposition beams so that Eqs. (7.8) and (7.9) are satisfied for the special case in which $\Delta l = 0$.

CHAPTER 8

CONCLUSION

This thesis represents an account of the original contributions to the scientific literature I have made during my time at Colorado State University. In collaboration with my advisor Mark Bradley, we developed our own formalism for using the information of a single ion impact crater to make predictions for the surface evolution as a whole. We furthermore demonstrated that the previous attempts to develop such a formalism were deeply flawed and contradicted earlier work.

We examined the case in which a binary material is bombarded by a broad ion beam while the sample is simultaneously rotating azimuthally. While limited to the early time regime, this work made some unexpected and interesting predictions. Under certain conditions, the wavelength of the pattern changes discontinuously through a continuous variation of the rotation frequency. These results were shown to hold qualitatively for continuous azimuthal rotation, and were placed in the appropriate mathematical context.

We also examined the case in which an elemental sample was bombarded with an ion beam while periodically the polar angle of ion beam incidence was periodically varied. We demonstrated with numerical simulations that this can suppress the spatiotemporal chaos and produce ripple patterns which are nearly perfectly periodic and stable in the long time limit. Given that the equation of motion considered is the most commonly adopted model of ion bombardment, this work should be of great interest for experimentalists.

Finally, we proposed and analyzed a new method for manufacturing blazed gratings using ion bombardment. We demonstrated evidence that bombardment of a pre-patterned surface at a high angle of incidence could be used to fabricate a blazed grating with high efficiency. We then extended this method to the case of multilayer blazed gratings. We demonstrated that ion bombardment during the deposition of the multilayer stack could be used to counteract the undesirable smoothing that has been seen to degrade the surface profile. This proposed procedure is currently being implemented in collaboration with Professor Carmen Menoni and her students.

BIBLIOGRAPHY

[1] M. Körner, K. Lenz, M. O. Liedke, T. Strache, A. Mücklich, A. Keller, S. Facsko, and J. Fassbender. Interlayer exchange coupling of fe/cr/fe thin films on rippled substrates. *Physical Review B*, 80(21):214401, 2009.

[2] L. Persechini, M. Ranjan, F. Grossmann, S. Facsko, and J. F. McGilp. The linear and nonlinear optical response of native-oxide covered rippled si templates with nanoscale periodicity. *physica status solidi (b)*, 249(6):1173–1177, 2012.

[3] Yoshinobu Aoyagi and Susumu Namba. Blazed ion-etched holographic gratings. *Journal of Modern Optics*, 23(9):701–707, 1976.

[4] Yoshinobu Aoyagi, Kazuo Sano, and Susumu Namba. High-spectroscopic qualities in blazed ion-etched holographic gratings. *Opt. Commun.*, 29(3):253–255, 1981.

[5] S. Somekh and H. C. Casey. Dry processing of high resolution and high aspect ratio structures in gaas-alxga 1- xas for integrated optics. *Appl. Optics*, 16(1):126–136, 1977.

[6] Xiangdong Xu, Yilin Hong, and Shaojun Fu. Vuv and soft x-ray diffraction grating fabrication by holographic ion beam etching. In *Photonics Asia 2004*, pages 165–175. International Society for Optics and Photonics, 2005.

[7] Minghui Chen, Quan Liu, and Jianhong Wu. A method of fabricating blazed grating by homogenous grating mask. In *International Conference on Optical Instruments and Technology (OIT2011)*, pages 820213–820213. International Society for Optics and Photonics, 2011.

[8] Quan Liu, Jianhong Wu, and Minghui Chen. Fabrication of blazed grating by native substrate grating mask. *Opt. Eng.*, 52(9):091706, 2 2013.

[9] Adrian Keller, Luca Peverini, Jörg Grenzer, György J. Kovacs, Arndt Mücklich, and Stefan Facsko. Polycrystalline ni thin films on nanopatterned si substrates: From highly conformal to nonconformal anisotropic growth. *Physical Review B*, 84(3):035423, 2011.

[10] Folarin Erogbogbo, Ken-Tye T. Yong, Indrajit Roy, Gaixia Xu, Paras N. Prasad, and Mark T. Swihart. Biocompatible luminescent silicon quantum dots for imaging of cancer cells. *ACS Nano*, 2(5):873–8, 5 2008.

[11] Francesca Granone, V. Mussi, A. Toma, S. Orlanducci, M. L. Terranova, C. Boragno, F. Buatier de Mongeot, and U. Valbusa. Ion sputtered surfaces as templates for carbon nanotubes alignment and deformation. *Nuclear Instruments and Methods in Physics Research Section B: Beam Interactions with Materials and Atoms*, 230(1):545–550, 2005.

[12] Scott A. Norris, Michael P. Brenner, and Michael J. Aziz. From crater functions to partial differential equations: a new approach to ion bombardment induced nonequilibrium pattern formation. *Journal of Physics: Condensed Matter*, 21(22):224017, 2009.

[13] R. Mark Bradley and J.M.E. Harper. Theory of ripple topography induced by ion bombardment. *J. Vac. Sci. Technol.*, 6(4):2390, 7 1988.

[14] Peter Sigmund. A mechanism of surface micro-roughening by ion bombardment. *J. Mat. Sci.*, 8(11):1545–1553, 1973.

[15] Anton Zalar and S. Hofmann. Influence of ion energy, incidence angle and surface roughness on depth resolution in aes sputter profiling of multilayer cr/ni thin films. *Nuclear Instruments and*

Methods in Physics Research Section B: Beam Interactions with Materials and Atoms, 18(1-6):655–658, 1986.

[16] Eun-Hee Cirlin, Robert E. Doty, John J. Vajo, and T. C. Hasenberg. Ion-induced topography, depth resolution, and ion yield during secondary ion mass spectrometry depth profiling of a gaas/algaas superlattice: Effects of sample rotation. *Journal of Vacuum Science & Technology A: Vacuum, Surfaces, and Films*, 9(3):1395, 5 1991.

[17] Eun-Hee . H. Cirlin, John J. Vajo, and T. C. Hasenberg. Limiting factors for secondary ion mass spectrometry profiling. *Journal of Vacuum Science & Technology B*, 12(1):269–275, 1994.

[18] F. Frost. The role of sample rotation and oblique ion incidence on quantum-dot formation by ion sputtering. *Applied Physics A*, 74(1):131–133, 2002.

[19] F. Frost, B. Ziberi, A. Schindler, and B. Rauschenbach. Surface engineering with ion beams: from self-organized nanostructures to ultra-smooth surfaces. *Appl. Phys. A*, 91(4):551–559, 4 2008.

[20] Christopher A. Palmer, Erwin G. Loewen, and R. G. L. Thermo. *Diffraction grating handbook*. Newport Corporation Springfield, Ohio, USA, 2005.

[21] Dmitriy L. Voronov, Minseung Ahn, Erik H. Anderson, Rossana Cambie, C.-H. Chang, Eric M. Gullikson, Ralf K. Heilmann, Farhad Salmassi, Mark L. Schattenburg, and Tony Warwick. High-efficiency 5000 lines/mm multilayer-coated blazed grating for extreme ultraviolet wavelengths. *Opt. Lett.*, 35(15):2615–2617, 2010.

[22] D. L. Voronov, P. Gawlitza, R. Cambie, S. Dhuey, E. M. Gullikson, T. Warwick, S. Braun, V. V. Yashchuk, and H. A. Padmore. Conformal growth of mo/si multilayers on grating substrates using collimated ion beam sputtering. *J. Appl. Phys.*, 111(9):093521, 2012.

[23] D. L. Voronov, E. H. Anderson, E. M. Gullikson, Farhad Salmassi, Tony Warwick, V. V. Yashchuk, and H. A. Padmore. Control of surface mobility for conformal deposition of mo–si multilayers on saw-tooth substrates. *Appl. Surf. Sci.*, 284:575–580, 2013.

[24] D. L. Voronov, E. M. Gullikson, F. Salmassi, T. Warwick, and H. A. Padmore. Enhancement of diffraction efficiency via higher-order operation of a multilayer blazed grating. *Opt. Lett.*, 39(11):3157–3160, 2014.

[25] R. L. Cunningham, P. Haymann, C. Lecomte, W. J. Moore, and J. J. Trillat. Etching of surfaces with 8-kev argon ions. *J. Appl. Phys.*, 31(5):839, 1960.

[26] M. Navez, D. Chaperot, and C. Sella. Microscopie electronique-etude de lattaque du verre par bombardement ionique. *Comptes Rendus Hebdomadaires Des Seances De L Academie Des Sciences*, 254(2):240, 1962.

[27] Marc Teichmann, Jan Lorbeer, Frank Frost, and Bernd Rauschenbach. Ripple coarsening on ion beam-eroded surfaces. *Nanoscale Res Lett*, 9(1):439, 2014.

[28] Gozde Ozaydin, Ahmet S. Özcan, Yiyi Wang, Karl F. Ludwig, Hua Zhou, Randall L. Headrick, and D. Peter Siddons. Real-time x-ray studies of mo-seeded si nanodot formation during ion bombardment. *Appl. Phys. Lett.*, 87(16):163104, 2005.

[29] B. Ziberi, F. Frost, M. Tartz, H. Neumann, and B. Rauschenbach. Importance of ion beam parameters on self-organized pattern formation on semiconductor surfaces by ion beam erosion. *Thin Solid Films*, 459(1):106–110, 2004.

[30] Charbel S. Madi and Michael J. Aziz. Multiple scattering causes the low energylow angle constant wavelength topographical instability of argon ion bombarded silicon surfaces. *Applied Surface Science*, 258(9):4112–4115, 2 2012.

[31] Kun Zhang, Marc Brötzmann, and Hans Hofsäss. Surfactant-driven self-organized surface patterns by ion beam erosion. *New Journal of Physics*, 13(1):013033, 1 2011.

[32] Jing Zhou, Stefan Facsko, Ming Lu, and Wolfhard Möller. Nanopatterning of si surfaces by normal incident ion erosion: Influence of iron incorporation on surface morphology evolution. *J. Appl. Phys.*, 109(10):104315, 2011.

[33] Sven Macko, Frank Frost, Martin Engler, Dietmar Hirsch, Thomas Höche, Jörg Grenzer, and Thomas Michely. Phenomenology of iron-assisted ion beam pattern formation on si(001). *New Journal of Physics*, 13(7):073017, 7 2011.

[34] J. A. Sánchez-García, L. Vázquez, R. Gago, A. Redondo-Cubero, J. M. Albella, and Zs Czigány. Tuning the surface morphology in self-organized ion beam nanopatterning of si(001) via metal incorporation: from holes to dots. *Nanotechnology*, 19(35):355306, 9 2008.

[35] A. Redondo-Cubero, R. Gago, F. J. Palomares, A. Mücklich, M. Vinnichenko, and L. Vázquez. Nanopatterning dynamics on si(100) during oblique 40-kev ar + erosion with metal codeposition: Morphological and compositional correlation. *Phys. Rev. B*, 86(8), 8 2012.

[36] Charbel S. Madi, Benny Davidovitch, H. Bola George, Scott A. Norris, Michael P. Brenner, and Michael J. Aziz. Multiple bifurcation types and the linear dynamics of ion sputtered surfaces. *Phys Rev Lett*, 101(24):246102, 12 2008.

[37] Charbel S. Madi, Benny Davidovitch, H. Bola George, Scott A. Norris, Michael P. Brenner, and Michael J. Aziz. Erratum: Multiple bifurcation types and the linear dynamics of ion sputtered surfaces [phys. rev. lett. 101 , 246102 (2008)]. *Phys. Rev. Lett.*, 107(4), 7 2011.

[38] K. Zhang, H. Hofsäss, F. Rotter, M. Uhrmacher, C. Ronning, and J. Krauser. Morphology of si surfaces sputter-eroded by low-energy xe-ions at glancing incident angle. *Surface and Coatings Technology*, 203(17-18):2395–2398, 6 2009.

[39] Adrian Keller and Stefan Facsko. Ion-induced nanoscale ripple patterns on si surfaces: Theory and experiment. *Materials*, 3(10):4811–4841, 10 2010.

[40] M. Castro, R. Gago, L. Vázquez, J. Muñoz García, and R. Cuerno. Stress-induced solid flow drives surface nanopatterning of silicon by ion-beam irradiation. *Phys. Rev. B*, 86(21), 12 2012.

[41] G. Carter and V. Vishnyakov. Roughening and ripple instabilities on ion-bombarded si. *Phys. Rev. B*, 54(24):17647, 1996.

[42] Charbel S. Madi, H. Bola George, and Michael J. Aziz. Linear stability and instability patterns in ion-sputtered silicon. *J Phys Condens Matter*, 21(22):224010, 6 2009.

[43] Javier Muñoz García, Raúl Gago, Luis Vázquez, José Angel Sánchez-García, and Rodolfo Cuerno. Observation and modeling of interrupted pattern coarsening: surface nanostructuring by ion erosion. *Phys Rev Lett*, 104(2):026101, 1 2010.

[44] F. Ludwig, C. R. Eddy, O. Malis, and R. L. Headrick. Si(100) surface morphology evolution during normal-incidence sputtering with 100500 ev ar[sup +] ions. *Appl. Phys. Lett.*, 81(15):2770, 2002.

[45] D. Carbone, A. Biermanns, B. Ziberi, F. Frost, O. Plantevin, U. Pietsch, and T. H. Metzger. Ion-induced nanopatterns on semiconductor surfaces investigated by grazing incidence x-ray scattering techniques. *J Phys Condens Matter*, 21(22):224007, 6 2009.

[46] Charbel S. Madi, Eitan Anzenberg, Karl F. Ludwig Jr, and Michael J. Aziz. Mass redistribution causes the structural richness of ion-irradiated surfaces. *Physical review letters*, 106(6):066101, 2011.

[47] Eitan Anzenberg, Charbel S. Madi, Michael J. Aziz, and Karl F. Ludwig Jr. Time-resolved measurements of nanoscale surface pattern formation kinetics in two dimensions on ion-irradiated si. *Phys. Rev. B*, 84(21), 12 2011.

[48] Tanmoy Basu and T. Som. Temporal evolution of ripple pattern on silicon surface: An ion induced solid flow approach. *Applied Surface Science*, 310:142–146, 8 2014.

[49] Adrian Keller, Steven Rossbach, Stefan Facsko, and Wolfhard Möller. Simultaneous formation of two ripple modes on ion sputtered silicon. *Nanotechnology*, 19(13):135303, 4 2008.

[50] Adrian Keller, Rodolfo Cuerno, Stefan Facsko, and Wolfhard Möller. Anisotropic scaling of ripple morphologies on high-fluence sputtered silicon. *Phys. Rev. B*, 79(11), 3 2009.

[51] Tanmoy Basu, Jyoti Ranjan Mohanty, and T. Som. Unusual pattern formation on si(100) due to low energy ion bombardment. *Appl. Surf. Sci.*, 258(24):9944–9948, 10 2012.

[52] Tanmoy Basu, Debi Prasad Datta, and Tapobrata Som. Transition from ripples to faceted structures under low-energy argon ion bombardment of silicon: understanding the role of shadowing and sputtering. *Nanoscale Res. Lett.*, 8(1):289, 2013.

[53] W. Hauffe. Faceting mechanism in the sputtering process. *Physica Status Solidi. A*, 35(2):K93–K96, 1976.

[54] G. Carter, M. J. Nobes, F. Paton, J. S. Williams, and J. L. Whitton. Ion bombardment induced ripple topography on amorphous solids. *Radiat. Eff.*, 33(2):65–73, 1977.

[55] F. Flamm, F. Frost, and D. Hirsch. Evolution of surface topography of fused silica by ion beam sputtering. *Appl. Surf. Sci.*, 179:96–101, 7 2001.

[56] P. Karmakar and D. Ghose. Ion beam sputtering induced ripple formation in thin metal films. *Surf. Sci.*, 554(2):L101–L106, 2004.

[57] Debi Prasad Datta and Tapas Kumar Chini. Atomic force microscopy study of 60 kev ar-ion-induced ripple patterns on si(100). *Phys. Rev. B*, 69(23), 6 2004.

[58] D. P. Adams, T. M. Mayer, M. J. Vasile, and K. Archuleta. Effects of evolving surface morphology on yield during focused ion beam milling of carbon. *Appl. Surf. Sci.*, 252(6):2432–2444, 2006.

[59] P. Mishra and D. Ghose. Effect of initial target surface roughness on the evolution of ripple topography induced by oxygen sputtering of al films. *J. Appl. Phys.*, 105(1):014304, 2009.

[60] Qiangmin Wei, Jie Lian, Lynn A. Boatner, L. M. Wang, and Rodney C. Ewing. Propagation of ripples on pyrochlore induced by ion beam bombardment. *Phys. Rev. B*, 80(8):085413, 2009.

[61] Tapas Kumar Chini, Debi Prasad Datta, and Satya Ranjan Bhattacharyya. Ripple formation on silicon by medium energy ion bombardment. *J. Phys. Condens. Matt.*, 21(22):224004, 6 2009.

[62] J. Völlner, B. Ziberi, F. Frost, and B. Rauschenbach. Topography evolution mechanism on fused silica during low-energy ion beam sputtering. *J. Appl. Phys.*, 109(4):043501–043501, 2011.

[63] A. Metya, D. Ghose, S. A. Mollick, and A. Majumdar. Nanopatterning of mica surface under low energy ion beam sputtering. *J. Appl. Phys.*, 111(7):074306, 2012.

[64] Martin Engler, Sven Macko, Frank Frost, and Thomas Michely. Evolution of ion beam induced patterns on si(001). *Phys. Rev. B*, 89(24):245412, 6 2014.

[65] Daniel A. Pearson and R. Mark Bradley. Theory of terraced topographies produced by oblique-incidence ion bombardment of solid surfaces. *J. Phys.-Condens. Mat.*, 27(1):015010, 2015.

[66] Daniel A. Pearson, Matthew P. Harrison, and R. M. Bradley. A model of terraced topographies produced by ion beam sputtering. *in preparation*, 2017.

[67] J. Muñoz García, R. Gago, R. Cuerno, J. A. Sánchez-García, A. Redondo-Cubero, M. Castro, and L. Vázquez. Independence of interrupted coarsening on initial system order: ion-beam nanopatterning of amorphous versus crystalline silicon targets. *J Phys Condens Matter*, 24(37):375302, 9 2012.

[68] Javier Muñoz García, Mario Castro, and Rodolfo Cuerno. Nonlinear ripple dynamics on amorphous surfaces patterned by ion beam sputtering. *Phys Rev Lett*, 96(8):086101, 3 2006.

[69] Javier Muñoz García, Rodolfo Cuerno, and Mario Castro. Short-range stationary patterns and long-range disorder in an evolution equation for one-dimensional interfaces. *Phys Rev E Stat Nonlin Soft Matter Phys*, 74(5 Pt 1):050103, 11 2006.

[70] Hans Hofsäss, Kun Zhang, and Omar Bobes. Self-organized surface ripple pattern formation by ion implantation. *Journal of Applied Physics*, 120(13):135308, 10 2016.

[71] Monika Fritzsche, Arndt Muecklich, and Stefan Facsko. Nanohole pattern formation on germanium induced by focused ion beam and broad beam ga+ irradiation. *Applied Physics Letters*, 100(22):223108, 2012.

[72] L. Bischoff, K-H . H. Heinig, B. Schmidt, S. Facsko, and W. Pilz. Self-organization of ge nanopattern under erosion with heavy bi monomer and cluster ions. *Nuclear Instruments and Methods in Physics Research Section B: Beam Interactions with Materials and Atoms*, 272:198–201, 2012.

[73] S. Facsko. Formation of ordered nanoscale semiconductor dots by ion sputtering. *Science*, 285(5433):1551–1553, 9 1999.

[74] F. Frost, A. Schindler, and F. Bigl. Roughness evolution of ion sputtered rotating inp surfaces: pattern formation and scaling laws. *Physical review letters*, 85(19):4116, 2000.

[75] Raúl Gago, Luis Vázquez, Rodolfo Cuerno, Maŕa Varela, Carmen Ballesteros, and José Maŕa Albella. Production of ordered silicon nanocrystals by low-energy ion sputtering. *Appl. Phys. Lett.*, 78(21):3316, 2001.

[76] Wen-bin . B. Fan, Wei-qing . Q. Li, Le-jun . J. Qi, Hai-tong . T. Sun, Jia Luo, You-yuan . Y. Zhao, and Ming Lu. On the role of ion flux in nanostructuring by ion sputter erosion. *Nanotechnology*, 16(9):1526, 2005.

[77] B. Ziberi, F. Frost, M. Tartz, H. Neumann, and B. Rauschenbach. Ripple rotation, pattern transitions, and long range ordered dots on silicon by ion beam erosion. *Applied Physics Letters*, 92(6):063102, 2008.

[78] Alexandre Cuenat and Michael J. Aziz. Spontaneous pattern formation from focused and unfocused ion beam irradiation. In *MRS Proceedings*, volume 696, pages N2–8. Cambridge Univ Press, 2001.

[79] B. Ziberi, M. Cornejo, F. Frost, and B. Rauschenbach. Highly ordered nanopatterns on ge and si surfaces by ion beam sputtering. *J Phys Condens Matter*, 21(22):224003, 6 2009.

[80] Sven Macko, Frank Frost, Bashkim Ziberi, Daniel F. Förster, and Thomas Michely. Is kev ion-induced pattern formation on si(001) caused by metal impurities? *Nanotechnology*, 21(8):85301, 2 2010.

[81] Hans Hofsäss and Kun Zhang. Surfactant sputtering. *Applied Physics A*, 92(3):517–524, 2008.

[82] H. Hofsäss, K. Zhang, A. Pape, O. Bobes, and M. Brötzmann. The role of phase separation for self-organized surface pattern formation by ion beam erosion and metal atom co-deposition. *Applied Physics A*, 111(2):653–664, 2013.

[83] Martin Engler, Frank Frost, Sven Müller, Sven Macko, Moritz Will, René Feder, Daniel Spemann, René Hübner, Stefan Facsko, and Thomas Michely. Silicide induced ion beam patterning of si(001). *Nanotechnology*, 25(11):115303, 3 2014.

[84] R. Gago, L. Vázquez, O. Plantevin, J. A. Sánchez-García, M. Varela, M. C. Ballesteros, J. M. Albella, and T. H. Metzger. Temperature influence on the production of nanodot patterns by ion beam sputtering of si (001). *Physical Review B*, 73(15):155414, 2006.

[85] Sven Macko, Jörg Grenzer, Frank Frost, Martin Engler, Dietmar Hirsch, Monika Fritzsche, Arndt Mücklich, and Thomas Michely. Iron-assisted ion beam patterning of si (001) in the crystalline regime. *New Journal of Physics*, 14(7):073003, 2012.

[86] Xin Ou, K-H Heinig, René Hübner, Jörg Grenzer, Xi Wang, Manfred Helm, Jürgen Fassbender, and Stefan Facsko. Faceted nanostructure arrays with extreme regularity by self-assembly of vacancies. *Nanoscale*, 7(45):18928–35, 12 2015.

[87] K. V. Sarathlal, Dileep Kumar, and Ajay Gupta. Growth study of co thin film on nanorippled si (100) substrate. *Applied Physics Letters*, 98(12):123111, 2011.

[88] C. Teichert. Self-organized semiconductor surfaces as templates for nanostructured magnetic thin films. *Applied Physics A*, 76(5):653–664, 2003.

[89] J. Fassbender, T. Strache, M. O. Liedke, D. Markó, S. Wintz, K. Lenz, A. Keller, S. Facsko, I. Mönch, and J. McCord. Introducing artificial length scales to tailor magnetic properties. *New Journal of Physics*, 11(12):125002, 2009.

[90] M. O. Liedke, M. Körner, K. Lenz, M. Fritzsche, M. Ranjan, A. Keller, E. Civzmar, S. A. Zvyagin, S. Facsko, and K. Potzger. Crossover in the surface anisotropy contributions of ferromagnetic films on rippled si surfaces. *Physical Review B*, 87(2):024424, 2013.

[91] Xin Ou, Reinhard Kögler, Xing Wei, Arndt Mücklich, Xi Wang, Wolfgang Skorupa, and Stefan Facsko. Fabrication of horizontal silicon nanowire arrays on insulator by ion irradiation. *AIP Advances*, 1(4):042174, 2011.

[92] Thomas WH Oates, Adrian Keller, Stefan Facsko, and Arndt Mücklich. Aligned silver nanoparticles on rippled silicon templates exhibiting anisotropic plasmon absorption. *Plasmonics*, 2(2):47–50, 2007.

[93] M. Ranjan, S. Facsko, M. Fritzsche, and S. Mukherjee. Plasmon resonance tuning in ag nanoparticles arrays grown on ripple patterned templates. *Microelectronic Engineering*, 102:44–47, 2013.

[94] Mukesh Ranjan and Stefan Facsko. Anisotropic surface enhanced raman scattering in nanoparticle and nanowire arrays. *Nanotechnology*, 23(48):485307, 2012.

[95] X. L. Ma, N. G. Shang, Q. Li, C. S. Lee, I. Bello, and S. T. Lee. Microstructural characterization of si cones fabricated by ar+-sputtering si/mo targets. *Journal of crystal growth*, 234(4):654–659, 2002.

[96] Y. S. Zou, Y. M. Chong, A. L. Ji, Y. Yang, Q. Ye, B. He, W. J. Zhang, I. Bello, and S. T. Lee. The fabrication of cubic boron nitride nanocone and nanopillar arrays via reactive ion etching. *Nanotechnology*, 20(15):155305, 4 2009.

[97] Ying Qiu, Hong-Chen . C. Hao, Jing Zhou, and Ming Lu. da close to unity and all-solar-spectrum absorption by ion-sputtering induced si nanocone arrays. *Optics express*, 20(20):22087–22094, 2012.

[98] Jing Zhou, Meret Hildebrandt, and Ming Lu. Self-organized antireflecting nano-cone arrays on si (100) induced by ion bombardment. *Journal of applied Physics*, 109(5):053513, 2011.

[99] C. Martella, D. Chiappe, P. Delli Veneri, L. V. Mercaldo, I. Usatii, and F. Buatier de Mongeot. Self-organized broadband light trapping in thin film amorphous silicon solar cells. *Nanotechnology*, 24(22):225201, 2013.

[100] Jana Sommerfeld, Jessica Richter, Raphael Niepelt, Stefanie Kosan, Thomas F. Keller, Klaus D. Jandt, and Carsten Ronning. Protein adsorption on nano-scaled, rippled tio2 and si surfaces. *Biointerphases*, 7(1-4):55, 12 2012.

[101] Elisa Mele, Francesca Di Benedetto, Roberto Cingolani, Dario Pisignano, Andrea Toma, Francesco Buatier de Mongeot, Renato Buzio, Corrado Boragno, Giuseppe Firpo, and Valentina Mussi. Nanostructuring polymers by soft lithography templates realized via ion sputtering. *Nanotechnology*, 16(11):2714, 2005.

[102] Rohit Karnik, Kenneth Castelino, Rong Fan, Peidong Yang, and Arun Majumdar. Effects of biological reactions and modifications on conductance of nanofluidic channels. *Nano Lett*, 5(9):1638–42, 9 2005.

[103] Christopher C. Striemer, Thomas R. Gaborski, James L. McGrath, and Philippe M. Fauchet. Charge- and size-based separation of macromolecules using ultrathin silicon membranes. *Nature*, 445(7129):749–53, 2 2007.

[104] Silva K. Theiss, M. J. Caturla, M. D. Johnson, J. Zhu, T. Lenosky, B. Sadigh, and T. Diaz De La Rubia. Atomic scale models of ion implantation and dopant diffusion in silicon. *Thin Solid Films*, 365(2):219–230, 2000.

[105] A. Mutzke, R. Schneider, W. Eckstein, and R. Dohmen. Sdtrimsp: Version 5.00. *IPP, Report,(12/8)*, 2011.

[106] Roger Smith. *Atomic and ion collisions in solids and at surfaces: theory, simulation and applications*. Cambridge University Press, 2005.

[107] C. A. Davis. A simple model for the formation of compressive stress in thin films by ion bombardment. *Thin solid films*, 226(1):30–34, 1993.

[108] H. Trinkaus and A. I. Ryazanov. Viscoelastic model for the plastic flow of amorphous solids under energetic ion bombardment. *Physical review letters*, 74(25):5072, 1995.

[109] H. Trinkaus. Dynamics of viscoelastic flow in ion tracks: origin of plastic deformation of amorphous materials. *Nuclear Instruments and Methods in Physics Research Section B: Beam Interactions with Materials and Atoms*, 146(1):204–216, 1998.

[110] S. G. Mayr, Y. Ashkenazy, K. Albe, and R. S. Averback. Mechanisms of radiation-induced viscous flow: role of point defects. *Phys Rev Lett*, 90(5):055505, 2 2003.

[111] B. Abendroth, H. U. Jager, W. Moller, and M. Bilek. Binary-collision modeling of ion-induced stress relaxation in cubic bn and amorphous c thin films. *Applied physics letters*, 90(18):181910, 2007.

[112] Yudi Rosandi and Herbert M. Urbassek. Glancing ion incidence on si (100): Influence of surface reconstruction on ion subsurface channeling. *Physical Review B*, 85(15):155430, 2012.

[113] Hans Hofsäss and R. Mark Bradley. Tests of the modified sigmund model of ion sputtering using monte carlo simulations. *Journal of Applied Physics*, 117(17):174310, 2015.

[114] Gerhard Hobler, R. Mark Bradley, and Herbert M. Urbassek. Probing the limitations of sigmund's model of spatially resolved sputtering using monte carlo simulations. *Physical Review B*, 93(20), 5 2016.

[115] R. Cuerno and A. . L. Barabási. Dynamic scaling of ion-sputtered surfaces. *Phys. Rev. Lett.*, 74(23):4746, 1995.

[116] Maxim A. Makeev and Albert-László Barabási. Ion-induced effective surface diffusion in ion sputtering. *Appl. Phys. Lett.*, 71(19):2800, 1997.

[117] Maxim A. Makeev, Rodolfo Cuerno, and Albert-Laszlo . L. Barabasi. Morphology of ion-sputtered surfaces. *Nuclear Instruments and Methods in Physics Research Section B: Beam Interactions with Materials and Atoms*, 197(3):185–227, 2002.

[118] Javier Muñoz García, Rodolfo Cuerno, and Mario Castro. Coupling of morphology to surface transport in ion-beam irradiated surfaces: oblique incidence. *Phys. Rev. B*, 78(20):205408, 2008.

[119] B. Kahng, H. Jeong, and A.-L. . Barabási. Quantum dot and hole formation in sputter erosion. *Appl. Phys. Lett.*, 78(6):805, 2001.

[120] Mario Castro, Rodolfo Cuerno, Luis Vázquez, and Raúl Gago. Self-organized ordering of nanostructures produced by ion-beam sputtering. *Phys Rev Lett*, 94(1):016102, 1 2005.

[121] Gozde Ozaydin, Ahmet S. Özcan, Yiyi Wang, Karl F. Ludwig, Hua Zhou, and Randall L. Headrick. Real-time x-ray studies of the growth of mo-seeded si nanodots by low-energy ion bombardment. *Nuclear Instruments and Methods in Physics Research Section B: Beam Interactions with Materials and Atoms*, 264(1):47–54, 11 2007.

[122] Adrian Keller, Matteo Nicoli, Stefan Facsko, and Rodolfo Cuerno. Dynamic effects induced by renormalization in anisotropic pattern forming systems. *Phys Rev E Stat Nonlin Soft Matter Phys*, 84(1 Pt 2):015202, 7 2011.

[123] G. Carter, V. Vishnyakov, and M. J. Nobes. Ripple topography development on ion bombarded si. *Nuclear Instruments and Methods in Physics Research Section B: Beam Interactions with Materials and Atoms*, 115(1):440–445, 1996.

[124] V. B. Shenoy, W. L. Chan, and E. Chason. Compositionally modulated ripples induced by sputtering of alloy surfaces. *Phys Rev Lett*, 98(25):256101, 6 2007.

[125] R. Mark Bradley. Exact linear dispersion relation for the sigmund model of ion sputtering. *Phys. Rev. B*, 84(7):075413, 2011.

[126] William W. Mullins. Theory of thermal grooving. *J. Appl. Phys.*, 28(3):333–339, 1957.

[127] C. C. Umbach, R. L. Headrick, and K. C. Chang. Spontaneous nanoscale corrugation of ion-eroded sio2: the role of ion-irradiation-enhanced viscous flow. *Phys. Rev. Lett.*, 87(24):246104, 12 2001.

[128] Michael Moseler, Peter Gumbsch, Cinzia Casiraghi, Andrea C. Ferrari, and John Robertson. The ultrasmoothness of diamond-like carbon surfaces. *Science*, 309(5740):1545–8, 9 2005.

[129] Benny Davidovitch, Michael J. Aziz, and Michael P. Brenner. On the stabilization of ion sputtered surfaces. *Physical Review B*, 76(20):205420, 2007.

[130] N. Kalyanasundaram, M. Ghazisaeidi, J. B. Freund, and H. T. Johnson. Single impact crater functions for ion bombardment of silicon. *Applied Physics Letters*, 92(13):131909, 2008.

[131] N. Kalyanasundaram, J. B. Freund, and H. T. Johnson. A multiscale crater function model for ion-induced pattern formation in silicon. *J Phys Condens Matter*, 21(22):224018, 6 2009.

[132] Scott A. Norris, Juha Samela, Laura Bukonte, Marie Backman, Flyura Djurabekova, Kai Nordlund, Charbel S. Madi, Michael P. Brenner, and Michael J. Aziz. Molecular dynamics of single-particle impacts predicts phase diagrams for large scale pattern formation. *Nat Commun*, 2:276, 2011.

[133] Scott A. Norris. Stability analysis of a viscoelastic model for ion-irradiated silicon. *Physical Review B*, 85(15):155325, 2012.

[134] Scott A. Norris. Stress-induced patterns in ion-irradiated silicon: model based on anisotropic plastic flow. *Physical Review B*, 86(23):235405, 2012.

[135] Mario Castro and Rodolfo Cuerno. Hydrodynamic approach to surface pattern formation by ion beams. *Applied Surface Science*, 258(9):4171–4178, 2012.

[136] Omar Bobes, Kun Zhang, and Hans Hofsäss. Ion beam induced surface patterns due to mass redistribution and curvature-dependent sputtering. *Phys. Rev. B*, 86(23), 12 2012.

[137] Zhangcan Yang, Michael Lively, and Jean Paul Allain. Atomistic simulation of ion beam patterning with crater functions. *Nuclear Instruments and Methods in Physics Research Section B: Beam Interactions with Materials and Atoms*, 2013.

[138] Wolfhard Möller. Tri3dyn–collisional computer simulation of the dynamic evolution of 3-dimensional nanostructures under ion irradiation. *Nuclear Instruments and Methods in Physics Research Section B: Beam Interactions with Materials and Atoms*, 322:23–33, 2014.

[139] Hans Hofsäss. Surface instability and pattern formation by ion-induced erosion and mass redistribution. *Applied Physics A*, 114(2):401–422, 2014.

[140] Hans Hofsäss, Omar Bobes, and Kun Zhang. Is sputtering relevant for ion-induced self-organized pattern formation? In *APPLICATION OF ACCELERATORS IN RESEARCH AND INDUSTRY: Twenty-Second International Conference*, volume 1525, pages 386–391. AIP Publishing, 2013.

[141] Yoshiki Kuramoto and Toshio Tsuzuki. Persistent propagation of concentration waves in dissipative media far from thermal equilibrium. *Prog. Theor. Phys.*, 55(2):356–369, 1976.

[142] G. I. Sivashinsky. On self-turbulization of a laminar flame. *Acta Astronaut.*, 6(5-6):569–591, 1979.

[143] H. Chen, Omar A. Urquidez, Stefan Ichim, L. Humberto Rodriquez, Michael P. Brenner, and Michael J. Aziz. Shocks in ion sputtering sharpen steep surface features. *Science*, 310(5746):294–7, 10 2005.

[144] Joy C. Perkinson, Michael J. Aziz, Michael P. Brenner, and Miranda Holmes-Cerfon. Designing steep, sharp patterns on uniformly ion-bombarded surfaces. *Proc Natl Acad Sci U S A*, 113(41):11425–11430, 10 2016.

[145] Miranda Holmes-Cerfon, Wei Zhou, Andrea L. Bertozzi, Michael P. Brenner, and Michael J. Aziz. Development of knife-edge ridges on ion-bombarded surfaces. *Applied Physics Letters*, 101(14):143109, 2012.

[146] Miranda Holmes-Cerfon, Michael J. Aziz, and Michael P. Brenner. Creating sharp features by colliding shocks on uniformly irradiated surfaces. *Physical Review B*, 85(16):165441, 2012.

[147] T. C. Kim, C-M . M. Ghim, H. J. Kim, D. H. Kim, D. Y. Noh, N. D. Kim, J. W. Chung, J. S. Yang, Y. J. Chang, and T. W. Noh. Kinetic roughening of ion-sputtered pd (001) surface: beyond the kuramoto-sivashinsky model. *Physical review letters*, 92(24):246104, 2004.

[148] Mario Castro and Rodolfo Cuerno. Comment on kinetic roughening of ion-sputtered pd (001) surface: beyond the kuramoto-sivashinsky model. *Physical review letters*, 94(13):139601; author reply 139602, 4 2005.

[149] Zoltán Csahók, Chaouqi Misbah, François Rioual, and Alexandre Valance. Dynamics of aeolian sand ripples. *The European Physical Journal E*, 3(1):71–86, 2000.

[150] R. Kree, T. Yasseri, and A. K. Hartmann. Surfactant sputtering: Theory of a new method of surface nanostructuring by ion beams. *Nuclear Instruments and Methods in Physics Research Section B: Beam Interactions with Materials and Atoms*, 267(8):1403–1406, 2009.

[151] R. Mark Bradley. Nanoscale patterns produced by ion erosion of a solid with codeposition of impurities: The crucial effect of compound formation. *Physical Review B*, 87(20):205408, 2013.

[152] Safiul Alam Mollick, Debabrata Ghose, Patrick D. Shipman, and R. Mark Bradley. Anomalous patterns and nearly defect-free ripples produced by bombarding silicon and germanium with a beam of gold ions. *Applied Physics Letters*, 104(4):043103, 2014.

[153] R. Mark Bradley. Producing ripple topographies by ion bombardment with codeposition of impurities: A curvature-dependent sputter yield is not required. *Physical Review B*, 85(11):115419, 2012.

[154] R. Mark Bradley and Kelly W. Mauser. Can the atomic yields oscillate during ion sputtering of an initially homogeneous multicomponent alloy? *Journal of Applied Physics*, 114(3):033506, 2013.

[155] R. Mark Bradley and Patrick D. Shipman. Spontaneous pattern formation induced by ion bombardment of binary compounds. *Phys Rev Lett*, 105(14):145501, 10 2010.

[156] Patrick D. Shipman and R. Mark Bradley. Theory of nanoscale pattern formation induced by normal-incidence ion bombardment of binary compounds. *Physical Review B*, 84(8):085420, 8 2011.

[157] R. Mark Bradley and Patrick D. Shipman. A surface layer of altered composition can play a key role in nanoscale pattern formation induced by ion bombardment. *Applied Surface Science*, 258(9):4161–4170, 2012.

[158] Francis C. Motta, Patrick D. Shipman, and R. Mark Bradley. Highly ordered nanoscale surface ripples produced by ion bombardment of binary compounds. *Journal of Physics D: Applied Physics*, 45(12):122001, 2012.

[159] Francis C. Motta, Patrick D. Shipman, and R. Mark Bradley. Theory of nanoscale pattern formation produced by oblique-incidence ion bombardment of binary compounds. *Phys. Rev. B*, 90(8), 8 2014.

[160] S. M. Cox and P. C. Matthews. Exponential time differencing for stiff systems. *J. Comput. Phys.*, 176(2):430–455, 2002.

[161] A. K. Kassam and Lloyd N. Trefethen. Fourth-order time-stepping for stiff pdes. *SIAM J. Sci. Comput.*, 26(4):1214–1233, 2005.

[162] M. Z. Hossain, K. Das, J. B. Freund, and H. T. Johnson. Ion impact crater asymmetry determines surface ripple orientation. *Applied Physics Letters*, 99(15):151913, 2011.

[163] Scott A. Norris, Juha Samela, Matias Vestberg, Kai Nordlund, and Michael J. Aziz. Crater functions for compound materials: A route to parameter estimation in coupled-pde models of ion bombardment. *Nuclear Instruments and Methods in Physics Research Section B: Beam Interactions with Materials and Atoms*, 318:245–252, 2014.

[164] Joy C. Perkinson, Eitan Anzenberg, Michael J. Aziz, and Karl F. Ludwig Jr. Model-independent test of the truncated crater function theory of surface morphology evolution during ion bombardment. *Physical Review B*, 89(11):115433, 2014.

[165] Maureen L. Nietiadi and Herbert M. Urbassek. Influence of local curvature on sputtering. *Applied Physics Letters*, 103(11):113108, 2013.

[166] M. Z. Hossain, J. B. Freund, and H. T. Johnson. Ion impact energy distribution and sputtering of si and ge. *Journal of Applied Physics*, 111(10):103513, 2012.

[167] Scott A. Norris. Ion-assisted phase separation in compound films: An alternate route to ordered nanostructures. *Journal of Applied Physics*, 114(20):204303, 2013.

[168] Javier Muñoz García, Luis Vázquez, Mario Castro, Raúl Gago, Andrés Redondo-Cubero, Ana Moreno-Barrado, and Rodolfo Cuerno. Self-organized nanopatterning of silicon surfaces by ion beam sputtering. *Mat. Sci. Eng. R-Reports*, 86:1–44, 12 2014.

[169] Jing Zhou and Ming Lu. Mechanism of fe impurity motivated ion-nanopatterning of si (100) surfaces. *Physical Review B*, 82(12):125404, 2010.

[170] R. Mark Bradley. Nanoscale compositional banding in binary thin films produced by ion-assisted deposition. *Journal of Applied Physics*, 114(22):224306, 2013.

[171] Anton Zalar. Auger electron spectroscopy depth profiling during sample rotation. *Surface and Interface Analysis*, 9(1):41–46, 1986.

[172] R. Mark Bradley and Eun-Hee . H. Cirlin. Theory of improved resolution in depth profiling with sample rotation. *Applied physics letters*, 68(26):3722–3724, 1996.

[173] R. Mark Bradley. Dynamic scaling of ion-sputtered rotating surfaces. *Physical Review E*, 54(6):6149, 12 1996.

[174] Taha Yasseri and Reiner Kree. A monte carlo study of surface sputtering by dual and rotated ion beams. *Nuclear Instruments and Methods in Physics Research Section B: Beam Interactions with Materials and Atoms*, 268(16):2496–2503, 8 2010.

[175] Debasree Chowdhury, Debabrata Ghose, and Biswarup Satpati. Production of ordered and pure si nanodots at grazing ion beam sputtering under concurrent substrate rotation. *Materials Science and Engineering: B*, 179:1–5, 1 2014.

[176] Zhangcan Yang, Michael A. Lively, and Jean Paul Allain. Kinetic monte carlo simulation of self-organized pattern formation induced by ion beam sputtering using crater functions. *Phys. Rev. B*, 91(7), 2 2015.

[177] Maureen L. Nietiadi, Luis Sandoval, Herbert M. Urbassek, and Wolfhard Möller. Sputtering of si nanospheres. *Phys. Rev. B*, 90(4), 7 2014.

[178] Matt P. Harrison and R. Mark Bradley. Crater function approach to ion-induced nanoscale pattern formation: Craters for flat surfaces are insufficient. *Physical Review B*, 89(24):245401, 2014.

[179] Herbert M. Urbassek, R. Mark Bradley, Maureen L. Nietiadi, and Wolfhard Möller. Sputter yield of curved surfaces. *Phys. Rev. B*, 91(16), 4 2015.

[180] F. Frost, B. Ziberi, T. Höche, and B. Rauschenbach. The shape and ordering of self-organized nanostructures by ion sputtering. *Nuclear Instruments and Methods in Physics Research Section B: Beam Interactions with Materials and Atoms*, 216:9–19, 2 2004.

[181] Ferdinand Verhulst. *Nonlinear differential equations and dynamical systems*. Springer Science & Business Media, 2006.

[182] J. H. Kim, N. B. Ha, J. S. Kim, M. Joe, K. R. Lee, and R. Cuerno. One-dimensional pattern of au nanodots by ion-beam sputtering: formation and mechanism. *Nanotechnology*, 22(28):285301, 7 2011.

[183] J. . H. Kim, J. . S. Kim, J. Muñoz García, and R. Cuerno. Role of nonlinearities and initial prepatterned surfaces in nanobead formation by ion-beam bombardment of au (001): Experiments and theory. *Physical Review B*, 87(8):085438, 2013.

[184] Adrian Keller and Stefan Facsko. Tuning the quality of nanoscale ripple patterns by sequential ion-beam sputtering. *Physical Review B*, 82(15):155444, 2010.

[185] J.-H. Kim, M. Joe, S.-P. Kim, N.-B. Ha, K.-R. Lee, B. Kahng, and J.-S. Kim. Pattern evolution on previously rippled au(001) by crossing-ion-beam sputtering. *Physical Review B*, 79(20), 5 2009.

[186] M. Joe, J-H Kim, C. Choi, B. Kahng, and J-S Kim. Nanopatterning by multiple-ion-beam sputtering. *J Phys Condens Matter*, 21(22):224011, 6 2009.

[187] G. Carter. Surface ripple amplification and attenuation by sputtering with diametrically opposed ion fluxes. *Vacuum*, 79(1-2):106–109, 7 2005.

[188] Sebastian Vogel and Stefan Linz. Surface structuring by multiple ion beams. *Physical Review B*, 75(8), 2 2007.

[189] B. Ziberi, F. Frost, Th Höche, and B. Rauschenbach. Ripple pattern formation on silicon surfaces by low-energy ion-beam erosion: Experiment and theory. *Physical Review B*, 72(23):235310, 2005.

[190] Alexandre Cuenat, H. Bola George, K-C . C. Chang, Jack M. Blakely, and Michael J. Aziz. Lateral templating for guided self-organization of sputter morphologies. *Advanced Materials*, 17(23):2845–2849, 2005.

[191] Martin P. Gelfand and R. Mark Bradley. Highly ordered nanoscale patterns produced by masked ion bombardment of a moving solid surface. *Physical Review B*, 86(12):121406, 2012.

[192] Daniel Michelson. Steady solutions of the kuramoto-sivashinsky equation. *Physica D: Nonlinear Phenomena*, 19(1):89–111, 1986.

[193] M. Rost and J. Krug. Anisotropic kuramoto-sivashinsky equation for surface growth and erosion. *Phys Rev Lett*, 75(21):3894–3897, 11 1995.

[194] Adrian V. Coward, Demetrios T. Papageorgiout, and Yiorgos S. Smyrlis. Nonlinear stability of oscillatory core-annular flow: A generalized kuramoto-sivashinsky equation with time periodic coefficients. *Zeitschrift für angewandte Mathematik und Physik ZAMP*, 46(1):1–39, 1995.

[195] M. A. Tagg, R. Smith, and J. M. Walls. Sample rocking and rotation in ion beam etching. *Journal of materials science*, 21(1):123–130, 1986.

[196] G. Carter. Theory of ripple topography inhibition in depth profiling with sample rocking. *Appl. Phys. Lett.*, 71(21):3066, 1997.

[197] Matt P. Harrison and R. Mark Bradley. Nanoscale patterns formed by ion bombardment of rotating binary materials. *Journal of Physics: Condensed Matter*, 27(29):295301, 2015.

[198] Yoshinobu Aoyagi and Susumu Namba. Blazing of holographic grating by ion etching technique. *Jpn. J. Appl. Phys.*, 15:721, 1976.

[199] B. S. Tilley, S. H. Davis, and S. G. Bankoff. Nonlinear long-wave stability of superposed fluids in an inclined channel. *Journal of Fluid Mechanics*, 277:55–83, 1994.

[200] E. G. Loewen, M. Neviere, and D. Maystre. Grating efficiency theory as it applies to blazed and holographic gratings. *Appl. Optics*, 16(10):2711–2721, 1977.

[201] N. V. Medhekar, W. L. Chan, V. B. Shenoy, and Eric Chason. Stress-enhanced pattern formation on surfaces during low energy ion bombardment. *Journal of Physics: Condensed Matter*, 21(22):224021, 2009.

[202] Martin P. Gelfand and R. Mark Bradley. One dimensional conservative surface dynamics with broken parity: Arrested collapse versus coarsening. *Phys. Lett. A*, 379(3):199–205, 1 2015.

[203] M. Sato and M. Uwaha. Step bunching as formation of soliton-like pulses in benney equation. *Europhys. Lett.*, 32(8):639, 1995.

[204] J. H. Kim, J. S. Kim, J. Muñoz García, and R. Cuerno. Role of nonlinearities and initial prepatterned surfaces in nanobead formation by ion-beam bombardment of au(001): Experiments and theory. *Physical Review B*, 87(8), 2 2013.

[205] T. Spalvins and W. A. Brainard. Nodular growth in thick-sputtered metallic coatings. *J. Vac. Sci. Technol.*, 11(6):1186–1192, 1974.

[206] M. P. Kowalski, R. G. Cruddace, K. F. Heidemann, R. Lenke, H. Kierey, T. W. Barbee, and W. R. Hunter. Record high extreme-ultraviolet efficiency at near-normal incidence from a multilayer-coated polymer-overcoated blazed ion-etched holographic grating. *Opt. Lett.*, 29(24):2914–2916, 2004.

[207] D. G. Stearns, P. B. Mirkarimi, and E. Spiller. Localized defects in multilayer coatings. *Thin Solid Films*, 446(1):37–49, 2004.

[208] J. Röder and H.-U. Krebs. Frequency dependent smoothing of rough surfaces by laser deposition of zro2. *Appl. Phys. A*, 90(4):609–613, 2008.

[209] K. P. Shaha, Y. T. Pei, C. Q. Chen, A. A. Turkin, D. I. Vainshtein, and J. Th M. De Hosson. On the dynamic roughening transition in nanocomposite film growth. *Appl. Phys. Lett.*, 95(22):223102, 2009.

[210] Johanna Röder, Tobias Liese, and H.-U. Krebs. Material-dependent smoothing of periodic rippled structures by pulsed laser deposition. *J. Appl. Phys.*, 107(10):103515, 2010.

[211] Matt P. Harrison and R. Mark Bradley. Blazed diffraction gratings produced by ion bombardment of pre-patterned solid surfaces. *Journal of Applied Physics*, 121(5):054308, 2017.

[212] A. V. Vinogradov and B. Ya Zeldovich. X-ray and far uv multilayer mirrors: principles and possibilities. *Applied optics*, 16(1):89–93, 1977.

[213] I. V. Kozhevnikov and A. V. Vinogradov. Basic formulae of xuv multilayer optics. *Physica Scripta*, 1987(T17):137, 1987.

[214] Mehran Kardar, Giorgio Parisi, and Y. . C. Zhang. Dynamic scaling of growing interfaces. *Physical Review Letters*, 56(9):889, 1986.

[215] Matt P. Harrison and R. Mark Bradley. Producing virtually defect-free nanoscale ripples by ion bombardment of rocked solid surfaces. *Phys Rev E*, 93(4-1):040802, 4 2016.

[216] Matt H. Harrison and R. Mark Bradley. Fabrication of high quality multilayer blazed gratings using ion beam assisted deposition. *J. Appl. Phys.*, 2017.